Development and improvement of embedded structures in microelectronic chips : Study of mechanical and electrical contact

Sebastian Orellana

THÈSE DE DOCTORAT

de l'Université de recherche Paris Sciences et Lettres

PSL Research University

Préparée à

MINES ParisTech

Development and improvement of embedded structures in microelectronic chips : Study of mechanical and electrical contact.

~~~

Développement et amélioration de structures mobiles embarquées dans les interconnexions des puces microélectroniques :
Etude du contact mécanique et électrique.

Ecole doctorale n°364

Sciences Fondamentales et Appliquées

Spécialité : Computational mechanics and Materials

Soutenue par **Sebastian ORELLANA**

Le 11 Octobre 2016

Dirigée par Karim INAL & Pierre MONTMITONNET

COMPOSITION DU JURY :

M. BOSSEBOEUF Alain
Directeur de Recherches CNRS,
C2N Paris-Saclay
Rapporteur

M. COCCETTI Fabio
Docteur, HDR, RF-Microtech, Toulouse
Rapporteur

M. FORTUNIER Roland
Professeur, ENI, Saint-Etienne
Président

M. INAL Karim
Professeur, MINES ParisTech – CEMEF
Examinateur

M. MONTMITONNET Pierre
Directeur de Recherches CNRS, MINES ParisTech – CEMEF
Examinateur

M. FORNARA Pascal
Docteur, STMicroelectronics, Rousset
Examinateur

MINES ParisTech | PSL RESEARCH UNIVERSITY PARIS
~~~

“ *The future has many names: For the weak, it means the unattainable. For the fearful, it means the unknown. For the courageous, it means opportunity.* ”Victor Hugo

I would like to dedicate this thesis to my family, thanks . . .

Acknowledgements

This thesis is the result of three years of work at: ST Microelectronics, Rousset; CEMEF (Paris Science and Humanities) MINES ParisTech, Sophia Antipolis and CMP (Centre Microélectronique de Provence) MINES Saint-Etienne, Gardanne, where I have met remarkable people who I wish to acknowledge.

I would first like to thank the members of the jury: Professor Alain Bosseboeuf and Dr. Fabio Coccetti for taking time out of their busy schedules to assess my work. My thanks go also to Professor Roland Fortunier for agreeing to preside the defence. It was a great honour to have you on my thesis committee.

I would like to give special thanks to my academic advisors, Professor Karim Inal and Professor Pierre Montmitonnet. They taught me how to reach good results through methodical and thorough research work. I'm grateful for all their contribution of time, ideas and patience, which contributed to make my Ph.D. a productive and stimulating experience.

I am very much obliged to my industrial advisor, Dr. Pascal Fornara for his implication, time and guidance. My deepest thanks to you for all your support during my four years at STMicroelectronics.

I would also like to thank Dr. Jean-Michel Mirabel, R D manager at Rousset, as well as Dr. Elisabeth Massoni, director of CEMEF, for giving me the opportunity to do my PhD. in their respective departments.

After spending three years mainly at ST Rousset and CMP Gardanne, there are many people I want to thank. First of all, I am deeply indebted to Cristian (El Paisano) and Brice for their guidance and advice on this work. I thank Kevin, Maxime and Mohamed for helping me to improve our device. I'm grateful to the Advanced Technology team: Nando and Antonio, and the TCAD Team: Valerie, Roberto and Julien, for their support and for welcoming me in the team.

I obviously cannot forget to acknowledge the tremendous help from all the technicians, engineers, researchers and interns from ST and the CMP – without whom I would not have achieved such quick and good results. My sincere thanks to: Thierry for his support on HF release; Carole for her help on the first analyses of the SEM/TEM and HF release; Suzanne for her support on the in-situ heating in the SEM test.

Then, I wish to express my thanks to my colleagues from ST with whom I shared offices, coffee time, and with whom I have spent enjoyable times – in particular at the doctorate box: Abdel, Alexandre, Aurélie, Bertrand, Dino, Julien, who welcomed me there; Adrien, Alejandro, Anthony, Arnaud, Clément, Emilie, Jordan, Laudine, Maria, Marjorie, Nico, Thibault, Victor, Vincent ...

Finally, I would like to express my most sincere and friendly thanks to my colleagues at CMP: Clément, Eloise, Etienne, Henda, Malika, Mohamed, Olivier, Rubaiyet...

It is now time to thank the people who are the dearest to me. And I need to thank them in Spanish...

Mi primer pensamiento, a la distancia, va hacia mi familia. Mi madre, mi tia, mis hermanos, mis primos, gracias a todos por apoyarme. Gracias por estar siempre ahi, y creer en mi cuando he perseguido mis sueños. Gracias Pauline, por soportarme, en las buenas y en las malas. Ahora que la tesis se terminó, tendras que buscar una nueva excusa para molestarme :P

Introduction

In the early 1900s, the vacuum tube led to technological advances in electronics. Afterwards, in the 1940s the development of the first transistor established a revolution in the electronic industry. Embedded on a semiconductor, the first silicon transistor (1947) started the race which consists in developing the smallest devices possible. Thus, in 1965, Gordon Moore published a paper forecasting a fast miniaturization of devices that would allow the number of components per integrated circuit to double every year [3]. This proposition establishes the well-known "Moore law", which has been governing the microelectronics development for the last fifty years.

The mechanical machines also took advantage of the miniaturization observed in electronics devices. The first paper about miniaturization in microsystems was written in 1967 by Nathanson et al. [1], who developed and manufactured the resonant gate MOS transistor. The microsystems or Micro-Electro-Mechanical Systems (MEMS) are miniaturized systems incorporating sensors, actuators and information processing devices. These systems, the size of which ranges from a few micrometers to a few millimeters, are made by using various micro/nano fabrication technologies with processes derived from microelectronics or with specific processes.

Manufacturers have made the Moore law the rule in semiconductors industry for developing and miniaturizing circuit boards. However, silicon electronics faces a challenge. The latest circuits are just about 7 nm wide. Yet, the size of individual silicon atoms (around 0.2 nm) appears to be the hard physical limit – considering the possibility of a single-atom-wide circuit. The idea was then to integrate "smarter" components at assembly. Following this new principle, known as "More than Moore", smaller products with more features could still be created.

The technologies Systems on Chip (SoC) were born in response to this context – promising that integrated solutions would add new functionalities in small dimensions. The SoC solution is a technology where several features live together on one single chip. The evolution of this technological solutions is the CMOS-MEMS – *i.e.* the MEMS is fabricated at the same time as electronics part. The first CMOS-MEMS, following Parameswaran et al. [2], was a poly-silicon micro-bridge. The interest of integrating the MEMS devices in a Complementary Metal Oxide

Semi-conductor (CMOS) fabrication flow is to reduce cost by avoiding additional fabrication steps with special materials.

The miniaturization of the devices adds new technological challenges, such as the properties changes at small scale. The well-known material properties for bulk evolves at the scale of thin film complexifying its thermal, electrical and mechanical analysis. The goal of this thesis is then to make a functional structure and cope with problems linked to miniaturization.

One of studied devices was originally designed as a passive stress sensor, able to measure the stress level on a film layer. It consists of a metal line inserted in an oxide layer above Silicon. When the oxide is eliminated, the arms of this MEMS are freed and rotate under the effect of initial internal stresses.

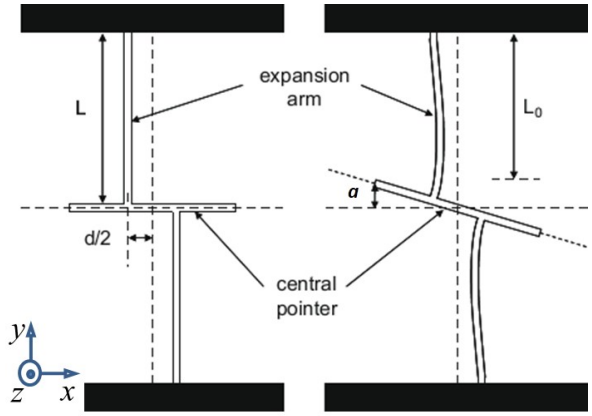

Fig. 1

It has been suggested that these movements could also be exploited to modify the electrical state of the system in which it is inserted, to change a capacity or to switch on/off. The effect in this case is obtained by an actuating current inducing Joule heating and dilatation. This is the context of this research, which is carried out by Multiphysics Finite Element Method (FEM) simulation and various characterization methods – *i.e.* SEM nanoprobing, optical profilometer, electrical measurements and in-situ heating SEM.

The challenge then lies in the release of the moving parts by dissolution of the surrounding oxide (out of plane deformation under the effect of residual stress, stiction and residues which prevent contact), in the actuator (current density, repeatability, durability, reliability) and, for ohmic switches, in the ability to establish a real electrical contact with low resistance (real / apparent area of contact with rough surfaces, contact pollution). Of course, an important job is to do the design and simulate of microsystems to overcome these difficulties and / or to study the behavior and measure the effects.

This PhD thesis is organized into four chapters:

- The first chapter is dedicated to a bibliographic study based on four axes: the MEMS process flow; the mechanical stress; the mechanical and electrical contact; and the MEMS reliability.
- The second chapter studies the residual stress in the structures. The stress is studied from the wafer fabrication to the final device. FEM analyses are performed in order to support and explain experimental data.
- The third chapter studies the actuation process on devices following several steps. First a thermal actuation is studied, followed by a Joule effect actuation, finishing with a mechanical contact and its FEM model. The latter considers the release step, the actuation part and the mechanical contact.

Table of contents

Chapter 1

Bibliographical Review

Contents

Born from the need to reduce size and to integrate the mechanical properties in electronics systems, the MEMS have emerged in the 80's. The first MEMS, the resonant gate transistor developed by Nathanson et al. [1] consists in a electrostatically excited cantilever beam employing field-effect transistor.

In this chapter a bibliographical review is presented in order to clarify the complex fabrication process needed by a MEMS device, a *CMOS-MEMS* [2] in our case. The compatibility between the fabrication of mobile mechanical parts and a classical microelectronics fabrication flow is studied.

Companies in the technology sector are competing to provide better integrated solutions. The last years two trends stood out, the More Moore and the More than Moore.

Contrary to Moore's law[1] [3], which aims at increasing the transistor density, the More than Moore (MtM) strategy aims at the integration of applications and functionalities. More Moore (MM) refers to the continued shrinking of horizontal and vertical physical feature sizes to reduce cost and improve performances.

The roadmap for microsystems industry shown in Figure 1.1 – elaborated by the International Technology Roadmap for Semiconductors (ITRS) – put the More than Moore strategy in a central position of the future of microsystems – lead by the internet of things.

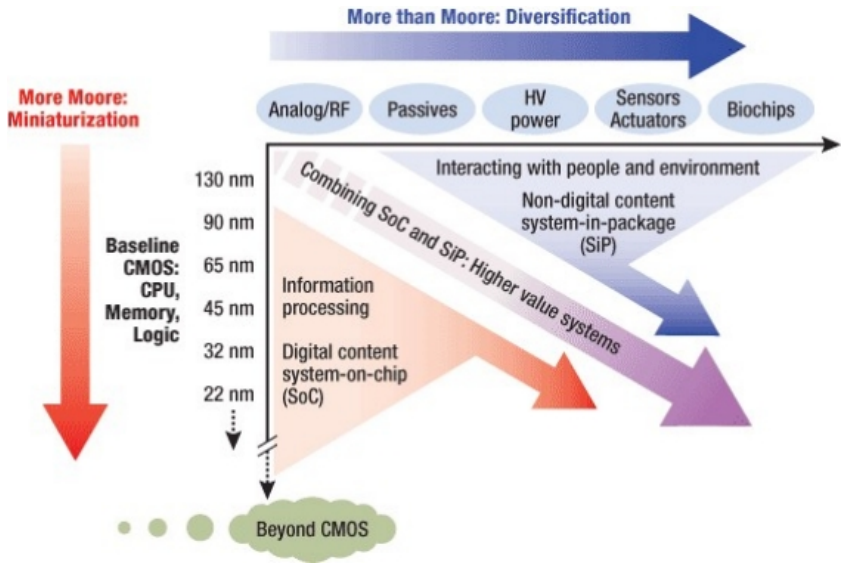

Fig. 1.1 ITRS roadmap, 2010 version

Figure 1.1 maintains the difference between miniaturization and diversification, creating two distinct parts: Beyond Moore and More than Moore. As the MEMS have been developed

[1]The complexity for minimum component costs has increased at a rate of roughly a factor of two per year. Certainly over the short term this rate can be expected to continue, if not to increase.

to perform mechanical functions, they are located in the MtM trend – *i.e.* as a sensor/actuator device.

Three parts are treated in this chapter. First, an introduction to MEMS fabrication is presented. Second, the issues related to MEMS development are treated in two parts; the residual stress present in thin films and the contact from both mechanical and electrical points of view. Finally, some MEMS reliability issues are given.

1.1 MEMS process flow

1.1.1 MEMS devices

The word Microsystems, Micro-electro-mechanical systems or just MEMS [4] refers to:

- Micro, related to size of devices in micrometre scale,
- Electro, which suggests either electrical or electronics, and
- Mechanical = existence of mobile or deformable parts.

The MEMS devices according to its functionality are mainly classified as sensors and actuators [4, 5].

This definition does not consider all devices or functions currently performed. At present, various physical phenomena are exploited to create new devices. Thus, using physics as:

- information transmission: fluidic [6], optical [7],
- actuator or detector: thermal [8, 9], magnetic [10], piezoelectric [11],

The MEMS can be divided in:

- sensor that measures: *e.g.* pressure [12],
- actuators: with or without moving parts [13].

The conception of MEMS is not only a size reduction of "macro" system, *e.g.* gear [13], but rather a motivation to solve problems arising in the "small world", *e.g.* inkjet printer head [14].

A wide variety in the kinds of the MEMS devices, divided between sensors and actuators, was presented. This work studies the switch devices, their integration and fabrication issues.

1.1.2 MEMS Switch introduction

One of the fastest growing markets in the last years is in the MEMS switches, which present various advantages compared with their predecessors, the p-i-n-diode or *FET* switches: near-zero power consumption (for electrostatic switches); very high isolation (formed by air gap); very low insertion loss [15].

From the first micro-relay developed by Petersen in 1979 [16] these devices have continuously evolved. These last years, the mechanical micro-switch takes an important place as

RF-switch device, removing the hegemony of solid state switches [15] in the microelectronics industry.

The RF circuits, where a switch can be commuted at a high frequency, is not the only application. The majority of switches have an electrostatic actuation [15, 17], which ensures a high speed commutation; there are also bistable switches [18–21] and latching switches [22, 23], used in low power applications. Among other types of actuation we can find: thermal switches [24, 25], magnetic switches [26] and capacitive switches [27].

In standard fabrication (Figure 1.2), the MEMS device is assembled as a single device, which is put close to the electronic device; the two are wired together and then the assembly is packaged.

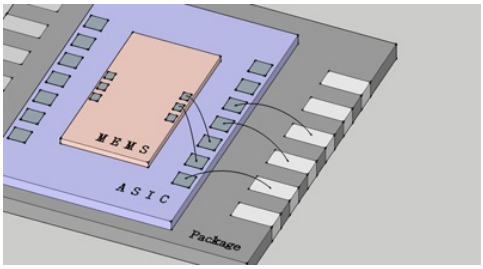

Fig. 1.2 Packaging of MEMS device, the electronic device (ASIC) with the mechanical part (MEMS) bound together in a so-called System on Chip (SoC)

This method of stacking can be a source of issues in fabrication processes: robustness problems, increase of fabrication cost, longer fabrication time.

The research laboratory and industry actors are working on the technique to improve the embedded multiple functions in a single device. The *CMOS-MEMS* concept and different fabrication process are then explained in the next section.

1.1.3 CMOS-MEMS

The interest of integrating the MEMS devices in a CMOS fabrication flow is to reduce cost by avoiding additional fabrication steps with special materials and individual packaging processes. The first *CMOS-MEMS*, due to Parameswaran et al. [2], was a poly-silicon micro-bridge.

The MEMS devices use some of the microelectronics fabrication processes like photolithography or material deposition steps [28].

The *RF MEMS-CMOS* development has been studied by Mansour [29], who made an in-depth study of the possibilities of integration between CMOS and MEMS technologies. MEMS fabrication processes are classified as:

1.1.3.1 Pre-CMOS: MEMS fabricated before CMOS

Sandia National Laboratory [30] proposed a MEMS construction called *Pre-CMOS* (Figure 1.3), in which the MEMS (Micromechanical Device area) are fabricated before the Back end of Line (BEOL) part of circuit (CMOS Device area).

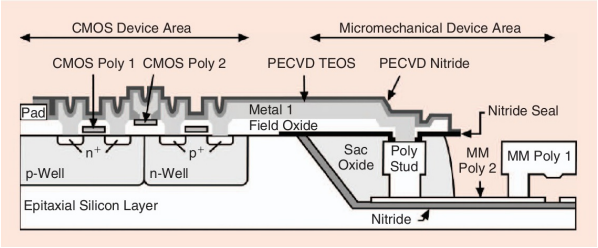

Fig. 1.3 A cross-section schematic of an integrated *MEMS-CMOS* illustrating *pre-CMOS* principle [30]

In the MEMS fabrication process, annealing at 900 °C should be done to avoid residual stress in polysilicon. At such temperatures, the *Al* BEOL present in the CMOS circuit would melt – *i.e.* *Al* melts at 660 °C. To avoid the melting risk, the annealing is performed before BEOL part.

1.1.3.2 Intra-CMOS: MEMS fabricated during the CMOS

Infineon Technologies fabricated in the same level as the CMOS device, a membrane in poly-silicon serving as pressure sensor [12].

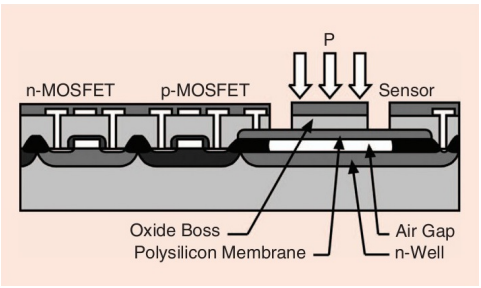

Fig. 1.4 A cross section schematic of Infineon integrated MEMS technology for a pressure sensor [12]

The polysilicon (membrane) is inserted in the BEOL part, thus the stress of this layer should be considered for a successful integration.

1.1.3.3 Post-MEMS: MEMS fabricated after CMOS

The fabrication of CMOS is firstly performed, then the MEMS part is fabricated over the CMOS in a specialized MEMS-factory. The principal problem of this technique is the temperature used in MEMS fabrication which may deteriorate the metal lines of the CMOS device. However, Cavendish Kinetics [31], Berkeley [32], IBM [33] (Figure 1.5) and Wispry [34] develop this sort of *CMOS-MEMS*.

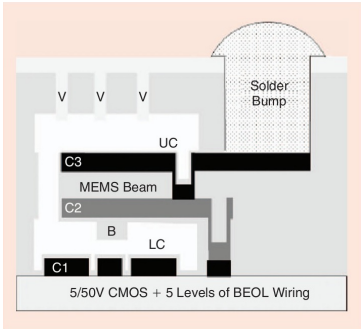

Fig. 1.5 A cross section schematic of IBM/Wispry integrated *MEMS* technology [33]

All these possibilities to integrate CMOS and MEMS technologies in a single fabrication flow present various technical integration problems, principally due to fabrication steps in temperature and material choices.

1.1.3.4 BEOL-MEMS: MEMS fabricated within CMOS

Parameswaran et al. [2] in 1988 created the first *BEOL-MEMS*. Afterward, Carnegie Mellon university continued the development [35, 36], which is actually commercialised as Application Specific Integrated MEMS Process Service (ASIMPS) [37] (Figure 1.6). The principal advantage of this solution is the integration with CMOS fabrication process. Its development needs a Reactive-Ion Etching (RIE) plasma and chemical etching process, both already present in a CMOS standard fabrication flow.

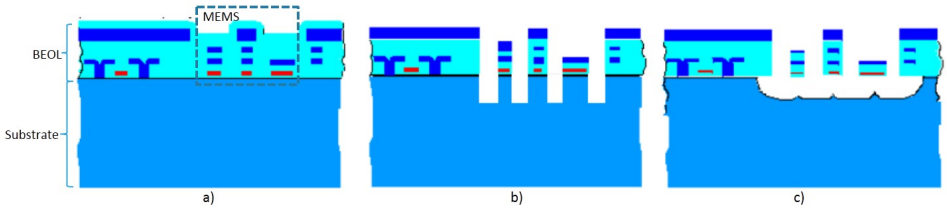

Fig. 1.6 A cross section schematic of Carnegie Mellon *BEOL-MEMS* technology [37]

Pre-, *Intra-* and *Post-MEMS* solutions are intended to insert the "classical MEMS" into a "classical CMOS" device, adding new fabrication steps. All these solutions try to make compatible the MEMS and CMOS fabrication processes.

In conclusion, the *CMOS-MEMS* principle is a simple way to insert an additional function in an electronic device – *e.g.* adapting the fabrication steps used in MEMS.

Because of the "simplicity" of integration in a CMOS factory, the *BEOL-MEMS* principle is used in this work. Later in the manuscript this approach will be developed.

Now I will review a few mechanical aspects. The MEMS studied are built from thin films, which have a particular mechanical behaviour due to their small scale (several tens of microns). The device function is not only dependent of constraint but also by their thermomechanical characteristics.

1.2 Mechanical stress in an isotropic thin film

The thin layers we consider are defined by two characteristics: the film thickness t_f is much smaller than the substrate thickness t_s ($t_f << t_s$); the substrate thickness t_s is much smaller than the film dimensions' d ($d >> t_s$). In the following, we consider only films of isotropic elastic materials, involving two elastic constants, Young's modulus E and Poisson's ratio ν.

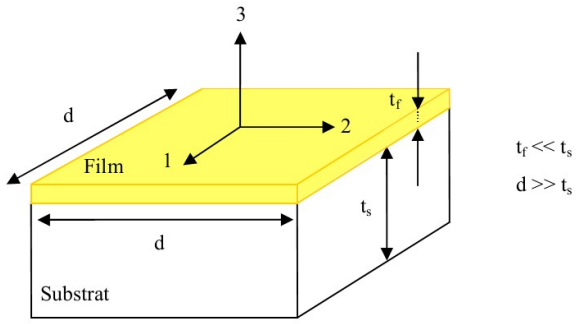

Fig. 1.7 Representation of the stress component in a thin film over substrate in Voigt notation

In the classical case of constrained film/substrate system, the top surface is free of constraint, $\sigma_3 = 0$, which implies in Voigt[1] notation $\sigma_3 = \sigma_4 = \sigma_5 = 0$. Also, the shear stress in the geometric axes in the plane is generally small, so $\sigma_6 = 0$. Although the strain is tri-axial, the plane stress condition applies:

$$\sigma_1 = \frac{E}{(1+\nu)\cdot(1-2\nu)}[(1-\nu)\varepsilon_1 + \nu(\varepsilon_2+\varepsilon_3)] \tag{1.1}$$

$$\sigma_2 = \frac{E}{(1+\nu)\cdot(1-2\nu)}[(1-\nu)\varepsilon_2 + \nu(\varepsilon_1+\varepsilon_3)] \tag{1.2}$$

$$\sigma_3 = \frac{E}{(1+\nu)\cdot(1-2\nu)}[(1-\nu)\varepsilon_3 + \nu(\varepsilon_1+\varepsilon_2)] \tag{1.3}$$

where E and ν are the isotropic elastic modulus and Poisson's ratio respectively. As $\sigma_3 = 0$

$$0 = (1-\nu)\varepsilon_3 + \nu(\varepsilon_1+\varepsilon_2) \rightarrow \varepsilon_3 = -\frac{\nu}{1-\nu}(\varepsilon_1+\varepsilon_2) \tag{1.4}$$

Replacing ε_3, the stress conditions becomes:

[1] The stress tensor in matrix notation is

$$\sigma = \begin{pmatrix} \sigma_{xx} & \sigma_{xy} & \sigma_{xz} \\ \sigma_{yx} & \sigma_{yy} & \sigma_{yz} \\ \sigma_{zx} & \sigma_{zy} & \sigma_{zz} \end{pmatrix}$$

the Voigt notation, simplified to a 6-dim. vector is: $\sigma = (\sigma_{xx}, \sigma_{yy}, \sigma_{zz}, \sigma_{yz}, \sigma_{xz}, \sigma_{xy}) = (\sigma_1, \sigma_2, \sigma_3, \sigma_4, \sigma_5, \sigma_6)$

$$\sigma_1 = \frac{E}{(1-\nu^2)}[\varepsilon_1 + \nu\varepsilon_2] \tag{1.5}$$

$$\sigma_2 = \frac{E}{(1-\nu^2)}[\nu\varepsilon_1 + \varepsilon_2] \tag{1.6}$$

Assuming that the stress is equibiaxial, $\sigma_1 = \sigma_2 = \sigma$:

$$\sigma = \frac{E}{-2\nu}\varepsilon_\perp \quad \text{with} \quad \varepsilon_\perp = \varepsilon_3 \tag{1.7}$$

Or

$$\sigma = M\varepsilon_\parallel \quad \text{with} \quad \varepsilon_1 = \varepsilon_2 = \varepsilon_\parallel \tag{1.8}$$

with M the biaxial modulus $M = \frac{E}{1-\nu}$

The residual stress present in a film over a substrate is induced by the sequence of thermal steps in fabrication process and microstructure evolution. The origin of these stresses can be classified as intrinsic and extrinsic.

1.2.1 Origin of stress

1.2.1.1 Intrinsic stress

Generated during the creation of the film [38, 39], the intrinsic stresses depend on: the material deposited; the different growth modes (*e.g.* columnar grain growth or island growth); the technique used (*e.g.* Physical Vapor Deposition (PVD), Chemical Vapor Deposition (CVD)); the deposition parameters (*e.g.* environmental gas, substrate temperature).

This intrinsic stress is then considered as fixed in a controlled environment, granted by the microelectronics production line.

The sources of intrinsic stress depend on the deposition process and the involved materials. Some important examples are listed below [40]:

- Coalescence of grain boundaries: during the film deposition the grains grow over a substrate. In many cases, the Volmer-Weber island growth mechanism dominates (Figure 1.8). When these crystallites coalesce, a tensile stress is generated.

- Grain growth: due to coalescence of grains and the elimination of its boundaries the film reaches a minimum system energy. Thus, the number of grains decreases as the grains grow. The elimination of the grain boundary densifies the film and a tensile stress is created.

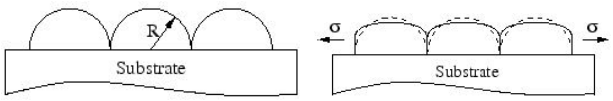

(a) (b)

Fig. 1.8 Coalescence of deposited grains, a) the islands of material grow and b) become elastically strained generating a tensile stress state in the film

- Misfit stress: in the case of epitaxy, the lattice constants between the deposited thin film (a_f) and the substrate (a_s) are generally different. The deposition process forces the crystal lattices of the film and the substrate to strain to fit, inducing stress.

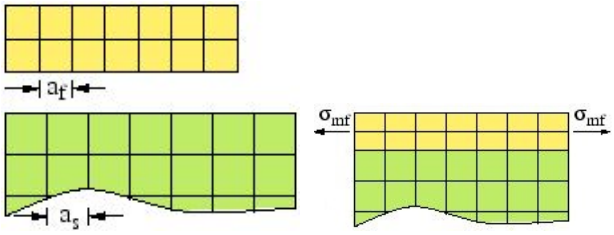

(a) (b)

Fig. 1.9 a) An original lattice difference (a_f vs a_s) generate b) leads to misfit stress (σ_{mf})

1.2.1.2 Extrinsic stress

The thermo-elastic deformation generated by the thermal steps in the microelectronics fabrication is the main source of extrinsic stress. Due to adhesion, if the substrate is much thicker than the attached films, it imposes its own dilatation over the rest of the layers. The stress is thus built by the difference of expansion coefficients between film and the substrate. Then, for a film over substrate system, the substrate deformation induce a homogeneous biaxial deformation on the film defined by [38]:

$$\varepsilon_{film} = \int_{T_0}^{T_1} (\alpha_{sub} - \alpha_{film}) dT \tag{1.9}$$

Where α_{film} and α_{sub} are the coefficients of thermal expansion of the film and substrate respectively. For a limited temperature range, and for α_{film} and α_{sub} independent of temperature, the previous equation can be approximated as:

$$\varepsilon_{film} = (\alpha_{sub} - \alpha_{film}) \triangle T \tag{1.10}$$

Using the previous strain via Hooke's law, the stress can be calculated:

$$\sigma_{film} = -\left[\frac{E}{1-\nu}\right]_{film} (\alpha_{sub} - \alpha_{film}) \triangle T \tag{1.11}$$

In this way, the thermal cycles during the fabrication process of the device generate a thermo-elastic deformation. The temperature can produce a microstructure modification and/or can exceed the elastic limit of the film, which finally determines the stress state of the film.

The CMOS fabrication processes include different materials with notably different properties. The residual stress is a result of all the fabrication process steps and the different materials properties (see Table 1.1) – *e.g.* coefficients of thermal expansion and Young's modulus. The SiO_2, $SiNx$ and TiN compounds have quite different α and E values. Table 1.1 gives some values, although it should be kept in mind that these properties may vary considerably from one process to another.

Material	$\alpha \times 10^{-6}[C^{-1}]$	E [GPa]
Si	3	130
SiO_2	~ 0.8	~ 63
SiNx	~ 2.2	~ 164
W	4.27	$385-500$
Cu	16	130
Al	23	70
TiN	~ 9.35	$\sim 500(between\ 450-590)$

Table 1.1 Coefficients of thermal expansion α, and Young's modulus E of the main materials used in microelectronics [41]

The materials used for the structures fabrication and therefore involved in this study are: *Al*, SiO_2, *TiN* and *Si*. In the fabrication flow, over the silicon substrate a successive alternation of an insulator (SiO_2) also called InterMetallic Dielectric (IMD) and a metallic layer – principally *Al* or *Cu* – is deposited, thus forming the Back-end-of-line (B). As already mentioned, the differences of material properties between the *Si* and the added layers, combined with the deposition process and annealing steps, are responsible for residual stress.

Serving to isolate the *Si* substrate from the following layers, an undoped CVD SiO_2 (Tetraethyl Orthosilicate (TEOS)) is deposited at 700 °C – *i.e.* CVD deposition. The TEOS oxide has a compressive residual stress of −100 MPa. Furthermore there is the thermal SiO_2 grown at 800 °C to 1200 °C which has a compressive residual stress of −300 MPa [42] – mainly used as a protective layer for *Si*.

The *Al* film is sputtered using PVD from a target containing $0.5wt\%\ Cu$ – *i.e.* *Al* (*Cu*). The addition of copper increases the resistance to electromigration by slowing down the grain

boundary diffusion [43]. The target reaches a temperature of 90 °C during the deposition step – while the wafer is heated to 350 °C. A biaxial residual tensile stress of ∼300 MPa is reported in literature [44, 38] on *Al* (*Cu*) layer.

The *TiN* layer is added on top of the *Al* layer to avoid the electromigration of *Al* lines. This *TiN* is deposited using CVD process with a heater temperature of 450 °C and a wafer temperature of 407 °C. Meanwhile, the *TiN* layer has a compressive stress near −800 MPa [45, 46].

These fabrications steps are repeated as many times as there are metal levels in our technology – *i.e.* the levels that make up the back-end-of the line technology. Thus, the multiple steps which use high temperature make the residual stress in the layer evolve [44]. Figure 1.10 show the stress in an *Al* layer on a heating-cooling cycle.

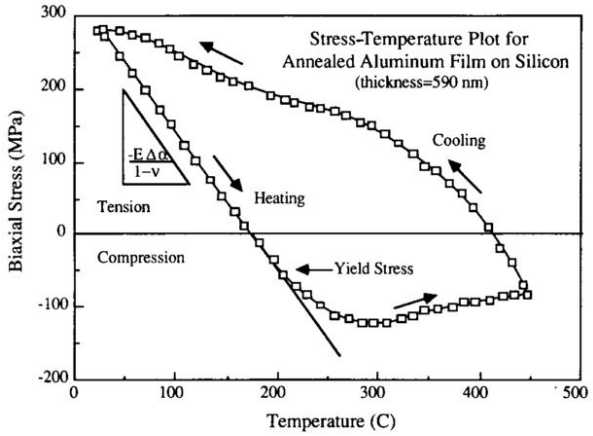

Fig. 1.10 Stress-temperature plot for an *Al* film on a *Si* substrate. Elastic and plastic deformations occur in the film during a thermal cycle [44]

The residual stress is harmful in most cases. It is therefore important to measure it.
The stress in thin films can be determined from:

- Substrate curvature (optical interferometry [47], X-ray diffraction [48], laser scanning [49])
- Lattice spacing (X-ray diffraction [50]),

The simplest method is to measure the substrate curvature and use Stoney's approximation [51, 41], for a thin substrate-film composite – *i.e.* the film is thin in front of the thickness of the substrate (<5%) [52].

1.2.2 Passive stress sensor

Another way to measure the residual stress is to insert a sensor in the thin film, for instance the Rosettes stress sensor [53, 54], which measures the electrical response from an array of transistors, and the cross-shape stress sensor [55, 56], which relies on the rotation in a structure due to an initial stress level.

The design of our cross-shape stress sensor is based on the work of Horsfall [57] on aluminium and Kasbari [56] on copper structures. The structure, integrated in a single layer, is composed of two metallic expansion arms connected to a metal central pointer, thus forming a conducting asymmetrical cross (Figure 1.11).

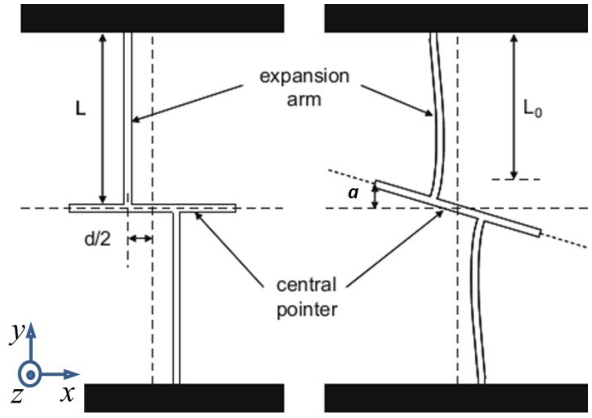

Fig. 1.11 Sensor diagram [58], fabricated in a single metallic layer

It consists of a metal line inserted in an oxide layer above Si. When the oxide is etched, the arms of this MEMS are released and the pointer rotates under the effect of initial internal stresses (Figure 1.11).

These movements could also be exploited to modify the electrical state of the system in which it is inserted, to change a capacity or to switch on/off – *i.e.* electro-mechanical switch. The effect in this case is obtained by an actuating current inducing Joule heating and dilatation.

As a switch has been chosen for test implementation, the present study will try to understand the mechanisms and laws related to electro-mechanical contact. The electrical contact term requires a junction between two conductors, which is apt to carry electric current. Next section develops the study of contact, considering both mechanical and electrical properties.

1.3 Mechanical and electrical contact

Holm [59] has studied the electric contact, and one of the first relations proposed by Holm highlights the need to define first the mechanical contact. A scheme of the contacting parts (Figure 1.12) recalls that surfaces are not perfectly smooth. One undesirable effect of these asperities is that only a few contact spots are available for the electric current, inducing a constriction of the flow, and a resulting increase of the "electric contact resistance".

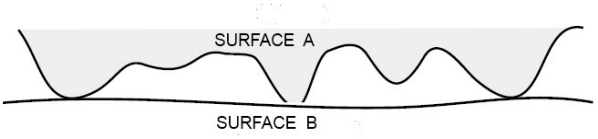

Fig. 1.12 Representation of the contact zone between A (rough) and B (smooth) surface

To make a good contact both the mechanical and the electrical contact should be studied and improved. The next section studied the mechanical contact through different models.

1.3.1 Mechanical contact

Mechanical contact between two smooth bodies is described as a relationship between the contact area and the applied pressure applied, involving material characteristics:

- Elastic modulus (E)
- Poisson's ratio (ν)
- Elastic limit (R_p or σ_y) or Hardness (H)

Contact between rough surfaces requires more sophisticated models to predict the overall contact area, the real area in contact, and in some cases the contact spot size distribution and local pressure. The knowledge of the topography in the nanometric scales is indispensable.

The short name $a-spot$ for the conducting contact areas, referring to the radius a of a circular contact area, is a widely accepted term. The sum of all these areas or $a-spots$ is the load bearing area A_b ($A_b = \sum_n \pi a_n^2$) upon which the pressure p is applied [59] that gives a load P of:

$$P = \xi_c H A_b \tag{1.12}$$

where ξ_c is the p/H ratio, usually $0.2 < \xi_c < 1$ and H is the (macroscopic) contact Hardness, so the spot has only a plastic deformation.

The mechanical contact is imperfect at every scale. The hills and valleys present on the surface make a difference between the real contact and nominal contact area.

Modelling the real contact area requires to establish a relation between the applied macroscopic load and the number and size of contact spots, and for completeness their deformation and contact stress. Each contact spot may be elastic or plastic.

Many authors have tried to model the three basic cases: elastic, elastic-plastic or purely plastic model deformation of spots. Some used analytical, others numerical approaches, the description of a-spots being statistical or deterministic (Table 1.2).

Reference	roughness description	elastic-plastic	statistical -deterministic	analytical -numerical
[60, 61]	Statistic	elastic	Statistical	analytical
[62]	Fractal	elastoplastic	Statistical	analytical
[63]	Multiscale	elastoplastic	Deterministic	numerical
[64]	Real measurement	elastoplastic	deterministic/ statistical	numerical
[65, 66]	Deterministic	plastic	Deterministic	analytical

Table 1.2 Resume of contact theories

In the following, the survey is restricted to small to moderate real contact area, as can be expected in our electro-mechanical contact problems ((1 to 6) µN [67, 68]). We leave aside the high pressure contacts which can be found in metal forming [69] or mechanical joints [70]. Physically, this implies that plasticity is limited to the smallest scale asperities, or to the top of larger asperities.

1.3.1.1 Elastic, statistical analytical contact:

Considering roughness peaks as spherical caps, this first analysis is based on Hertz' theory [60, 61] of elastic contact of a sphere (radius β) with a semi-infinite body. Originally, the contact radius a_c, area A_b, and load P can be expressed in terms of w, the distance by which the sphere has sunk into the half-space, as [60]

$$a_c = \beta^{1/2} w^{1/2}, \;\; A_b = \pi \beta w, \;\; P = \frac{4}{3} E' \beta^{1/2} w^{3/2} \tag{1.13}$$

Where E' is the equivalent elasticity modulus

$$\frac{1}{E'} = \frac{1-\nu_1^2}{E_1} + \frac{1-\nu_2^2}{E_2} \tag{1.14}$$

E_i and ν_i are respectively the Young's modulus and Poisson's coefficient of material i.

From these equations, Greenwood and Williamson derived their model of contact between rough surfaces (Figure 1.13) using several assumptions:

- purely elastic micro-contacts,
- independent isolated sphere/plane contacts (strain and stress fields of neighbouring contacts do not interfere),
- the contact of two rough surfaces can be modelled as a rough and a smooth one in contact, using the concept of combined roughness,
- only one scale of roughness is considered.

Distribution of asperities

Assume that two surfaces come in contact until their reference planes are separated by a distance d. Further, the asperities heights have a random distribution, the probability that asperities height is between z and $z+dz$ above some reference plane is $\phi(z)dz$. Accepting that each asperity deforms elastically according to Hertz model, the number of contact spots n, the total contact area A_r and the total load P in general case are:

$$n = N\int_d^\infty \phi(z)dz \tag{1.15}$$

Since N number of asperities, $w = z-d$ and $A_b = \pi\beta w$, then the total area A_r of contact is

$$A_r = \pi N\beta\int_d^\infty (z-d)\phi(z)dz \tag{1.16}$$

And the total load P is

$$P = \frac{4}{3}NE'\beta^{1/2}\int_d^\infty (z-d)^{3/2}\phi(z)dz \tag{1.17}$$

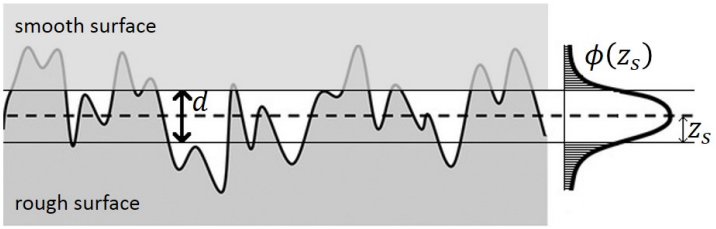

Fig. 1.13 Contact of two surfaces, a smooth and a rough one.

Greenwood and Williamson (GW) [60] represent the previous result in a non-dimensional way, describing heights in terms of standard deviation σ_a of the height distribution. They also

introduce the surface density of asperities η, which multiplied by the nominal area A_n gives the number of asperities $N = \eta A_n$. Then [60]:

Number of contact spots

$$n = \eta A_n F_0(h') \tag{1.18}$$

Total contact area

$$A_r = 2\eta A_n \beta \sigma F_1(h') \tag{1.19}$$

Load

$$P = \frac{4}{3}\eta A_n E' \beta^{1/2} \sigma^{3/2} F_{3/2}(h') \tag{1.20}$$

Where h', the standardized separation, is equal to d/σ and

$$F_n(h') = \int_h^{\prime\infty} (s - h')^n \phi^*(s) ds \tag{1.21}$$

Where $\phi^*(s)$ is the height distribution scaled to make its standard deviation unity.

The model of GW is the first model of rough contact based on statistical method and serves as a basis for the creation of a multitude of other statistical contact models.

1.3.1.2 Criticism

Although very successful, the GW model has been criticized. Its assumptions have been successively questioned.

1.3.1.2.1 Elastic vs plastic asperities Some argue that plastic asperities should be modelled as well, as suggested by GW themselves. Considering the hertzian stress field inside the solids and expressing their plastic limit, GW (Greenwood Williamson 1966) proposed to check for the elastic/plastic state of asperities using the plasticity Index:

$$\psi = \frac{E}{H}\sqrt{\frac{h_p}{\beta}} \tag{1.22}$$

Where H is the material hardness and h_p is the standard deviation of the distribution of peak heights. If $\psi < 0.6$ the contact deformation can be considered as purely elastic for all asperities. If $\psi > 1$ some asperities deform plastically, even under low loads and the contact area is proportional to applied load P:

$$A_n = \frac{P}{H} \tag{1.23}$$

This shows that surfaces, the asperities of which have larger radii of curvature β, wide distribution of peak heights (h_p) or small E/H ratios tend to remain elastic for larger loads.

Elastic-plastic deformation of asperities has later on been introduced in most models. For example, fractal models [62, 63] conclude that small spots are in plastic deformation while large spots are in elastic deformation, because small scale peaks have much smaller radii of curvature, an effect neglected by GW. Duvivier [65], Arrazat [66] and Yastrebov [64] are also cases of elastic-plastic microcontacts, in a classical (mono-scale) context. These models are described below.

1.3.1.2.2 The Multiscale character of surface roughness Others consider that roughness being known as a multiscale stochastic process, multiscale analyses should be elaborated.

In practice, GW considers the existence of a single radius (β) of curvature, which is the average for a surface profile. The problem is the ambiguity of the measurement scale, because the measured radius evolves with the scale of analysis (length measured, discretization step). This is dealt with in Multiscale and fractal models (see Table 1.2 above).

1.3.1.2.3 Interactions between contact spots Finally, GW assume that asperities are far enough from each other that no interaction of the strain and stress fields occurs. This implicitly assumes a very low real area of contact. This can be questioned as well.

It must be noted that GW model considers an isotropic surface. This probably makes a difference in the intensity of the interactions. For instance, Pennec et al. [71] considered an area of interaction and numerical analysis to define the interaction between asperities.

All three issues are reviewed next. In each case, many papers have been published. I will not go too deeply into this approach, because the main aim of this PhD thesis is to make a device robust and electrically active.

1.3.1.3 Multiscale, including fractal analysis

The fractal analysis described by Majumdar and Bhushan (MB) defines a surface as a succession of asperities [62], observation scale-dependent. They consider a surface profile $z(x)$ as shown in Figure 1.14.

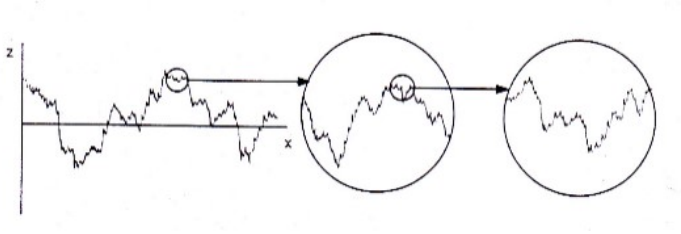

Fig. 1.14 Qualitative representation of statistical self-affinity for a surface profile in fractal model

They proposed the Weierstrass-Mandelbrot (*WM*) functions[1] as an adequate description of this Multiscale character. Such a roughness is composed of sinusoidal waves of different wavelengths and amplitudes superposed on each other. From the *WM* function, at a wavelength of $l_i = \gamma^{n_i}$, the asperity profile $z(x)$ before any deformation is given by [72]:

$$z(x) = G^{D-1} l^{2-D} \cos\left(\frac{\pi x}{l}\right) \quad ; \quad -\frac{l}{2} < x < \frac{l}{2} \tag{1.24}$$

where D is the fractal dimension of the surface profile ($1 < D < 2$), G is the fractal roughness parameter, and l is the length scale of a single asperity (Figure 1.15). In the *MB* model the length scale l is the same as its real contact length, therefore the interference (or distance of interpenetration) (w) of any asperity is equal to its full height (δ):

$$w = \delta = G^{D-1} l^{2-D} \tag{1.25}$$

The principal difference with GW model is that the fractal model considers the radius of curvature (β) of a contact spot to be a function of the area of the spot.

$$\beta = \frac{a^{D/2}}{\pi^2 G^{D-2}} \tag{1.26}$$

where a = radius of the area of contact. The critical area of asperities is:

$$a_{rc} = \frac{G^2}{\left(\frac{K'H}{2E}\right)^{\frac{2}{D-1}}} \tag{1.27}$$

Where H is the hardness of the material, E is the elastic modulus, and K' is the hardness coefficient related to the Poisson ratio ν of the material by [72] $K' = 0.454 + 0.41\nu$.

a_r is the real contact area of asperities, therefore when $a_r < a_{rc}$, the contact mode is plastic, and it becomes elastic when $a_r > a_{rc}$.

[1] $z(x) = G^{D-1} \sum_n \frac{\cos(2\pi\gamma^n x)}{\gamma^{(2-D)n}}$; $1 < D < 2$; $\gamma > 1$, where, D is the fractal dimension, G is a characteristic length scale of the surface and γ^n determines the frequency spectrum of the surface roughness

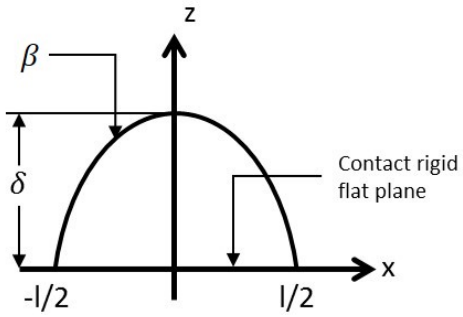

Fig. 1.15 Illustration of a contact spot of length scale l according to *MB* model

The multiscale contact theory proposed by Jackson and Strator (*JS*) is also a model of rough surfaces in contact [63], similar in principle to fractal analysis that tries to model multiscale asperities. This non-fractal multiscale model is applicable to elastic and elastoplastic conditions. A scan length (L) is selected, the surface data is acquired and a FFT is performed. From the resulting Fourier series, the area asperity density and radius of curvature are computed for each frequency level according to [63]:

$$R_i = \frac{1}{4\pi^2 \beta_i f_i^2} \tag{1.28}$$

where f_i denotes the spatial frequency i (*i.e.* the reciprocal of wavelength) and β_i are the asperity amplitude corresponding to the given frequency. Figure 1.16 shows a proportionality between area and load. This observation is valid for Jackson and Green (*JG*) formulation, a Hertz model (Trunc), the Majumdar and Bhushan (*MB*) fractal model and the GW statistical contact model using the Jackson and Green (*JG*) formulation.

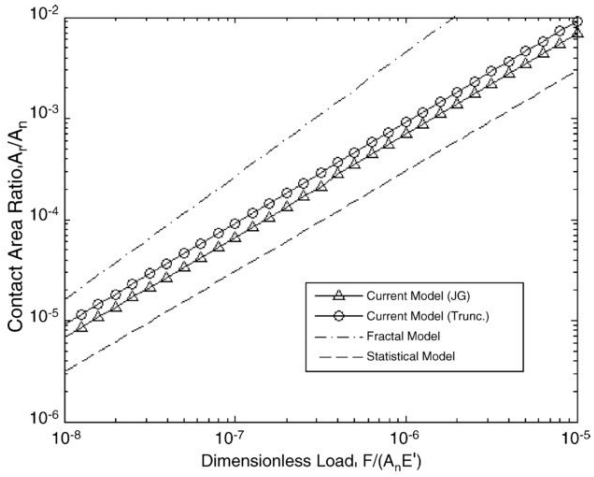

Fig. 1.16 Comparison of elasto-plastic surface contact models [63]

This proportionality, can be interpreted by the average pressure ($\overline{p}$), based on the real contact area (A_r):

$$\overline{p} = \frac{F}{A_r} \tag{1.29}$$

1.3.1.4 Deterministic description of asperities to be deformed

Advances in the computer field have allowed important improvements in FEM, along with the improvements of characterization methods such as Atomic-Force Microscopy (AFM), they have permitted true representations of the sample. This is the basis of "deterministic" (as opposed to statistical) approaches.

1.3.1.4.1 A semi-analytical model The method proposed by Duvivier [65] and Arrazat [66] mixes a classical elastic model, GW like, with an analytical model of plastically deformed peaks. Furthermore, each asperity is described individually in terms of height and radius of curvature (single-scale however) thanks to an AFM measurement of the surface.

At a given penetration of the indenter (hard and smooth compared to the rough surface under study), each peak is notified as elastic or plastic and the relevant model is applied, given the spot size and pressure. The load is finally obtained as the discrete sum of the loads over each asperity.

Here however, the short distance spot-spot interaction is not included; but the large scale elastic sinking of the surface under the indenter load is accounted for and reduces the effective interference of each asperity with the indenter for a given position of the latter.

1.3.1.4.2 FEM modelling of interactions between contact spots The criticism made to GW model related to individual treatment of asperities has been seen by Pennec et al. [71]. They have treated the interaction when several neighbouring asperities are deformed in a contact with a rigid body. As in the previous paper, they obtain a real representation of a bump in a capacitive switch thanks to AFM (Figure 1.17a), then the model is exported to a FEM software with an intermediate Matlab treatment (Figure 1.17a).

Using this data, a FEM model can be performed, this time considering the neighbouring asperities deformation.

Arrazat in his PhD thesis has also worked on the interaction between the contact points. Figure 1.18 shows a comparison of experiments and models of a sphere/plane contact that include or not interaction between spots. The models without interactions between spots overestimate contact force compared with the experimental data. Without interaction, the number of spots in contact is also larger.

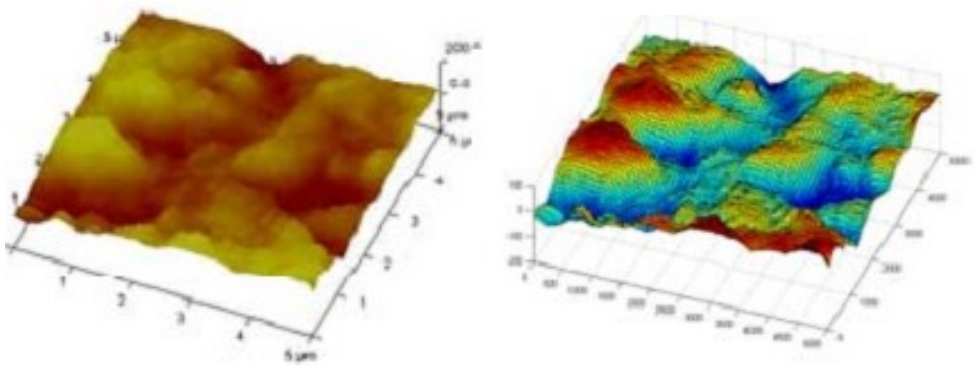

(a) (b)

Fig. 1.17 Topographic survey of a bump in a capacitive switch [71], a) AFM representation, b) FEM representation (treated with Matlab)

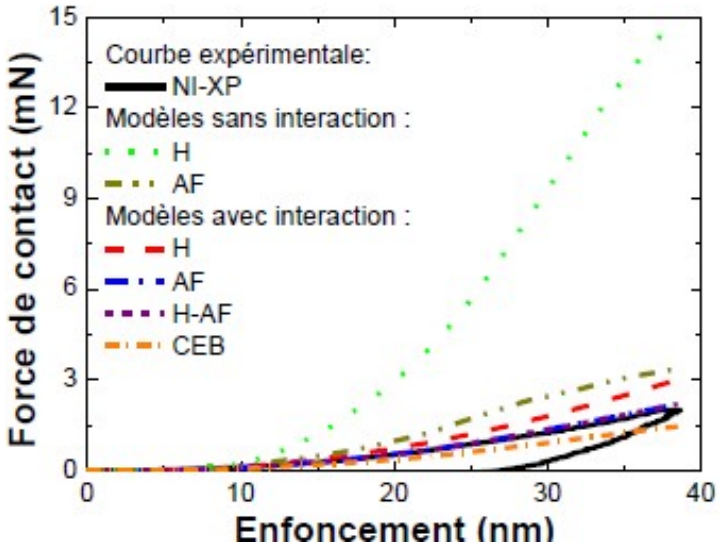

Fig. 1.18 Sphere/plan contact in Arrazat's experience. Comparison of experiments with models with / without neighbouring spot interaction [66] – *i.e.* Hertz (H), Abbott and Firestone (AF), Chang Etsion Bogy (CEB) and Hertz-Abbott and Firestone (H-AF)

Due to the small dimensions (0.3 to 3 µm) of the contact between the arm of the MEMS (1 µm cross section) and the pad, few peaks will be involved so that statistical approaches are questionable. Moreover, deterministic methods may now rely on the high precision of AFM scanning on the one hand, of the FEM model on the other hand. Among the asperity contact models, that elastic-plastic ones should be preferred is shown by the application of the plasticity index (ψ) concept.

Mechanical contact area is not necessarily the area of electrical contact (Figure 1.19) as we will see in the next section (subsection 1.3.2).

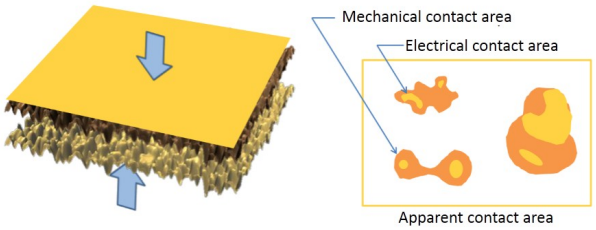

Fig. 1.19 Schema of a real electrical contact, making the difference between apparent, electrical and mechanical contact area [65]

In this way the studies of mechanical contact reported in this section, are not sufficient to estimate an electrical contact area. Meanwhile the next section focuses on how the electrical current flows through the contact: conduction mode and reliability of the contact.

1.3.2 Electrical contact

Ensuring good electrical conduction means reducing the resistance. The contact resistance at an interface must be adapted from the general concept of electrical resistance (R):

$$R = \rho \cdot \frac{L}{A} \tag{1.30}$$

where ρ is the resistivity, L is the length and A is the area of the conducting electrical lines. Taking a junction between two solids and measuring the resistance between two points, a certain distance from the interface, it is found that the resistance is larger than the sum of the resistances calculated from Equation 1.30. This introduces the existence of a specific "contact" resistance.

Now in most cases, the contact is between rough surfaces as pictured in (Figure 1.12). This also constitutes a resistance to electrical conduction, since only a small fraction of the apparent contact surface is available, in the form of a few contact spots – *i.e.* Figure 1.19.

Assume a regular array of contact spots of diameter $2a$, separated by distances $2r$. Electric current lines have to bend and concentrate to go through the spot. The solution of electric field

equations has been made in different situations. From a solution of Laplace's equation using appropriate boundary conditions, Timsit defines in [73] the formula for non-vanishingly small a/r:

$$R_H = \frac{\rho}{2a}\left[1 - 1.41581\left(\frac{a}{r}\right) + 0.06322\left(\frac{a}{r}\right)^2 + 0.13261\left(\frac{a}{r}\right)^3 + 0.19998\left(\frac{a}{r}\right)^4\right] \tag{1.31}$$

If $a << r$, precedent expression reduces to the well-known Holm resistance (R_H):

$$R_H = \frac{\rho}{2a} \tag{1.32}$$

1.3.2.1 Scale dependent theory of electronic transport

The macroscopic conductors are characterized by Ohm's law, which establishes that the resistance of a given sample is directly proportional to its length L and inversely proportional to its area A. However, Ohm's law is no longer applicable at very small scale. In the present project, typical contact area is 1 µm and individual contact spots may be of the order of tens of nanometers.

In microscopic systems, we can identify different regimes of transport related to length scales. An important length scale is the electron elastic mean free path ℓ, which roughly measures the distance between elastic collisions with static impurities. For Crystalline Al, the electron-movement has a mean free paths of $\ell \sim 50nm$ [74, 75].

Considering the relation between the mean free path ℓ and the contact length, we can identify two principal regimes [76]:

if $\ell << L$, it is called diffusive (each electron undergoes a number of diffusions on obstacles; Ohm's law); L is a characteristic length, to be specified case by case,

if $\ell > L$, it is called ballistic (no or few collisions) in which the electron momentum can be assumed constant.

For **ballistic transport**, Sharvin's model [65] calculates the resistance of a circular constriction of radius a in a surface which separates two half-spaces. The Sharvin Resistance (R_s) is characterized by the mean free path ℓ and the resistivity ρ:

$$R_s = \frac{4}{3}\cdot\rho\left(\frac{\ell}{\pi a^2}\right) \tag{1.33}$$

In contrast to subsection 1.3.2, now the surface A and the length L are replaced by πa^2 (the surface of a-spot) and ℓ (the mean free path) respectively.

For **quasi-ballistic transport**, Wexler's model [77] makes the link between ballistic ($a << \ell$) and diffusive ($a >> \ell$) regimes (Knudsen number, $K^* = \ell/a$):

$$R_w = \frac{4K^*\rho}{3\pi a} + \frac{\rho\gamma(K^*)}{2a} = R_s + \gamma(K^*)R_H \tag{1.34}$$

where R_W is the so-called Wexler resistance, and $\gamma(K^*)$ is a slowly varying gamma function.

The model involves a function $\gamma(K^*)$, which weights the addition of the Holm diffusive term to the ballistic term of Sharvin. This function has been calculated by Wexler using Green function integral in the Maxwell limit method, but their calculation is not simple.

Nikolic [78] has proposed a simplified form, where $\gamma(K^*)$ has the limiting value $\gamma(0) = 1$ and $\frac{R_s}{R_H} = 0$. Nikolic's method is able to compute $\gamma(K^*)$ numerically to an accuracy of better than 1 %:

$$\gamma(K^*) = \frac{1 + 0.83K^*}{1 + 1.33K^*} \tag{1.35}$$

Nikolic's answer for γ differs little from the approximate answer of Wexler[1] (Figure 1.20). With this complete relation, we can calculate a resistance for all three regimes – regarding to Figure 1.20, in the quasi-ballistic regime (K^* between 0.1 and 10), both Wexler's and Nikolic's approximation are valid.

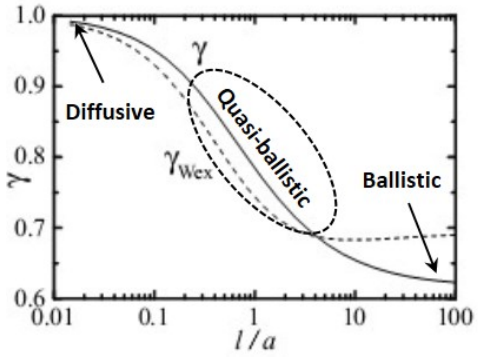

Fig. 1.20 Gamma function dependence on Knudsen number, Wexler (γ_{Wex}) and Nikolic (γ) approximation [78]

Many problems may occur in a metal-metal electrical contact: stiction, creep, sintering, growth of oxide which change the contact resistance. They are particularly significant for small dimension electrical contacts. In the next section the oxidation of aluminium and electrical conduction through this oxide are studied.

[1] The limits of $\gamma(K^*)$ of Wexler are: $\gamma(0) = 1$ an $\lim_{K^*\to\infty}\gamma(K^*) = \frac{9\pi^2}{128} = 0.694$

1.3.2.2 Physical evolutions of the surfaces and consequences on electric contact resistance

The models above give a static, geometric view of electric contact. Furthermore, contacts evolve by a number of physical phenomena. In this work, the main impediment to electrical contact is the oxidation of the *Al*.

A thin layer of oxide grows naturally on almost all metals in contact with air. Growth is faster at higher temperature. Figure 1.21 shows the cross section of the sample used by Mercier et al. [79], Titanium (*Ti*) and Aluminium (*Al*) are deposited over SiO_2. The native aluminium oxide (Al_2O_3) grows at room temperature over the *Al* layer.

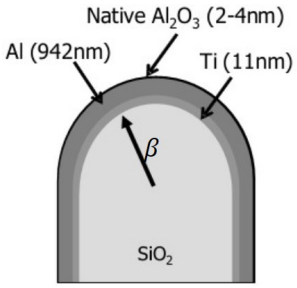

Fig. 1.21 Cross-section illustrating native oxide in aluminium sample [79]

Alumina is a very good insulator – electrical resistivity around $(10^{20} - 10^{22})$ µΩcm contrary to aluminium around 2.8 µΩcm [79]. It builds a high contact resistance so two possibilities for electric conduction are:

- Generate a tunnel effect; that means using a large electric field to generate a weak current flow.
- Cracking alumina improves contact conduction; it is possible by increasing the load, by imposing sliding, or electrically, by a high current flow leading to breakdown of the oxide. When this process is complete, stable ohmic conduction can be retrieved.

Both solutions, tunnel effect and alumina cracking, have some drawbacks.

- **Tunnel effect** allows only a weak flow of current (around 1 nA for 5 nm of aluminium oxide).

  An example of the evolution of current density with an applied potential is shown in Figure 1.22, displaying the *I-V* characteristic for films of different thickness of Al_2O_3– *i.e.* the highest current density observed does not exceed 10×10^{-9} A µm^{-2} (10×10^{-1} A cm^{-2}).

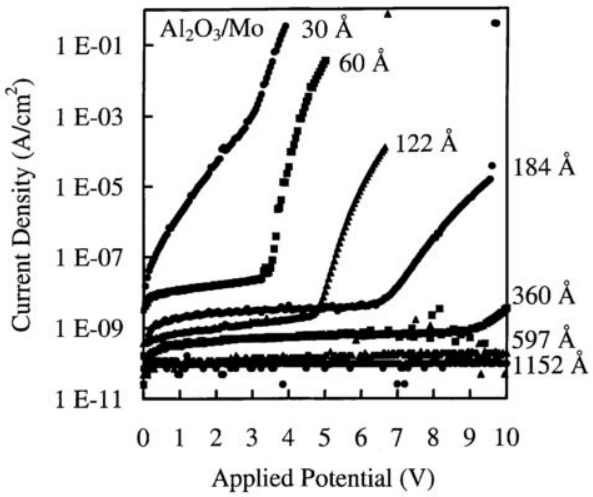

Fig. 1.22 *I-V* plot for films of different thickness of Al_2O_3 ALD (Atomic layer deposition) [80], until its breakdown

- **Cracking** alumina generates welding of metallic parts if the electrical method is used – *i.e.* the switch function is not accomplished.

  An example of the evolution of electrical resistance with an applied load is shown in Figure 1.23, displaying three regimes of conduction in the presence or not of an oxide layer.

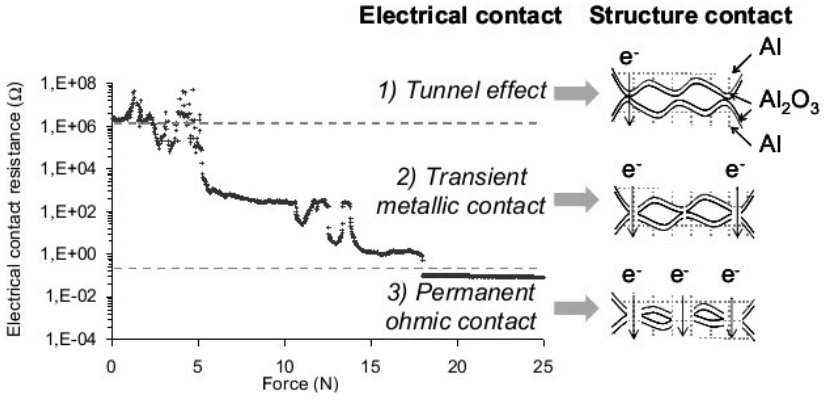

Fig. 1.23 Evolution of the contact resistance as a function of the applied force [79]

Due to our typical expected contact spot dimensions ($< 1\,\mu m$) compared with the electron mean free path (50 nm), ballistic transport will have to be considered in addition to diffusive. This means that the fractional real area of contact is not sufficient; the contact mechanics model should give us an estimate of the individual size of contact spots.

The question of oxide elimination, which is very sensitive to the yet unknown contact stresses, will also have to be examined. Then, a bibliographical study of possible conduction modes through the insulator is presented in next section.

1.3.2.3 Electrical conduction modes in the insulators

An Ohmic conduction governs the electrical conduction in the so-called "electrical conductors" – *i.e.* a linear relation between voltage U and current I ($U = I \cdot R$). Even if an insulator is supposed to prevent the flow of current, in fact it gives way to small currents when the electrical field or temperature is sufficiently high.

The electrical conduction in a composite material can be represented by the energy band model. In the case of a Metal-Oxide-Metal (MIM) capacitor, the energy band in the rest state and in the case of an external voltage U_{ext} applied at one electrode is shown in Figure 1.24 (both metal electrodes are identical).

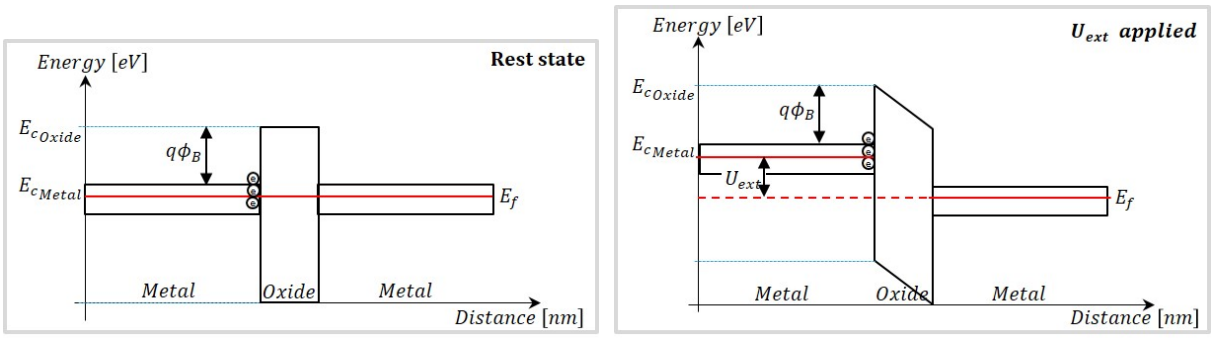

(a) (b)

Fig. 1.24 Simplified scheme of the band structure of a MIM capacitor consisting of metal, oxide, and metal (both metals are identical) illustrating a) a rest state, and b) an external voltage U_{ext} applied [81]

Figure 1.24a shows the Fermi level E_F (electrochemical potential of electrons) in equilibrium, $q\phi_B$ is the thermodynamic work (required to remove an electron from the material to a state of zero total energy E_F), q is the electron charge and ϕ_B is the junction barrier height.

Figure 1.24b shows an external voltage U_{ext} applied in the electrodes that modifies the band diagram; now the Fermi level E_F is not in equilibrium (pointed lines represent the rest position), the $-q\phi_B$ energy is deformed to conserve the equilibrium.

The conduction mode originates from a single or multiple conduction mechanisms. Two groups of conduction mechanisms can be defined, depending on electrical properties of either the insulator material or the electrode-dielectric contact [82–84]:

1.3.2.3.1 Electrode-limited conduction mechanism Electrode-limited conduction mechanisms, depend on electrical properties at the electrode-dielectric contact.

Schottky emission Also known as thermo-ionic emission, an electron flux is obtained by a thermal excitation of carriers – *i.e.* enough energy to overcome a potential-energy barrier (Figure 1.25). The electrons at one metal side overcome the energy barrier at the interface to go to the other metal electrode – *i.e.* without the application of a strong voltage. The Schottky emission is the most frequent conduction mechanism at high temperature.

The current density J_{SE} of Schottky emission can be related to the electric field (ξ) and temperature (T) by:

$$J_{SE} = \frac{4\pi q m^* (kT)^2}{h^3} \cdot \left[\frac{-q\left(\phi_B - \sqrt{\frac{q\xi}{4\pi\varepsilon}}\right)}{kT} \right] \tag{1.36}$$

Where q is the electron charge, m^* is the effective electron mass in the oxide, k is the Boltzmann's constant, h is Planck's constant, ϕ_B is the junction barrier height, ξ is the electric field across the oxide and ε is the permittivity of the oxide.

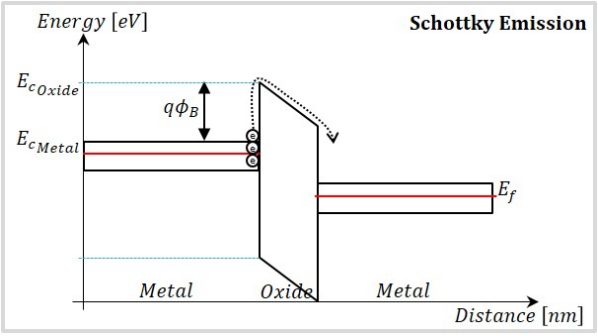

Fig. 1.25 Scheme of the band structure for a thermo-ionic emission

Figure 1.25 shows the band structure of MIM configuration, with a small voltage applied in the metal of left side. The electrons are agitated thermally (not necessarily by the electric field applied) and overcome the junction barrier through the oxide.

Fowler-Nordheim (FN) tunnelling If the applied electric field is large enough at an electrode side, the electrons see a triangular barrier, which they can cross to reach the conduction band of the second electrode and generate a tunnel current (Figure 1.26). At low temperature (room temperature), the Schottky emission is suppressed and tunnelling current is dominant.

The current density J_{FN} of Fowler-Nordheim tunnelling can be related to the electric field (ξ) by:

$$J_{FN} = \frac{q^2}{8\pi h\phi_B} \cdot \exp\left[\frac{-8\pi\sqrt{2qm^*}}{3h\xi}\right] \tag{1.37}$$

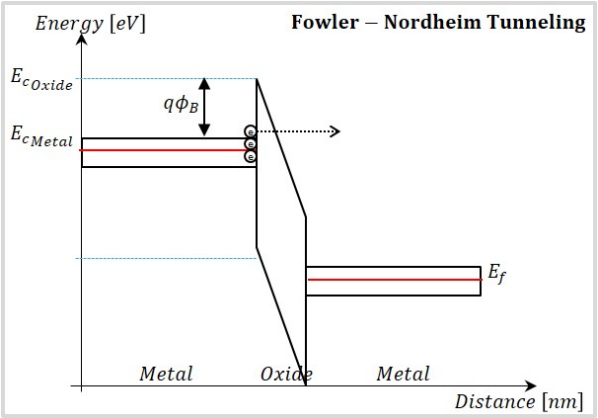

Fig. 1.26 Scheme of the band structure for a Fowler - Nordheim tunnelling

Figure 1.26 shows the band structure of MIM configuration, with a high voltage applied in the metal of left side. The band gap is deformed and narrower, allowing a carrier flow through the oxide.

Direct tunnelling Uses the same principle of FN tunnelling, the difference lies in the applied voltage and the insulator thickness. Therefore, direct tunnelling is more dominant in oxide thinner than 3 nm [84] – *i.e.* FN tunnelling is dominant at thicker oxide and higher electric field. If the voltage across the insulator is small, the electrons see the oxide thickness and the current flows thanks to direct tunnelling through the oxide (Figure 1.27).

The current density J_{DT} of direct tunnelling can be approximated by:

$$J_{DT} \approx \exp\left[\frac{-8\pi\sqrt{2q}}{3h} \cdot \sqrt{m^*\phi_B} \cdot \varkappa \cdot t_{eot}\right] \tag{1.38}$$

Where $\varkappa$ is the relative dielectric constant of the oxide layer and t_{eot} is the equivalent oxide thickness.

The direct tunnelling occurs when the carriers are excited and allowed to cross the band gap (thinner than *FN* tunnelling case).

1.3.2.3.2 Bulk-limited conduction mechanism The bulk-limited conduction mechanisms depend only on the properties of the dielectric itself.

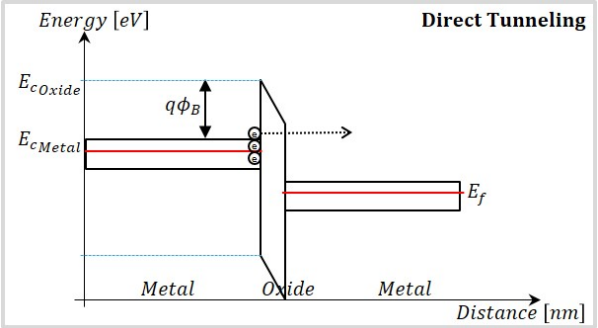

Fig. 1.27 Scheme of the band structure for a direct tunnelling

Poole-Frenkel (PF) emission It is very similar to Schottky emission, *i.e.* the conduction is granted by existing traps assisted by an electric field (descending the potential barrier for the injection into the traps). Therefore, PF emission is also called internal Schottky emission (Figure 1.28). The carriers jump from trap to trap, which seems a thinner oxide to the electrons.

The current density J_{PF} can be expressed as:

$$J_{PF} = q\mu N_C \xi \cdot \exp\left[\frac{-q\left(\phi_T - \sqrt{\frac{q\xi}{\pi\varepsilon}}\right)}{kT}\right] \tag{1.39}$$

Where μ is the electronic mobility, N_C is the density of states in conduction band and ϕ_T is the depth of traps potential well.

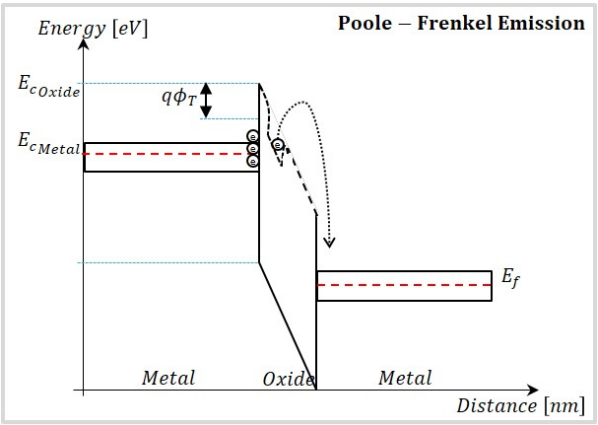

Fig. 1.28 Scheme of the band structure for a Poole-Frenkel emission

Space-charge-limited conduction (SCLC) This mechanism is similar to the transport conduction of electron in a vacuum diode. One metallic side is heated, the excited atoms within the metal emit electrons which are accelerated across the insulator between the electrodes.

Ionic conduction As the name says, this conduction results from the movement of ions caused by an electric field. The ions move between traps in the dielectric to traverse the insulator thickness.

Grain-boundary-limited conduction The grain boundary resistivity is not negligible in the total resistivity of the insulator. In a polycrystalline material the resistivity of the grain boundaries can be higher than that of the grain itself.

The resume of equations and the voltage/temperature dependence for each conduction process are presented in Table 1.3.

Process	Expression	Voltage(V)& temperature(T)dependence
Thermionic emission	$J = A^* \cdot T^2 \cdot \exp\left[\frac{-q\left(\phi_B - \sqrt{\frac{q\phi_i}{4\pi\varepsilon_i}}\right)}{kT}\right]$	$\propto T^2 \cdot \exp\left[\frac{q}{kT}(a\sqrt{V} - \phi_B\right]$
FN Tunnelling	$J \propto \xi_i^2 \cdot \exp\left[-\frac{4\sqrt{2m^*}\cdot(q\phi_B)^{3/2}}{3q\hbar\xi_i}\right]$	$\propto V^2 \cdot \exp\left(-\frac{b}{V}\right)$
PF emission	$J \propto \xi_i \cdot \exp\left[\frac{-q\left(\phi_B - \sqrt{\frac{q\xi_i}{\pi\varepsilon_i}}\right)}{kT}\right]$	$\propto V \cdot \exp\left[\frac{q}{kT}(2a\sqrt{V} - \phi_B)\right]$
Ohmic	$J \propto \xi_i \cdot \exp\left(-\frac{\triangle E_{ac}}{kT}\right)$	$\propto V \cdot \exp\left(\frac{-c}{T}\right)$
Ionic conduction	$J \propto \frac{\xi_i}{T} \cdot \left(-\frac{\triangle E_{ai}}{kT}\right)$	$\propto \frac{V}{T} \cdot \left(\frac{-d}{T}\right)$
Space-charge-limited	$J = \frac{9\varepsilon_i \mu V^2}{8d^3}$	$\propto V^2$

Table 1.3 Basic conduction processes in insulators [84]

where, A^*= effective Richardson constant ($A^* = \frac{4\pi q m^*}{h^3}$), ϕ_B= barrier height, ξ_i=electric field in insulator, ε_i=insulator permittivity, m^*=effective mass, k is the Boltzmann constant, d=insulator thickness, $\triangle E_{ac}$=activation energy of electrons, $\triangle E_{ai}$=activation energy of ions. $V \approx \xi_i d$, $a = \sqrt{\frac{q}{4\pi\varepsilon_i d}}$, b, c, and d are constants.

The dielectric is an undesirable material that prevents an electrical contact – in the best case, it allows a weak current flow. The dielectric observed in this work grows from an *Al-Cu* thin layer. The sample itself is manufactured using photolithography process, which involves several chemical steps – *e.g.* etching, polishing, and cleaning. All this chemical process contributes to generate a native oxide that is not a standard Al_2O_3 oxide with well-known characteristics.

1.4 MEMS reliability

In order to analyze the reliability of MEMS system, one must understand the possible ways in which the system may fail. Through the study of MEMS reliability, we can ensure a durable functioning of these devices in time. Depending on the type of MEMS, the failure modes can be of diverse origin, and tests to detect and prevent failures will be also different. Therefore, and in accordance with the type of structures studied, many failure sources can be related to failure devices, among others: Mechanical fracture, stiction, wear, delamination, vibration and shocks, electrostatic discharge and dielectric charging, radiation effects, temperature, humidity.

In this work the reliability is studied among three axes: the mechanical, the thermal and the contact issues.

1.4.1 Mechanical issues

The moving parts of MEMS devices makes it vulnerable to material flaws. Thus, material issues in MEMS can be divided into three categories:

The material set: The interest of integrating the MEMS device in the microelectronics component, forces us to use the CMOS facilities – *i.e.* only a limited range of materials may be used in fabrication flow [15, 31, 12].

In order to ensure the material compatibility and a reliable process integration, any new material used has to be tested. The fabrication and testing time can take several months. Even a compromise between higher mechanical performances and optimal transducer elements (electrical, thermal, oxidation) should be found.

The principal materials used in CMOS fabrication include: Silicon wafers as the substrate and deposited layers of: Polycrystalline silicon for resistive elements; aluminium and copper as conductor; silicon dioxide, silicon nitride and titanium nitride as electrical insulation and/or passivation.

The manufacturing process: Like in the previous section, the new structure must be compatible with CMOS manufacturing process – *i.e.* photolithography, additive processes, planarization, bonding. Additionally, to create a free-standing part into the CMOS device, an etching step in fabrication process is then added. This extra manufacturing step, which normally is an etch of sacrificial SiO_2, adds chemical contamination [85].

Likewise, the stress generated in the different fabrication steps causes reliability problems (Figure 29) and reduces the operating performance in service of electronic devices. The known

failure mechanisms are principally: voids [86, 87]; hillocks [88]; cracks – which impede a proper functioning of the system.

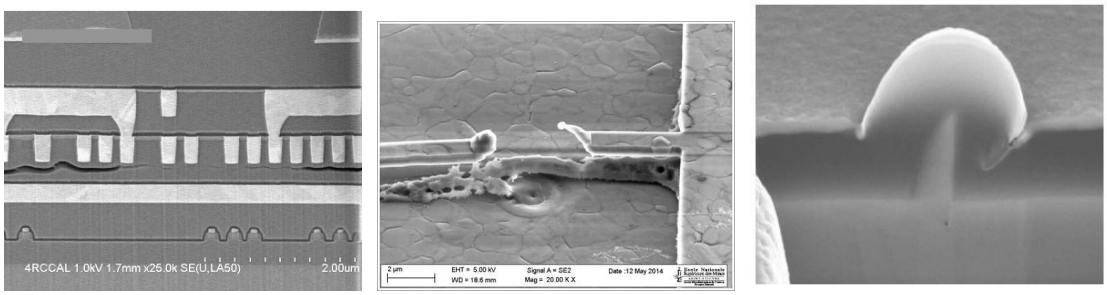

(a) (b) (c)

Fig. 1.29 Defaults caused by mechanical stress, a) cracking, b) voids in an *Al* line, c) hillock

The specific design: The simulation tools help to create the device with a reduced number of prototypes, reducing the cost of final product. The mechanical properties of materials may vary considerably between macro- and micro-scale. These differences should be considered in order to create a robust and durable design:

Elastic properties, essential for accurate performance, principally in cantilever beams and diaphragm devices [4, 89].

Strength. The MEMS devices being exposed to large deflexion levels. The strength of both ductile and brittle materials can be very dependent on the scale and fabrication flow [90].

Even if the thermal issues can be treated in the mechanical part, the thermal actuation of the devices suggests a separate study.

1.4.2 Thermal issues

The electrical actuation by Joule heating induces high temperatures *e.g.* in the contact zone and in the geometrical constrictions [91]. The thermal actuation cycles undergone by the structure along its life generate additional thermal stress [92]. As the device is made out of *Al*, the critical point is the contact zone, which can reach quickly very high temperatures compared with the melting temperatures.

The contact is reached in a “hot switching” actuation mode, on a rough surface, this generates a concentration of electric flow. The anode temperature increase caused by a current

flux is not easily calculated. If a semi-infinite solid at ambient temperature is considered and with a constant electron flow – *i.e.* increase the temperature in the surface – a rough estimation of the temperature (T) at the surface can be calculated using the Carslaw expression [93]:

$$T = \frac{2F_0}{K}\sqrt{\frac{Kt}{\pi\rho_m c}} \tag{1.40}$$

where F_0 is the constant electron flow, K is the thermal conductivity of electrode material, ρ_m is the material density, t is the time and c the specific heat. Poulain et al. [94] used this equation to study the temperature in function of time with gold (Au), ruthenium (Ru) and platinum (Pt) as electrode materials.

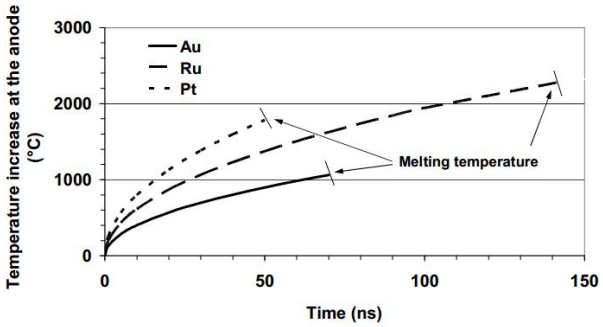

Fig. 1.30 Estimation of anode heating, the melting point are indicated and the time to reach it [94]

All three materials (Au, Ru and Pt) studied by Poulain et al. [94], shown in Figure 1.30, reach temperatures over 1000 °C very quickly – *i.e.* before 50 ns.

Using Equation 1.40 to calculate the time when an aluminum contact reaches the melting temperature (660 °C) is then estimated. Therefore, for Al electrodes, where K=237 $\mathrm{W\,m^{-1}\,K^{-1}}$, ρ=2700 $\mathrm{kg\,m^{-3}}$ and c=900 $\mathrm{J\,kg^{-1}\,K^{-1}}$ [41] (using $F_0 = 0.1 \times 10^{12}\,\mathrm{W\,m^{-2}}$ [94]), 660 °C is reached at 20 ns, an almost instantaneous heating.

1.4.3 Contact issues

Gold, ruthenium and platinum are often used in electro-mechanical contacts due to their good electrical conductivity and corrosion resistance [94, 95]. However, as already mentioned, in this work, only aluminium is used for its easy integration in a CMOS fabrication and its good electrical conductivity ($2.8 \times 10^{-8}\,\Omega\,\mathrm{m}$).

The contact issues are related to the degradation of metal contact during switch operation, which has the effect of degrading the quality of the metal-metal contacts.

Two types of contact exist: "hot switching" is when switching occurs with a signal or potential across the electric contact, "cold switching" when no field exists across the contacts as the switch opens or closes.

The main reliability problems related to the contact are:

1.4.3.1 Surface contamination

Usually from the manufacturing stage, the surface contamination prevents good electrical contact [96]. In some cases, depending on the material used, the contamination can even help the development of insulating oxide in the surface. This is the case with *Al*, which oxidizes in contact with air. The thickness of this contamination layer depends on the chosen material, the fabrication process and the operating environment [97].

The switch operation can also generate contamination in the surfaces in contact. The friction of surfaces at nanoscale should be considered [98], this friction can generate polymer formation or accumulation of the contamination [99].

1.4.3.2 Electric arc

The electrical arc failure is associated to "hot switching" operation mode [15]. Thanks to small separation of electrodes and the applied electrical current the formation of an electrical arc is possible. Therefore, if the voltage between electrodes is larger than the ionization voltage of the gas between the electrodes an arc can be produced.

The arc generation is defined by Paschen's corrected formula [94] which links the breakdown voltage (V_B) to the product of the gas pressure (p_g) by the gap distance (d).

$$V_B = \frac{B^* p_g d}{\ln(A^* p_g d) - \ln\left[\ln\left(1 + \frac{1}{\gamma_{se}}\right)\right]} \tag{1.41}$$

Where γ_{se} is the secondary electron emission coefficient at the cathode, A^* is the saturation ionization in the gas at given U/p_g, and B^* is a constant related to the excitation and ionization energies.

Figure 1.31 show a typical curve for air, nitrogen and hydrogen at 1 atm, with a minimum value for air at 327 V – *i.e.* Paschen minimum.

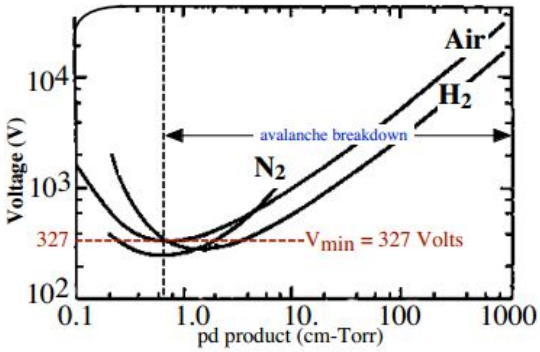

Fig. 1.31 The Paschen curve for dry air, nitrogen and hydrogen [94]

The minimum in this curve occurs when the electronic mean free path is just barely sufficient to allow electrons to gain the ionization energy.

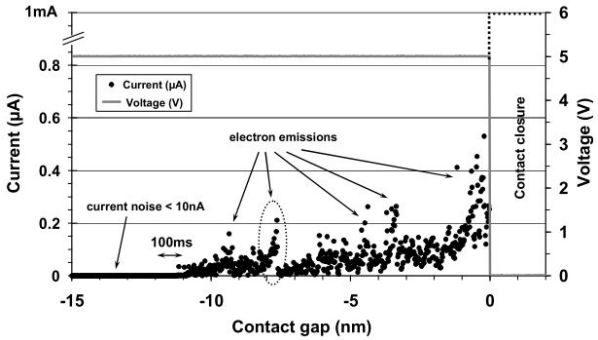

Fig. 1.32 Typical evolution of the current and voltage as the function of the contact gap just before contact closure [94]

In Figure 1.32 (Poulain et al. [94]) an electric current is measured although the two Au/Au electrodes are separated by 10 nm. Several irregular current peaks of a few hundreds of nA are observed.

1.4.3.3 Material transfer phenomena

Material transfer or sintering is another phenomenon observed in "hot switching" (Figure 1.33) [94]. If anode and cathode surfaces approach (a), the roughness amplifies the electric field (ξ) locally by tip effect (b), β' is an amplification factor. Then the contact surfaces are sufficiently close to trigger the electron flux by Fowler-Northeim effect (c). The electron flux collides with the anode, locally heating the anode (d) and causing evaporation (e).

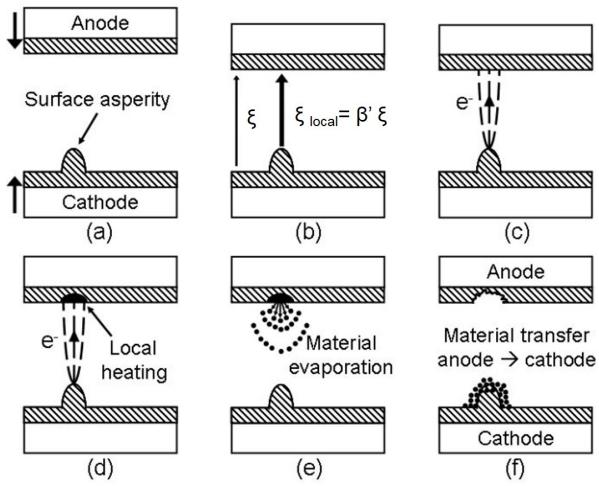

Fig. 1.33 Scheme of a material transfer mechanism in a contact [94]

A compromise can be found on the initial roughness of the contact surface. The rougher the surface is, the worse the electrical contact (too few contact spots). A large contact force can be needed to grant electrical contact by flattening asperities and increasing the real contact area. Nevertheless, if after repetitive contact the surfaces become too smooth, a risk of stiction between moving parts appears.

1.4.3.4 Stiction

The stiction is an adhesion of surfaces of mobile part – *e.g.* contacting parts. Stiction occurs either in fabrication process or in operation life of device. The main mechanisms of adhesion are [100, 101]:

Capillary forces, Also known as meniscus forces, they are due to liquid residues. In the MEMS technologies, a poorly controlled packaging is the origin of this liquid. The capillarity force (F_m) for a sphere/plane contact is defined by [102]:

$$F_m = 4\pi\beta\gamma_{1v}\cos(\theta) \tag{1.42}$$

where γ_{1v} is the surface tension of water (72.8 mN m^{-1} at 20 °C), β the radius of the sphere and θ the contact angle.

Hydrogen bridging, Hydrophilic silicon surfaces contain adsorbed water layers generating hydroxyl groups. When the contact is closing, hydroxyl groups can form strong hydrogen bonds.

Electrostatic forces, They are generated by the Coulomb attraction between charged surfaces in contact – *e.g.* polarised from contact potential during actuation. It is caused by differences in the local energy states and electron work functions, the energy is:

$$F(x) = \frac{1}{2}\varepsilon_{air} S \frac{U^2}{d^2(x)} \tag{1.43}$$

Where U is the potential difference between surfaces, S is the electrode surface, d is the initial gap, x is the displacement and ε_{air} the air permittivity. At small separations ($\sim$100 nm), electrostatic forces equal Van der Waals forces.

Van der Waals forces, Van der Waals forces result from the interaction between instantaneous dipole moment of atoms. The attractive force of Van der Waals and the repulsive force of Born are included in this kind of adhesives forces. The Van der Waals force (F_{VDW}) in given in function of the separation (d) by [103]:

$$F_{VDW}(d) = -\frac{A_H}{6\pi d^3} \tag{1.44}$$

where A_H is the Hamaker constant ($\sim 2.8 \times 10^{-19}$J [103]).

Figure 1.34 shows the bond strength in function of separation distance between electrodes for all the forces described above.

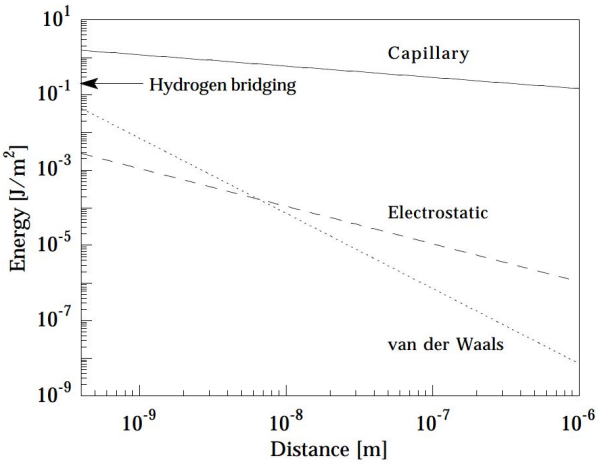

Fig. 1.34 The Bonding energy in function to separation between two electrodes (sphere-plane model)[104]

The capillarity energy was calculated for water using a surface tension of 73 mN m^{-1} and a contact angle of zero degrees with a reference distance d of 2 µm. For the electrostatic energy a

voltage difference of 0.5 V was used and for the Van del Waals energy a Hamaker's constant of silicon in air equal to 27×10^{-20} J has been used.

Summary

This chapter has given a brief description of Microsystems – also known as Micro-electro-mechanical systems or just MEMS. The MEMS devices are generally designed either to measure a physical variable (sensor) or to perform some functionality (actuator).

This kind of devices are in continuous evolution. During the last years, it moved from standalone parts to complex Systems on Chip (SoC). This evolution is justified by More than Moore evolution principle, which tends to integrate additional functionalities in a single chip. This integration is the source of many issues in the fabrication process, which are studied in this chapter.

In the first part of this chapter, the CMOS-MEMS are presented. After presenting several models, the BEOL-MEMS concept is chosen to make our device, because it allows an easy integration on CMOS process flow. Then, a study about mechanical stress in Al metallic layer is carried out. This study helps to understand the mechanisms developed during fabrication process, which cause stress in the final product. This residual stress, normally harmful to the devices is used on our structure as a trigger of a switch function.

A thermo-electro-mechanical switch embedded in the BEOL (*Al*) of CMOS technologies is presented in chapter 2, which is activated by the Joule effect.

The physics of the contact, both mechanical and electrical, is studied next. The mechanical part of the contact, is explained thanks to different approaches: statistic, fractal, and deterministic models. The contact in the structures is performed by a lateral movement, so the contact surfaces, perpendicular to the plane, are difficult to study.

As the switch is made of aluminium, an oxide layer of $(2 \text{ to } 4)\,\text{nm}$ will grow on the surface, including the contact area. This oxide prevents an ohmic electric conduction, so other conduction mechanisms are studied.

After reviewing the different electrical conduction modes in the insulators, the *Fowler-Nordheim* tunnelling effect should be considered.

The final part of this chapter is dedicated to the study of MEMS reliability. Three parts were presented:

- The mechanical issues, in particular the manufacturing problems and the harmful stress. Both must be considered in the manufacture of the device.
- The thermal issues, the 'hot switching' mode is explained. High temperatures, around 660 °C (melting point of *Al*) can be achieved in some 50 ns for an electrodes made out of aluminium.
- The contact issues, the risks of electric arcs and sintering are studied for an operation mode. The stiction is also studied, which can be present during manufacturing or operation mode.

This bibliographical chapter gives us the fundamental understanding of the physical principles discussed later in this thesis. Not only for the manufacturing stage, but also for the actuation and robustness studies.

Résumé français

Une description des microsystèmes est réalisée dans ce chapitre – dispositifs connus par leur acronyme anglais MEMS (Micro-electro-mechanical systems). Les MEMS sont généralement conçus soit pour transformer l'état d'une grandeur physique observée en une grandeur utilisable (capteur), soit pour convertir un signal physique en un autre (transducteur).

Ce type de dispositifs est en permanent évolution, et ces dernières années ils sont passés d'un mode de fonctionnement autonome à une participation à un système plus complexe – Système sur une puce (SoC, de son acronyme en anglais System-on-Chip). Une telle transformation est justifiée par le principe "More than Moore", qui contrairement au principe "More Moore" qui cherche à diminuer la taille des dispositifs, vise à intégrer des fonctionnalités supplémentaires dans une seule puce. Cette intégration est une source de nombreux problèmes étudiés dans ce chapitre.

Dans la première partie de ce chapitre, les dispositifs *CMOS-MEMS* sont présentés. Le concept *BEOL-MEMS* est choisi parmi d'autres méthodes pour réaliser nos dispositifs, du fait de leur intégration simplifiée dans un procédé de fabrication CMOS. Ensuite, une étude sur la contrainte mécanique dans la couche métallique d'Aluminium est réalisée. Cette étude aide à la compréhension des mécanismes qui provoquent l'état des contraintes dans le produit final. Cette contrainte résiduelle, nocive pour la plupart des applications, est utilisée dans la structure comme déclencheur d'une fonction de commutation.

Un commutateur thermo-électro-mécanique, intégré dans le *BEOL* (*Al*) des technologies CMOS et activé par l'effet Joule est étudié dans ce travail de thèse.

La physique du contact, à la fois mécanique et électrique est étudiée ensuite. La partie mécanique du contact est expliquée à travers différents approches : statistique, fractal, et déterministe. Comme nous ne connaissons pas les surfaces étudiées (contact latéral), la partie mécanique du contact reste difficile à modéliser.

Comme l'interrupteur est fait en aluminium, une couche d'oxyde de 2 nm to 4 nm croît sur la surface, notamment dans la zone de contact. Cet oxyde empêche une conduction électrique ohmique ; ainsi d'autres mécanismes de conduction sont étudiés. Après avoir examiné les

différents modes de conduction électrique dans les isolants, l'effet tunnel Fowler-Nordheim semble être le plus approprié à étudier.

La dernière partie de ce chapitre est consacrée à l'étude de la fiabilité des MEMS. Trois parties sont traitées ici :

- Les problèmes mécaniques, en particulier les problèmes de fabrication et la contrainte résiduel sont étudiés.
- Les problèmes thermiques : le mode de "commutation à chaud" est expliqué. Pour des électrodes faites en aluminium, des températures d'environ 660 °C (point de fusion de l'*Al*) peuvent être atteintes en moins de 50 ns.
- Les problèmes de contact, les risques d'arcs électriques et le frittage sont étudiés. L'adhérence est également étudiée, qui peut être présente lors de la fabrication ou pendant le fonctionnement de la structure.

Ce chapitre bibliographique nous donne les bases pour comprendre les principes physiques discutés plus loin dans ce manuscrit, pour l'étape de fabrication, mais aussi pour les études d'actuation et de robustesse de la structure.

Bibliography

[1] H. Nathanson, W. Newell, R. Wickstrom, and J. Davis, "The resonant gate transistor," *IEEE Transactions on Electron Devices*, vol. 14, no. 3, pp. 117–133, mar 1967. [Online]. Available: http://ieeexplore.ieee.org/lpdocs/epic03/wrapper.htm?arnumber=1474635 2

[2] M. Parameswaran, H. Baltes, and A. Robinson, "Polysilicon microbridge fabrication using standard CMOS technology," in *IEEE Technical Digest on Solid-State Sensor and Actuator Workshop*. IEEE, 1988, pp. 148–150. [Online]. Available: http://ieeexplore.ieee.org/lpdocs/epic03/wrapper.htm?arnumber=26463 2, 5, 7

[3] G. Moore, "Cramming More Components Onto Integrated Circuits," *Proceedings of the IEEE*, vol. 86, no. 1, pp. 82–85, jan 1998. [Online]. Available: http://ieeexplore.ieee.org/lpdocs/epic03/wrapper.htm?arnumber=658762 2

[4] S. D. Senturia, *Microsystem Design*. Boston: Kluwer Academic Publishers, 2002. [Online]. Available: http://link.springer.com/10.1007/b117574 4, 36

[5] H. Fujita, "Microactuators and micromachines," *Proceedings of the IEEE*, vol. 86, no. 8, pp. 1721–1732, 1998. [Online]. Available: http://ieeexplore.ieee.org/lpdocs/epic03/wrapper.htm?arnumber=704278 4

[6] R. E. Pearson, L. F. Fuller, and I. Puchades, "MEMS Fabrication Course for Pressure Sensors, Flow Sensors, Fluidic Channels and Micro-Pumps," in *2008 17th Biennial University/Government/Industry Micro/Nano Symposium*. IEEE, jul 2008, pp. 70–74. [Online]. Available: http://ieeexplore.ieee.org/lpdocs/epic03/wrapper.htm?arnumber=4573204 4

[7] L. Hornbeck, "Digital Light Processing and MEMS: an overview," in *Digest IEEE/Leos 1996 Summer Topical Meeting. Advanced Applications of Lasers in Materials and Processing*. IEEE, 1996, pp. 7–8. [Online]. Available: http://ieeexplore.ieee.org/lpdocs/epic03/wrapper.htm?arnumber=540770 4

[8] P. Gilgunn, Jingwei Liu, N. Sarkar, and G. Fedder, "CMOS–MEMS Lateral Electrothermal Actuators," *Journal of Microelectromechanical Systems*, vol. 17, no. 1, pp. 103–114, feb 2008. [Online]. Available: http://ieeexplore.ieee.org/lpdocs/epic03/wrapper.htm?arnumber=4441701 4

[9] D. Dellaert and J. Doutreloigne, "Modeling and simulation of a MEMS thermal actuator with polysilicon heater," in *2014 15th International Conference on Thermal, Mechanical and Mulit-Physics Simulation and Experiments in Microelectronics and Microsystems (EuroSimE)*. IEEE, apr 2014, pp. 1–6. [Online]. Available: http://ieeexplore.ieee.org/lpdocs/epic03/wrapper.htm?arnumber=6813800 4

[10] A. A. Fomani, S. Fouladi, and R. R. Mansour, "Magnetically-actuated dielectric cantilever RF MEMS switches," in *2010 IEEE MTT-S International Microwave Symposium*. IEEE, may 2010, pp. 296–299. [Online]. Available: http://ieeexplore.ieee.org/lpdocs/epic03/wrapper.htm?arnumber=5516847 4

[11] A. Flynn, L. Tavrow, S. Bart, R. Brooks, D. Ehrlich, K. Udayakumar, and L. Cross, "Piezoelectric micromotors for microrobots," *Journal of Microelectromechanical Systems*, vol. 1, no. 1, pp. 44–51, mar 1992. [Online]. Available: http://ieeexplore.ieee.org/lpdocs/epic03/wrapper.htm?arnumber=128055 4

[12] T. Scheiter, H. Kapels, K.-G. Oppermann, M. Steger, C. Hierold, W. Werner, and H.-J. Timme, "Full integration of a pressure-sensor system into a standard BiCMOS process," *Sensors and Actuators A: Physical*, vol. 67, no. 1-3, pp. 211–214, may 1998. [Online]. Available: http://linkinghub.elsevier.com/retrieve/pii/S0924424798000296 4, 6, 35

[13] D. Tanner, S. Swanson, J. Walraven, and J. Dohner, "On-chip monitoring of MEMS gear motion," in *2003 IEEE International Reliability Physics Symposium Proceedings, 2003. 41st Annual.* IEEE, 2003, pp. 484–490. [Online]. Available: http://ieeexplore.ieee.org/lpdocs/epic03/wrapper.htm?arnumber=1197796 4

[14] S. Fuller, E. Wilhelm, and J. Jacobson, "Ink-jet printed nanoparticle microelectromechanical systems," *Journal of Microelectromechanical Systems*, vol. 11, no. 1, pp. 54–60, 2002. [Online]. Available: http://ieeexplore.ieee.org/lpdocs/epic03/wrapper.htm?arnumber=982863 4

[15] G. Rebeiz and J. Muldavin, "RF MEMS switches and switch circuits," *IEEE Microwave Magazine*, vol. 2, no. 4, pp. 59–71, 2001. [Online]. Available: http://ieeexplore.ieee.org/lpdocs/epic03/wrapper.htm?arnumber=969936 4, 5, 35, 38

[16] K. E. Petersen, "Micromechanical Membrane Switches on Silicon," *IBM Journal of Research and Development*, vol. 23, no. 4, pp. 376–385, jul 1979. [Online]. Available: http://ieeexplore.ieee.org/lpdocs/epic03/wrapper.htm?arnumber=5390793 4

[17] H. A. C. Tilmans, W. D. Raedt, and E. Beyne, "MEMS for wireless communications: from RF-MEMS components to RF-MEMS-SiP," *Journal of Micromechanics and Microengineering*, vol. 13, no. 4, pp. S139–S163, jul 2003. [Online]. Available: http://stacks.iop.org/0960-1317/13/i=4/a=323?key=crossref.4a17c2bc03c87d450a0fe82a4c3f8efb 5

[18] T. Gomm, L. L. Howell, and R. H. Selfridge, "In-plane linear displacement bistable microrelay," *Journal of Micromechanics and Microengineering*, vol. 12, no. 3, pp. 257–264, may 2002. [Online]. Available: http://stacks.iop.org/0960-1317/12/i=3/a=310?key=crossref.e68444ced807fdd85277215adce7eb47 5

[19] M. Baker and L. Howell, "On-chip actuation of an in-plane compliant bistable micromechanism," *Journal of Microelectromechanical Systems*, vol. 11, no. 5, pp. 566–573, oct 2002. [Online]. Available: http://ieeexplore.ieee.org/lpdocs/epic03/wrapper.htm?arnumber=1038852

[20] N. Masters and L. Howell, "A self-retracting fully compliant bistable micromechanism," *Journal of Microelectromechanical Systems*, vol. 12, no. 3, pp. 273–280, jun 2003. [Online]. Available: http://ieeexplore.ieee.org/lpdocs/epic03/wrapper.htm?arnumber=1203765

[21] Jin Qiu, J. Lang, A. Slocum, and A. Weber, "A bulk-micromachined bistable relay with U-shaped thermal actuators," *Journal of Microelectromechanical Systems*, vol. 14, no. 5, pp. 1099–1109, oct 2005. [Online]. Available: http://ieeexplore.ieee.org/lpdocs/epic03/wrapper.htm?arnumber=1516192 5

[22] M. Sterner, N. Roxhed, G. Stemme, and J. Oberhammer, "Coplanar-waveguide embedded mechanically-bistable DC-to-RF MEMS switches," in *2007 IEEE/MTT-S International Microwave Symposium*. IEEE, jun 2007, pp. 359–362. [Online]. Available: http://ieeexplore.ieee.org/lpdocs/epic03/wrapper.htm?arnumber=4263822 5

[23] M. Daneshmand, S. Fouladi, R. Mansour, M. Lisi, and T. Stajcer, "Thermally Actuated Latching RF MEMS Switch and Its Characteristics," *IEEE Transactions on Microwave Theory and Techniques*, vol. 57, no. 12, pp. 3229–3238, dec 2009. [Online]. Available: http://ieeexplore.ieee.org/lpdocs/epic03/wrapper.htm?arnumber=5337885 5

[24] W.-C. Chen, C.-C. Chu, J. Hsieh, and W. Fang, "A reliable single-layer out-of-plane micromachined thermal actuator," *Sensors and Actuators A: Physical*, vol. 103, no. 1-2, pp. 48–58, jan 2003. [Online]. Available: http://linkinghub.elsevier.com/retrieve/pii/S0924424702003151 5

[25] D. Girbau, M. A. Llamas, J. Casals-Terre, X. Simo-Selvas, L. Pradell, and A. Lazaro, "A Low-Power-Consumption Out-of-Plane Electrothermal Actuator," *Journal of Microelectromechanical Systems*, vol. 16, no. 3, pp. 719–727, jun 2007. [Online]. Available: http://ieeexplore.ieee.org/lpdocs/epic03/wrapper.htm?arnumber=4276802 5

[26] W. Taylor, O. Brand, and M. Allen, "Fully integrated magnetically actuated micromachined relays," *Journal of Microelectromechanical Systems*, vol. 7, no. 2, pp. 181–191, jun 1998. [Online]. Available: http://ieeexplore.ieee.org/lpdocs/epic03/wrapper.htm?arnumber=679353 5

[27] S. Zhang, W. Su, M. Zaghloul, and B. Thibeault, "Wideband CMOS Compatible Capacitive MEMS Switch for RF Applications," *IEEE Microwave and Wireless Components Letters*, vol. 18, no. 9, pp. 599–601, sep 2008. [Online]. Available: http://ieeexplore.ieee.org/lpdocs/epic03/wrapper.htm?arnumber=4624619 5

[28] G. Fedder, R. Howe, Tsu-Jae King Liu, and E. Quevy, "Technologies for Cofabricating MEMS and Electronics," *Proceedings of the IEEE*, vol. 96, no. 2, pp. 306–322, feb 2008. [Online]. Available: http://ieeexplore.ieee.org/lpdocs/epic03/wrapper.htm?arnumber=4403892 5

[29] R. R. Mansour, "RF MEMS-CMOS Device Integration: An Overview of the Potential for RF Researchers," *IEEE Microwave Magazine*, vol. 14, no. 1, pp. 39–56, jan 2013. [Online]. Available: http://ieeexplore.ieee.org/lpdocs/epic03/wrapper.htm?arnumber=6421094 5

[30] J. Smith, S. Montague, J. Sniegowski, J. Murray, and P. McWhorter, "Embedded micromechanical devices for the monolithic integration of MEMS with CMOS," in *Proceedings of International Electron Devices Meeting*, no. 100. IEEE, 1995, pp. 609–612. [Online]. Available: http://ieeexplore.ieee.org/lpdocs/epic03/wrapper.htm?arnumber=499295 6

[31] R. Gaddi, R. Van Kampen, A. Unamuno, V. Joshi, D. Lacey, M. Renault, C. Smith, R. Knipe, and D. Yost, "MEMS technology integrated in the CMOS back end," *Microelectronics Reliability*, vol. 50, no. 9-11, pp. 1593–1598, sep 2010. [Online]. Available: http://linkinghub.elsevier.com/retrieve/pii/S0026271410003860 7, 35

[32] A. Franke, J. Heck, Tsu-Jae King, and R. Howe, "Polycrystalline silicon-germanium films for integrated microsystems," *Journal of Microelectromechanical Systems*, vol. 12, no. 2, pp. 160–171, apr 2003. [Online]. Available: http://ieeexplore.ieee.org/lpdocs/epic03/wrapper.htm?arnumber=1192710 7

[33] A. K. Stamper, C. V. Jahnes, S. R. Dupuis, A. Gupta, Z.-X. He, R. T. Herrin, S. E. Luce, J. Maling, D. R. Miga, W. J. Murphy, E. J. White, S. J. Cunningham, D. R. DeReus, I. Vitomirov, and A. S. Morris, "Planar MEMS RF capacitor integration," in *2011 16th International Solid-State Sensors, Actuators and Microsystems Conference*. IEEE, jun 2011, pp. 1803–1806. [Online]. Available: http://ieeexplore.ieee.org/lpdocs/epic03/wrapper.htm?arnumber=5969479 7

[34] S. P. Natarajan, S. J. Cunningham, A. S. Morris, and D. R. Dereus, "CMOS integrated digital RF MEMS capacitors," in *2011 IEEE 11th Topical Meeting on Silicon Monolithic Integrated Circuits in RF Systems*. IEEE, jan 2011, pp. 173–176. [Online]. Available: http://ieeexplore.ieee.org/lpdocs/epic03/wrapper.htm?arnumber=5719327 7

[35] G. Fedder, S. Santhanam, M. Reed, S. Eagle, D. Guillou, M.-C. Lu, and L. Carley, "Laminated high-aspect-ratio microstructures in a conventional CMOS process," in *Proceedings of Ninth International Workshop on Micro Electromechanical Systems*. IEEE, 1996, pp. 13–18. [Online]. Available: http://ieeexplore.ieee.org/lpdocs/epic03/wrapper.htm?arnumber=493822 7

[36] H. Xie, L. Erdmann, X. Zhu, K. Gabriel, and G. Fedder, "Post-CMOS processing for high-aspect-ratio integrated silicon microstructures," *Journal of Microelectromechanical Systems*, vol. 11, no. 2, pp. 93–101, apr 2002. [Online]. Available: http://ieeexplore.ieee.org/lpdocs/epic03/wrapper.htm?arnumber=993443 7

[37] G. Fedder, J. G. Kaigham, M. A. Maher, and M. Tamal, "Application-Specific Integrated-Microelectromechanical Systems (MEMS) process services (ASIMPS)," Carnegie Mellon University, New York, Tech. Rep. April, 2005. 7

[38] D. Gardner and P. Flinn, "Mechanical stress as a function of temperature in aluminum films," *IEEE Transactions on Electron Devices*, vol. 35, no. 12, pp. 2160–2169, 1988. [Online]. Available: http://ieeexplore.ieee.org/lpdocs/epic03/wrapper.htm?arnumber=8790 10, 11, 13

[39] R. Abermann, "Measurements of the intrinsic stress in thin metal films," *Vacuum*, vol. 41, no. 4-6, pp. 1279–1282, jan 1990. [Online]. Available: http://linkinghub.elsevier.com/retrieve/pii/0042207X9093933A 10

[40] E. Klokholm and B. S. Berry, "Intrinsic Stress in Evaporated Metal Films," *Journal of The Electrochemical Society*, vol. 115, no. 8, p. 823, 1968. [Online]. Available: http://jes.ecsdl.org/cgi/doi/10.1149/1.2411441 10

[41] L. B. Freund and S. Suresh, *Thin Film Materials*. Cambridge: Cambridge University Press, 2004. [Online]. Available: http://ebooks.cambridge.org/ref/id/CBO9780511754715 12, 13, 37

[42] S. Wolf and R. N. Tauber, *Silicon Processing for the VLSI Era, Vol. 1: Process Technology*, 1st ed. Lattice Press, 1986. 12

[43] I. Ames, F. M. D'Heurle, and R. E. Horstmann, "Reduction of Electromigration in Aluminum Films by Copper Doping," *IBM Journal of Research and Development*, vol. 14, no. 4, pp. 461–463, jul 1970. [Online]. Available: http://ieeexplore.ieee.org/lpdocs/epic03/wrapper.htm?arnumber=5391634 13

[44] W. D. Nix, "Mechanical properties of thin films," *Metallurgical Transactions A*, vol. 20, no. 11, pp. 2217–2245, nov 1989. [Online]. Available: http://link.springer.com/10.1007/BF02666659 13

[45] R. Machunze and G. Janssen, "Stress gradients in titanium nitride thin films," *Surface and Coatings Technology*, vol. 203, no. 5-7, pp. 550–553, dec 2008. [Online]. Available: http://linkinghub.elsevier.com/retrieve/pii/S0257897208003526 13

[46] R. Liu, B. Jiao, Y. Kong, Z. Li, H. Shang, D. Lu, C. Gao, and D. Chen, "Elimination of initial stress-induced curvature in a micromachined bi-material composite-layered cantilever," *Journal of Micromechanics and Microengineering*, vol. 23, no. 9, p. 095019, sep 2013. [Online]. Available: http://stacks.iop.org/0960-1317/23/i=9/a=095019?key=crossref.69e3985166c29b7df348c40da29a80d1 13

[47] S. Wang, J. Chen, D. Li, Y. Huang, Z. Li, and W. Zhang, "Evaluating Interface Effect On Stresses In Thin Films By A Local Curvature Metrology With High Accuracy And Resolution," in *2006 1st IEEE International Conference on Nano/Micro Engineered and Molecular Systems*. IEEE, jan 2006, pp. 1513–1516. [Online]. Available: http://ieeexplore.ieee.org/lpdocs/epic03/wrapper.htm?arnumber=4135231 13

[48] A. Bohg, "Measurement of stresses in thin films on single crystalline substrates," *Physica Status Solidi (a)*, vol. 46, no. 2, pp. 445–450, apr 1978. [Online]. Available: http://doi.wiley.com/10.1002/pssa.2210460206 13

[49] P. Flynn, D. Gardner, and W. Nix, "Measurement and Interpretation of stress in aluminum-based metallization as a function of thermal history," *IEEE Transactions on Electron Devices*, vol. 34, no. 3, pp. 689–699, mar 1987. [Online]. Available: http://ieeexplore.ieee.org/lpdocs/epic03/wrapper.htm?arnumber=1486692 13

[50] L. Maniguet, M. Ignat, M. Dupeux, J. Bacmann, and P. Normandon, "X-ray Determination and Analysis of Residual Stresses in Uniform Films and Patterned Lines of Tungsten," *MRS Proceedings*, vol. 308, p. 285, jan 1993. [Online]. Available: http://journals.cambridge.org/abstract{_}S1946427400320814 13

[51] G. G. Stoney, "The Tension of Metallic Films Deposited by Electrolysis," *Proceedings of the Royal Society A: Mathematical, Physical and Engineering Sciences*, vol. 82, no. 553, pp. 172–175, may 1909. [Online]. Available: http://rspa.royalsocietypublishing.org/cgi/doi/10.1098/rspa.1909.0021 13

[52] N. Schwarzer and F. Richter, "On the Determination of Film Stress from Substrate Bending: STONEY's Formula and Its Limits," TU Chemnitz, Fakultat fur Naturwissenschaften, TU Chemnitz, Germany, Tech. Rep. 1, 2004. 13

[53] R. Jaeger, J. Suhling, R. Ramani, A. Bradley, and Jianping Xu, "CMOS stress sensors on [100] silicon," *IEEE Journal of Solid-State Circuits*, vol. 35, no. 1, pp. 85–95, jan 2000. [Online]. Available: http://ieeexplore.ieee.org/lpdocs/epic03/wrapper.htm?arnumber=818923 14

[54] K. A. Ewuame, V. Fiori, K. Inal, P.-O. Bouchard, S. Gallois-Garreignot, S. Lionti, C. Tavernier, and H. Jaouen, "Investigations of Thermomechanical Stress Induced by TSV-Middle (Through-Silicon via) in 3-D ICs by Means of CMOS Sensors and Finite-Element Method," *IEEE Transactions on Components, Packaging and Manufacturing Technology*, vol. 5, no. 8, pp. 1085–1092, aug 2015. [Online]. Available: http://ieeexplore.ieee.org/lpdocs/epic03/wrapper.htm?arnumber=7164297 14

[55] C. Wilson, A. Horsfall, A. O'Neill, N. Wright, K. Wang, S. Bull, J. Terry, J. M. Stevenson, and A. Walton, "Direct Measurement of Electromigration Induced Stress in Interconnect Structures," in *2006 IEEE International Reliability Physics Symposium Proceedings*, vol. 7, no. 2. IEEE, 2006, pp. 123–127. [Online]. Available: http://ieeexplore.ieee.org/lpdocs/epic03/wrapper.htm?arnumber=4017143 14

[56] M. Kasbari, C. Rivero, S. Blayac, F. Cacho, O. Bostrom, and R. Fortunier, "Direct Local Strain Measurement In Damascene Interconnects," *MRS Proceedings*, vol.

990, pp. 0990–B07–06, jan 2007. [Online]. Available: http://journals.cambridge.org/abstract{_}S1946427400034977 14

[57] A. Horsfall, J. dos Santos, S. Soare, N. Wright, A. O'Neill, S. Bull, A. Walton, A. Gundlach, and J. Stevenson, "A novel sensor for the direct measurement of process induced residual stress in interconnects," in *Electrical Performance of Electrical Packaging (IEEE Cat. No. 03TH8710)*. Estoril, Portugal: IEEE, 2003, pp. 115–118. [Online]. Available: http://ieeexplore.ieee.org/lpdocs/epic03/wrapper.htm?arnumber=1256824 14

[58] R. Vayrette, C. Rivero, B. Gros, S. Blayac, and K. Inal, "Residual stress estimation in damascene copper interconnects using embedded sensors," *Microelectronic Engineering*, vol. 87, no. 3, pp. 412–415, mar 2010. [Online]. Available: http://linkinghub.elsevier.com/retrieve/pii/S0167931709004390 14

[59] R. Holm, *Electric Contacts*, 4th ed. Berlin, Heidelberg: Springer Berlin Heidelberg, 1967. [Online]. Available: http://link.springer.com/10.1007/978-3-662-06688-1 15

[60] J. A. Greenwood and J. B. P. Williamson, "Contact of Nominally Flat Surfaces," *Proceedings of the Royal Society A: Mathematical, Physical and Engineering Sciences*, vol. 295, no. 1442, pp. 300–319, dec 1966. [Online]. Available: http://rspa.royalsocietypublishing.org/cgi/doi/10.1098/rspa.1966.0242 16, 17, 18

[61] H. Hertz, *Miscellaneous papers*. London ; New York : Macmillan, 1896., 1896. [Online]. Available: http://www.archive.org/details/cu31924012500306 16

[62] A. Majumdar and B. Bhushan, "Fractal Model of Elastic-Plastic Contact Between Rough Surfaces," *Journal of Tribology*, vol. 113, no. 1, p. 1, 1991. [Online]. Available: http://link.aip.org/link/JOTRE9/v113/i1/p1/s1{&}Agg=doi 16, 19

[63] R. L. Jackson and J. L. Streator, "A multi-scale model for contact between rough surfaces," *Wear*, vol. 261, no. 11-12, pp. 1337–1347, dec 2006. [Online]. Available: http://linkinghub.elsevier.com/retrieve/pii/S0043164806001359 16, 19, 21

[64] V. A. Yastrebov, J. Durand, H. Proudhon, and G. Cailletaud, "Rough surface contact analysis by means of the Finite Element Method and of a new reduced model," *Comptes Rendus Mécanique*, vol. 339, no. 7-8, pp. 473–490, jul 2011. [Online]. Available: http://linkinghub.elsevier.com/retrieve/pii/S163107211100091X 16, 19

[65] P.-Y. Duvivier, "Etude expérimentale et modelisation du contact electrique et mecanique quasi statique entre surfaces rugueuses d'or : application aux micro-relais MEMS," Ph.D.

dissertation, École Nationale Supérieure des Mines de Saint-Étienne, 2010. 16, 19, 22, 24, 25

[66] B. Arrazat, "Maitrise de la Microstructure de films minces d'or par traitements de surface pour l'optimisation du contact mecanique et ohmique des micro-relais MEMS," Ph.D. dissertation, Ecole Nationale Supérieure des Mines de Saint-Etienne, 2012. 16, 19, 22, 23

[67] K. Kataoka, S. Kawamura, T. Itoh, T. Suga, K. Ishikawa, and H. Honma, "Low contact-force and compliant MEMS probe card utilizing fritting contact," in *Technical Digest. MEMS 2002 IEEE International Conference. Fifteenth IEEE International Conference on Micro Electro Mechanical Systems (Cat. No.02CH37266)*. Las Vegas, NV, USA: IEEE, 2002, pp. 364–367. [Online]. Available: http://ieeexplore.ieee.org/lpdocs/epic03/wrapper.htm?arnumber=984278 16

[68] A. Broue, J. Dhennin, P.-L. Charvet, P. Pons, N. B. Jemaa, P. Heeb, F. Coccetti, and R. Plana, "Multi-Physical Characterization of Micro-Contact Materials for MEMS Switches," in *2010 Proceedings of the 56th IEEE Holm Conference on Electrical Contacts*. IEEE, oct 2010, pp. 1–10. [Online]. Available: http://ieeexplore.ieee.org/lpdocs/epic03/wrapper.htm?arnumber=5619519 16

[69] J. Zhan, J. Zhao, S. Xu, and P. Zhu, "Study of the contact force in free-form-surfaces compliant EDM polishing by robot," *Journal of Materials Processing Technology*, vol. 129, no. 1-3, pp. 186–189, oct 2002. [Online]. Available: http://linkinghub.elsevier.com/retrieve/pii/S0924013602006404 16

[70] S. Bograd, P. Reuss, A. Schmidt, L. Gaul, and M. Mayer, "Modeling the dynamics of mechanical joints," *Mechanical Systems and Signal Processing*, vol. 25, no. 8, pp. 2801–2826, nov 2011. [Online]. Available: http://linkinghub.elsevier.com/retrieve/pii/S0888327011000203 16

[71] F. Pennec, "Modelisation du contact metal-metal: Application aux microcommutateurs MEMS RF," Ph.D. dissertation, Universite Toulouse III - Paul Sabatier, 2009. 19, 22, 23

[72] X. Miao and X. Huang, "A complete contact model of a fractal rough surface," *Wear*, vol. 309, no. 1-2, pp. 146–151, jan 2014. [Online]. Available: http://linkinghub.elsevier.com/retrieve/pii/S0043164813005346 20

[73] R. Timsit, "Electrical contact resistance: properties of stationary interfaces," *IEEE Transactions on Components and Packaging Technologies*, vol. 22, no. 1, pp. 85–98,

mar 1999. [Online]. Available: http://ieeexplore.ieee.org/lpdocs/epic03/wrapper.htm?arnumber=759357 25

[74] H. Kanter, "Slow-Electron Mean Free Paths in Aluminum, Silver, and Gold," *Physical Review B*, vol. 1, no. 2, pp. 522–536, jan 1970. [Online]. Available: http://link.aps.org/doi/10.1103/PhysRevB.1.522 25

[75] A. F. Mayadas, "Intrinsic Resistivity and Electron Mean Free Path in Aluminum Films," *Journal of Applied Physics*, vol. 39, no. 9, p. 4241, 1968. [Online]. Available: http://scitation.aip.org/content/aip/journal/jap/39/9/10.1063/1.1656954 25

[76] N. Agraït, "Quantum properties of atomic-sized conductors," *Physics Reports*, vol. 377, no. 2-3, pp. 81–279, apr 2003. [Online]. Available: http://linkinghub.elsevier.com/retrieve/pii/S0370157302006336 25

[77] G. Wexler, "The size effect and the non-local Boltzmann transport equation in orifice and disk geometry," *Proceedings of the Physical Society*, vol. 89, no. 4, pp. 927–941, dec 1966. [Online]. Available: http://stacks.iop.org/0370-1328/89/i=4/a=316?key=crossref.c1c28f4e2757adee23b07106382eee86 26

[78] B. Nikolić and P. Allen, "Electron transport through a circular constriction," *Physical Review B*, vol. 60, no. 6, pp. 3963–3969, aug 1999. [Online]. Available: http://link.aps.org/doi/10.1103/PhysRevB.60.3963 26

[79] D. Mercier, V. Mandrillon, A. Holtz, F. Volpi, M. Verdier, and Y. Bréchet, "Quantitative Evolution of Electrical Contact Resistance between Aluminum Thin Films," in *2012 IEEE 58th Holm Conference on Electrical Contacts (Holm)*. IEEE, sep 2012, pp. 1–8. [Online]. Available: http://ieeexplore.ieee.org/lpdocs/epic03/wrapper.htm?arnumber=6336550 27, 28

[80] M. Groner, J. Elam, F. Fabreguette, and S. George, "Electrical characterization of thin Al2O3 films grown by atomic layer deposition on silicon and various metal substrates," *Thin Solid Films*, vol. 413, no. 1-2, pp. 186–197, jun 2002. [Online]. Available: http://linkinghub.elsevier.com/retrieve/pii/S0040609002004388 28

[81] H. Spahr, S. Montzka, J. Reinker, F. Hirschberg, W. Kowalsky, and H.-H. Johannes, "Conduction mechanisms in thin atomic layer deposited Al2O3 layers," *Journal of Applied Physics*, vol. 114, no. 18, p. 183714, 2013. [Online]. Available: http://scitation.aip.org/content/aip/journal/jap/114/18/10.1063/1.4829910 29

[82] F.-C. Chiu, "A Review on Conduction Mechanisms in Dielectric Films," *Advances in Materials Science and Engineering*, vol. 2014, pp. 1–18, 2014. [Online]. Available: http://www.hindawi.com/journals/amse/2014/578168/ 29

[83] K. Gloos, P. J. Koppinen, and J. P. Pekola, "Properties of native ultrathin aluminium oxide tunnel barriers," *Journal of Physics: Condensed Matter*, vol. 15, no. 10, pp. 1733–1746, mar 2003. [Online]. Available: http://stacks.iop.org/0953-8984/15/i=10/a=320?key=crossref.eb401cbe9fc0143dbd908b2373b5d8b9

[84] S. Sze and K. K. Ng, *Physics of Semiconductor Devices*. Hoboken, NJ, USA: John Wiley & Sons, Inc., oct 2006. [Online]. Available: http://doi.wiley.com/10.1002/0470068329 29, 31, 34

[85] K. Chen, A. Ayon, X. Zhang, and S. Spearing, "Effect of process parameters on the surface morphology and mechanical performance of silicon structures after deep reactive ion etching (DRIE)," *Journal of Microelectromechanical Systems*, vol. 11, no. 3, pp. 264–275, jun 2002. [Online]. Available: http://ieeexplore.ieee.org/lpdocs/epic03/wrapper.htm?arnumber=1007405 35

[86] J. Yue, W. Funsten, and R. Taylor, "Stress Induced Voids in Aluminum Interconnects During IC Processing," in *23rd International Reliability Physics Symposium*. IEEE, mar 1985, pp. 126–137. [Online]. Available: http://ieeexplore.ieee.org/lpdocs/epic03/wrapper.htm?arnumber=4208614 36

[87] F. Yost, D. Amos, and A. Romig, "Stress-driven diffusive voiding of aluminum conductor lines," in *27th Annual Proceedings., International Reliability Physics Symposium*. IEEE, 1989, pp. 193–201. [Online]. Available: http://ieeexplore.ieee.org/lpdocs/epic03/wrapper.htm?arnumber=36344 36

[88] S. Lahiri, "Mechanical stress induced void and hillock formations in thin films," in *Proceedings of IEEE International Workshop on Memory Technology, Design, and Test*. IEEE Comput. Soc. Press, 1994, pp. 22–25. [Online]. Available: http://ieeexplore.ieee.org/lpdocs/epic03/wrapper.htm?arnumber=397202 36

[89] M. A. Haque and M. T. A. Saif, "Deformation mechanisms in free-standing nanoscale thin films: a quantitative in situ transmission electron microscope study." *Proceedings of the National Academy of Sciences of the United States of America*, vol. 101, no. 17, pp. 6335–40, apr 2004. [Online]. Available: http://www.pubmedcentral.nih.gov/articlerender.fcgi?artid=404045{&}tool=pmcentrez{&}rendertype=abstract 36

[90] K. S. Chen, A. A. Ayon, K. A. Lohner, M. A. Kepets, T. K. Melconian, and S. M. Spearing, "Dependence Of Silicon Fracture Strength And Surface Morphology On Deep Reactive Ion Etching Parameters," *MRS Proceedings*, vol. 546, p. 21, jan 1998. [Online]. Available: http://journals.cambridge.org/abstract{_}S1946427400175165 36

[91] R. S. Timsit, "Constriction Resistance of Thin Film Contacts," *IEEE Transactions on Components and Packaging Technologies*, vol. 33, no. 3, pp. 636–642, sep 2010. [Online]. Available: http://ieeexplore.ieee.org/lpdocs/epic03/wrapper.htm?arnumber=5575402 36

[92] I.-S. Yeo, P. S. Ho, and S. G. H. Anderson, "Characteristics of thermal stresses in Al(Cu) fine lines. I. Unpassivated line structures," *Journal of Applied Physics*, vol. 78, no. 2, p. 945, 1995. [Online]. Available: http://scitation.aip.org/content/aip/journal/jap/78/2/10.1063/1.360288 36

[93] H. S. Carslaw and J. C. Jaeger, *Conduction of Heat in Solids*, 2nd ed. Oxford University Press, 1986. 37

[94] C. Poulain, A. Peschot, M. Vincent, and N. Bonifaci, "A Nano-Scale Investigation of Material Transfer Phenomena at Make in a MEMS Switch," in *2011 IEEE 57th Holm Conference on Electrical Contacts (Holm)*. IEEE, sep 2011, pp. 1–7. [Online]. Available: http://ieeexplore.ieee.org/lpdocs/epic03/wrapper.htm?arnumber=6034801 37, 38, 39, 40

[95] Z. Hou, Z. Liu, and Z. Li, "Al/Au composite membrane bridge DC-contact series RF MEMS switch," in *2008 9th International Conference on Solid-State and Integrated-Circuit Technology*. IEEE, oct 2008, pp. 2488–2491. [Online]. Available: http://ieeexplore.ieee.org/lpdocs/epic03/wrapper.htm?arnumber=4735076 38

[96] D. Dickrell and M. Dugger, "Silicone Oil Contamination and Electrical Contact Resistance Degradation of Low-Force Gold Contacts," *Journal of Microelectromechanical Systems*, vol. 16, no. 1, pp. 24–28, feb 2007. [Online]. Available: http://ieeexplore.ieee.org/lpdocs/epic03/wrapper.htm?arnumber=4099364 38

[97] Q. Ma, Q. Tran, T.-K. A. Chou, J. Heck, H. Bar, R. Kant, and V. Rao, "Metal contact reliability of RF MEMS switches," in *SPIE proceedings series*, A. L. Hartzell and R. Ramesham, Eds., jan 2007, pp. 646 305–646 305–13. [Online]. Available: http://proceedings.spiedigitallibrary.org/proceeding.aspx?articleid=1335231 38

[98] K. L. Johnson, "Contact mechanics and the wear of metals," *Wear*, vol. 190, no. 2, pp. 162–170, dec 1995. [Online]. Available: http://linkinghub.elsevier.com/retrieve/pii/0043164895066659 38

[99] A. Carré and J. Schultz, "Polymer-Aluminium Adhesion. I. The Surface Energy of Aluminium in Relation to its Surface Treatment," *The Journal of Adhesion*, vol. 15, no. 2, pp. 151–161, feb 1983. [Online]. Available: http://www.tandfonline.com/doi/full/10.1080/00218468308073223 38

[100] N. Tas, T. Sonnenberg, H. Jansen, R. Legtenberg, and M. Elwenspoek, "Stiction in surface micromachining," *Journal of Micromechanics and Microengineering*, vol. 6, no. 4, pp. 385–397, dec 1996. [Online]. Available: http://stacks.iop.org/0960-1317/6/i=4/a=005?key=crossref.de5910d9d76002d89ba6fb6639b4396b 40

[101] B. D. Jensen, K. Huang, L. L.-W. Chow, and K. Kurabayashi, "Adhesion effects on contact opening dynamics in micromachined switches," *Journal of Applied Physics*, vol. 97, no. 10, p. 103535, 2005. [Online]. Available: http://scitation.aip.org/content/aip/journal/jap/97/10/10.1063/1.1901837 40

[102] L. Chen, N. E. McGruer, G. G. Adams, and Y. Du, "Separation modes in microcontacts identified by the rate dependence of the pull-off force," *Applied Physics Letters*, vol. 93, no. 5, p. 053503, 2008. [Online]. Available: http://scitation.aip.org/content/aip/journal/apl/93/5/10.1063/1.2967855 40

[103] A. Tonck, F. Houzé, L. Boyer, J. L. Loubet, and J. M. Georges, "Electrical and mechanical contact between rough gold surfaces in air," *Journal of Physics: Condensed Matter*, vol. 3, no. 27, pp. 5195–5201, jul 1991. [Online]. Available: http://stacks.iop.org/0953-8984/3/i=27/a=013?key=crossref.d947e9cc962587385512017bffa38f49 41

[104] R. Legtenberg, "Electrostatic actuators fabricated by surface micromachining techniques," Ph.D. dissertation, University of Twente, 1996. 41

Chapter 2

Managing the stress state in structures

Contents

Remember that the operating cycle of the device is composed by the steps of: fabrication; release; actuation and optimization. In this chapter the mechanical stress state existing in structures, before and after release is studied. In order to quantify and understand the stress present in the structures, from their fabrication to released devices, FEM study and physical characterisation are performed.

The stacks of material are those used in microelectronics industry (B) – *e.g.* the metallic layer containing the structures is composed principally by *Al/TiN*.

The fabrication process introduces residual stress in the metallic layer. This stress evolves with steps process: deposition of a metallic layer, annealing and film patterning. This evolution is studied in the first part of this chapter.

Once the structures have been manufactured, the release of freestanding parts is performed. The partial relaxation of residual stress generates a rotation in the structure. The angle of this rotation is then measured on Scanning Electron Microscopy (SEM) images. In order to reproduce this rotation in a virtual laboratory, a FEM model is created. First a linear elastic simulation of the rotation at release is performed.

2.1 Studied structure: Cross-shaped CMOS MEMS

2.1.1 Description of rotational structure

The design of this cross-shape CMOS-MEMS is based on the work of Horsfall [1] on aluminium and Kasbari [2] on copper structures. The structure, integrated in a single layer, is composed of two metallic expansion arms connected to a metal central pointer, thus forming a conducting asymmetrical cross Figure 2.1.

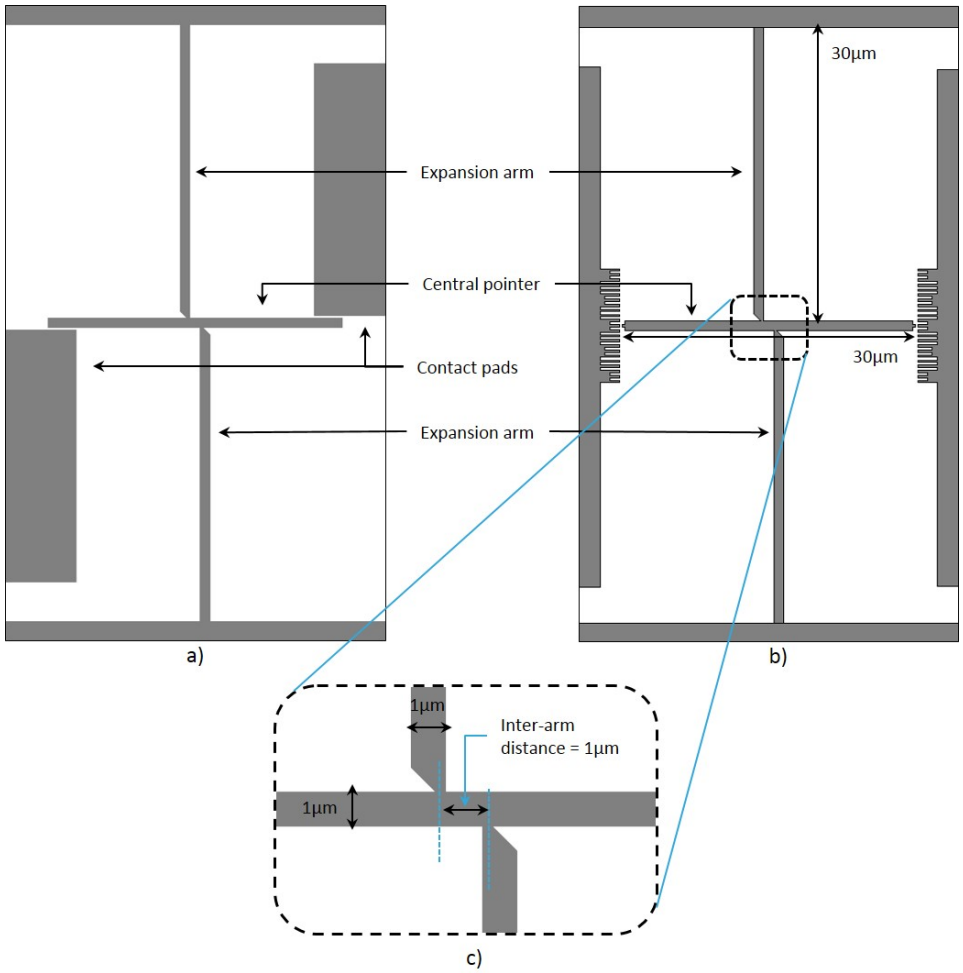

Fig. 2.1 Schematics and main dimensions of the cross-shape structure before release. a) Functional structure with contact pads, b) test structure, c) zoom on the hinge

Two structures, geometrically the same, are schematized in Figure 2.1 – the functional and the test structures. The first one has contact pads to ensure an electromechanical contact (Figure 2.1a). The second, designed without pads, can move freely. The rotation angle is then measured by a 'ruler' in front of the central pointer. The position of the ruler facilitates

the measurement of deviation from the original position of the central pointer before release. The ruler is composed of 23 nanobeams 250 nm wide and 1 µm and 2 µm long. Thanks to the 250 nm space between the nanobeams, this ruler allows quick measurement by steps of 500 nm – *i.e.* the distance between the center of two nanobeams.

The cross-shape device is fixed by SiO_2 dielectric layer (Figure 2.2a) at the end of fabrication process. As a result of the deposition process, and principally by the annealing (400 °C) and cooling steps [3, 4], the arms and pointer have some residual stress.

Before the release stage, which consists in etching away the SiO_2 layer (using Vapor Hydrofluoric acid (HF)(C)) which completely prevents any movement of the conducting lines, the expansion arms are in tension. At release, they shorten asymmetrically, pushing the pointer which rotates clockwise (Figure 2.2b).

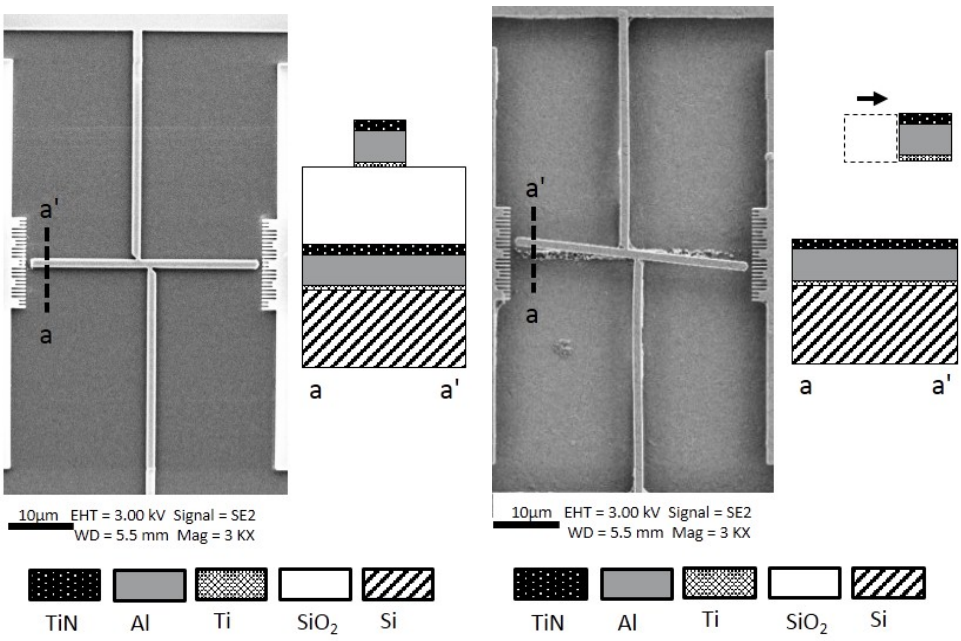

Fig. 2.2 Top and cross section view of the passive stress sensor at a) initial position before release and b) after release when pointer rotates due to stress relaxation

The top view images allow observing and estimating the rotation using the ruler. Next section examines what causes residual stress. In order to do so, it analyses the fabrication steps from the full wafer film to design of the structure patterns.

2.1.2 From thin film to line stress state

As explained in fabrication process description (B), a thin *Al* film is patterned to shape our structures. The structure design, basically composed of lines, imposes different levels of stress compared with an infinite *2D* film. Thus the metallic biaxial stress measured on unpatterned wafers evolves to a longitudinal uniaxial stress in fabricated structures – *i.e.* from full wafer to lines.

The stress in thin films can be measured by optical interferometry [5], X-ray diffraction (to measure lattice spacing [6] or to measure substrate curvature [7]), and laser scanning [3]. The simplest method is to measure the substrate curvature and use Stoney's approximation [8, 9]. This approximation gives the apparent stress in *M3* metallic layer. The technological stack is shown in cross section in Figure 2.3.

The film consists of:

- 0.52 µm of patterned standard CMOS metallic layer (*M3*) – *Ti* 7.5 nm / *Al* 470 nm / *TiN* 45 nm.

Then the substrate consists of:

- a 1.6 µm of sacrificial SiO_2 layer (*IMD1*), over
- a 0.52 µm metallic layer (*M1*), used to stop the release, over
- a 750 µm of *Si* (100) wafer.

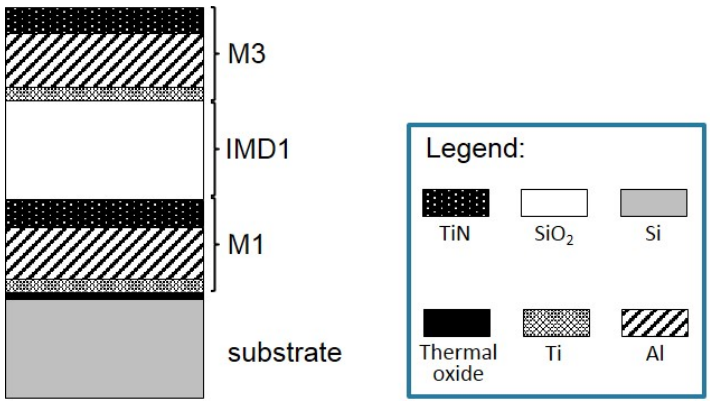

Fig. 2.3 Technological stack used to fabricate the devices

In this standard fabrication process, the *M3* metallic layer (522.5 nm) represents only 0.06 % of the silicon wafer thickness (750 µm). This configuration allows the stress determination according to the film/substrate model proposed by Stoney [8]. A test is then performed to confirm the ∼300 MPa stress value found in literature [4, 10].

The thermal cycles during the fabrication process of the device generate a thermo-elastic deformation, which is accumulated. Then, the effect of the temperature can produce a microstructure modification and/or a stress exceeding the elastic limit of the film, which finally determine the stress state of the film. The stress is thus built by the difference of expansion coefficients between each film and the substrate – *e.g.* $23 \times 10^{-6}\,\mathrm{K}^{-1}$ for aluminium and $3 \times 10^{-6}\,\mathrm{K}^{-1}$ for *Si* [4]. If the expansion coefficients are isotropic, a biaxial stress is generated. After layer deposition, during step-cooling, the *Al* layer shrinks more than *Si* which produces a tensile stress state on the *Al*.

2.1.3 Full Wafer stress approximation: Stoney's formula

In the case of a tensile stress (+), the face of substrate bonded to the film becomes concave. On the contrary, for a compressive stress (–), the *film/substrate* interface becomes convex.

The relationship between radius of curvature $R_{wf} = \frac{1}{k_{wf}}$ and film main average stress is:

$$\overline{\sigma_f} = k_{wf} \cdot \frac{E_s \cdot t_s^2}{6 \cdot (1 - \nu_s) \cdot t_f} \tag{2.1}$$

E_s being the Young's modulus of the substrate *Si*; t_s the substrate thickness; ν_s the Poisson's ratio of the substrate; and t_f the thickness of the film (*Al*).

The Stoney formula has the key property that the relationship between curvature k and thin film force f does not depend on properties of the film, only the Young's modulus and Poisson's coefficient of the substrate are involved.

An experiment on full wafers has been carried out to study the effect of different layer thicknesses of *M3* on measured stress (the initial courbure is considered as initial state). The capacitive measurement is used to determine the 8 inch wafer shape. During the measurement, the wafer is positioned horizontally onto three pins separated by 120°, they measure the distance between the wafer and each sensor. Additionally, this study gives the individual stress on *Al* and *TiN* sublayer. The Design of Experiment (DOE) involves 6 wafers described in Table 2.1.

Using Stoney's formula with equi-biaxial stress assumption, an apparent tensile stress can be found in *M3* metallic layer. I consider this *M*3 layer composed by: a Ti/Al layer, which will be as a single layer, noted Al, and a TiN layer. Results of this measurement are shown in Figure 2.4.

Wafers #04 and #05 have only an *Al* layer (470 nm of thickness). This allows obtaining a bilayer stress directly by Stoney's approximation. Therefore, the tensile stress of +290 MPa consists in the homogeneous biaxial residual stress on a single *Al* layer, which is confirmed by the literature [3, 4, 10].

			M3		
Wf *ID*	*M1*	*IMD1*	*Ti* nm	*Al* nm	*TiN* nm
1	0.52 µm Std	1.6 µm SiO_2	7.5	470	45
2			7.5	470	45
3			7.5	470	20
4			7.5	470	0
5			7.5	470	0
6			7.5	880	20

Table 2.1 The 6 full wafers used to measure the bow, in a variation of *M3* deposition

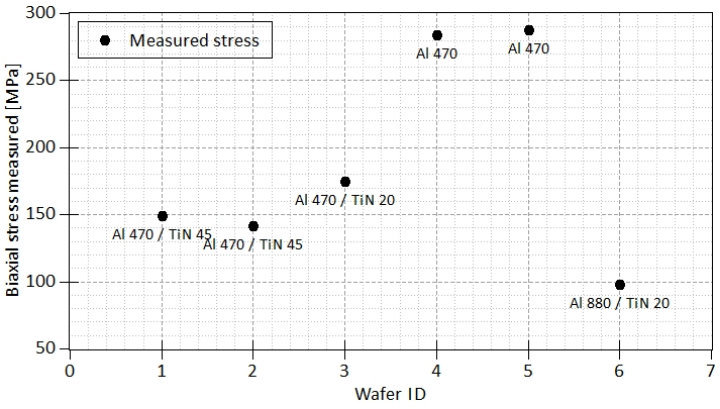

Fig. 2.4 Full wafer apparent stress measured in a thin metal layer. The 6 wafers have 4 different metal configurations

A tensile stress near 150 MPa is obtained on the standard bimetallic layer (wafers #01 and #02) – *i.e.* composed by 470 nm of *Al* and 45 nm of *TiN*. This difference is explained by Young's modulus of *TiN*, seven times stiffer (500 GPa) than *Al* (70 GPa) – *TiN* has a compressive stress [11, 12].

The thin layer of *TiN* (20 nm) over *Al* (470 nm), #03, gives a tensile stress level slightly higher (15 %) than standard *Al*/*TiN* bilayer (#01 and #02). Thereby, the tension stress in the *Al* film is more compensated when the *TiN* film in compression is thicker [11]. However, this stress variation is slight when we compare the thickness of the*TiN* layer of the *Al* layer due to *TiN* being much thinner than *Al*– *i.e.* for a *TiN* layer thickness from 10 to 5 percent of *Al* thickness the stress is 15 % higher.

With wafers #06 and #03 that have the same *TiN* thickness, we can study the influence of the *Al* thickness. Conforming to the principle of "thinner = less compensated", the tensile stress decreases by 45 % for a thick *Al* layer – compared with #03 of *M3* layer configuration (*Al* 470 nm / *TiN* 20 nm).

Knowing the average *M3* layer stress, furthermore the stress and thickness of *Al* layer, the *TiN* layer stress can be approximated with the following formula [9]:

$$\sigma_{TiN} = \frac{1}{t_{TiN}} \cdot (\sigma_{M3}(t_{Al} + t_{TiN}) - \sigma_{Al} t_{Al}) \tag{2.2}$$

σ_{M3} being the apparent biaxial stress in *M3*; σ_{Al} the apparent biaxial stress in *Al* (+290 MPa); σ_{TiN} the apparent biaxial stress in *TiN*; and t_x the thickness in *x-layer* (*Al* and *TiN*).

In this way, considering the wafers #04 and #05 and thus the single aluminium layer stress σ_{Al}=+290 MPa, it is possible to obtain the stress in each layer.

M3		Al		TiN [11]	
σ_{M3} MPa	Wafer #	t_{Al} nm	σ_{Al} MPa	t_{TiN} nm	σ_{TiN} MPa
150	1.2	470	290	45	-1300
190	3	470	290	20	-2100
290	4.5	470	290	-	-
100	6	880	150	20	-2100

Table 2.2 Estimation of stress in each sublayer — *TiN* and *Al*. Measured values in bold

Increasing the thickness of *TiN* layer decreases the compressive stress [13] – *i.e.* the stress depends on the thickness, because the structure varies with thickness.

In order to verify our finding, full wafer samples were prepared with a 90 nm *TiN* deposition over *Si* substrate. Bow was measured and Stoney's approximation was made. The compressive stress in *TiN* of −600 MPa was deduced, confirming our results (Table 2.2), therefore:

- −2.1 GPa if *TiN* 20 nm

- -1.3 GPa if *TiN* 45 nm
- -0.6 GPa if *TiN* 90 nm

in accordance with [11, 12].

For the *Al* layer, these experimental data are compared with previous works by Bostrom [14] and Vayrette [15] in Figure 2.5.

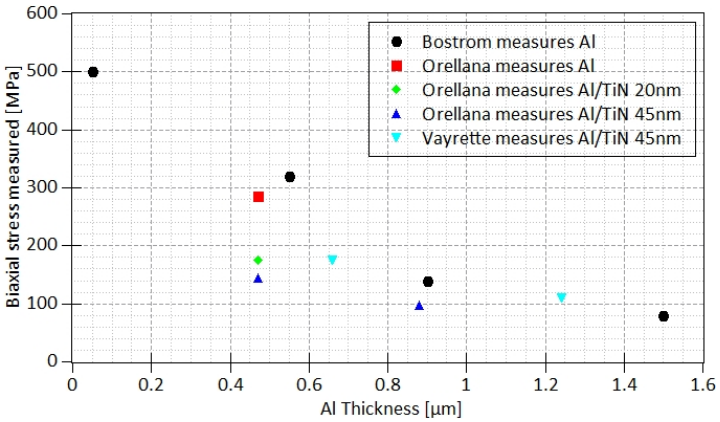

Fig. 2.5 Collected data of full wafer stress measures

The stress values are coherent with data reported in previous works. While Bostrom used a composite metallic layer composed of aluminium sputtered from a target containing $0.5wt\%Cu$ and $1wt\%Si$, Vayrette and the present work use the same aluminium compound (Al $0.5wt\%Cu$).

The next step in the fabrication process is to pattern the film in order to create the devices in a single layer. This process creates a structure in the form of beams with free sides. Some of the stress components are thus relaxed. The next section analyses the resulting stress state in the lines.

2.1.4 Stress state in a line

The stress measured in the previous section requires a biaxial condition, considering x and y component of stress tensor as equal. The structures studied here have a beam "*1D*" shape, specifically the expansion arms and the pointer – 30 µm in length, 1 µm in width and 0.47 µm in height. This form factor makes it necessary to redefine the stress component in order to consider the supplementary free surfaces and the subsequent stress relaxation.

Several theoretical and experimental stress studies in patterned line structures have been performed [16, 17, 6, 18]. Efforts will focus on finding a relationship between biaxial stress ($\overline{\sigma}$) descriptions and realistic residual stress in principal axes on line shapes, where the x-axis

is the width of the arm, and the y-axis is along the arm – *i.e.* transversal σ_{xx}, longitudinal σ_{yy}, and normal σ_{zz} along the arm.

A FEM study in unpassivated *Al* lines shows that the stress along the longitudinal direction is larger than in the transversal direction. This study was performed by Sauter [17] and confirmed experimentally by Flinn and Yeo [16, 18]. Maniguet [6] measured the stress in unpassivated *W* lines. All these studies confirm that the stress state is unequally biaxial and that stresses decrease as line width decreases. Maniguet ([6] found for his tungsten lines a relationship for longitudinal stress component σ_{yy} , which can be applied in aluminium lines because the relationship uses only material properties.

$$\sigma_{yy} = \overline{\sigma} \cdot (1 - \nu_f) \tag{2.3}$$

where $\overline{\sigma}$ is the biaxial stress component and ν_f Poisson's coefficient of film.

The Maniguet experiment was performed by X-ray measurements on striped lines over substrate. A planar stress state is assumed (normal component of stress (σ_{zz}) is assumed to be zero). Two line widths (w) of 1.7 µm and 4 µm have been studied, with the same homogenous height (h) of 0.65 µm. These lines are created from a uniform film which is then patterned, over 500 µm of *Si* substrate.

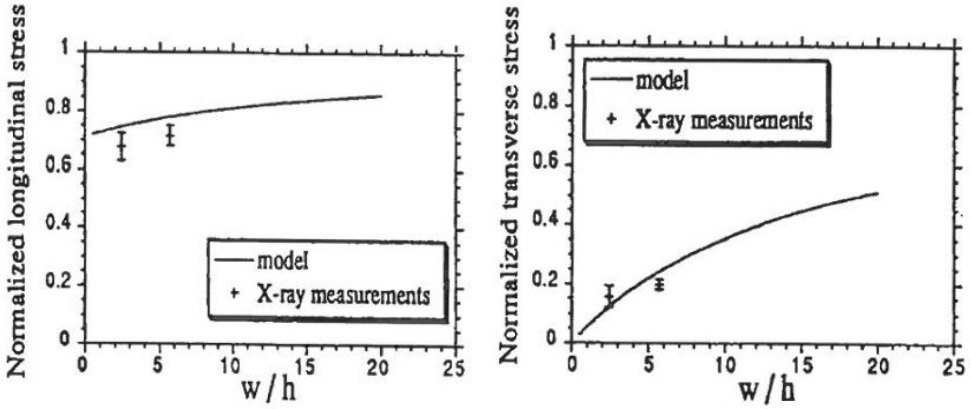

(a) (b)

Fig. 2.6 Variation of normalized stress with aspect ratio in a *W* line for a) longitudinal and b) transversal direction [6]

All the dimensions are normalized by line height. Both stress component (longitudinal and transverse) are normalized by the uniform biaxial film stress.

The aspect ratio used in our structures ($\frac{w}{h} = 2$) can be compared with the graph of Figure 2.6b – for transversal stress. The values of biaxial stress measured in previous section (+290 MPa) is transformed in longitudinal stress component by Equation 2.3.

- Longitudinal stress component σ_{yy}=+190 MPa
- Transversal stress component (from Figure 2.6b: $\sigma_{xx} = \overline{\sigma} \cdot 0.08$) σ_{xx}=+20 MPa

As in [6], the transversal stress is considered in the following to be equal to zero to simplify the future FEM analysis.

The other bilayer component, the *TiN* layer, has a compressive stress state of $\overline{\sigma} = -1.3$ GPa for 45 nm of *TiN* full wafer. The Equation 2.3 is used to extract the longitudinal stress along a line:

- Longitudinal stress component $\sigma_{yy} = -750$ MPa
- Transversal stress component (from Figure 2.6b: $\sigma_{xx} = \overline{\sigma} \cdot 0.08$) σ_{xx}=−100 MPa

The transversal stress, representing 10 % of longitudinal stress, is considered in the following to be equal to zero to simplify the future FEM analysis.

2.2 Functional devices and residual stress study

2.2.1 Bending and rotation in freestanding parts

Using a standard technological stack – including *TiN*, *Al* and *Ti* as metallic layer – bending is observed by tilted SEM images (Figure 2.7) – the end of pointer is close to *M1* layer 1.6 µm under *M3* patterned layer.

The bending observed in freestanding structures is an obstacle on the way to the expected operational mode – *i.e.* movement in-the plane of mobile structure, without contact with metal layer *M1*.

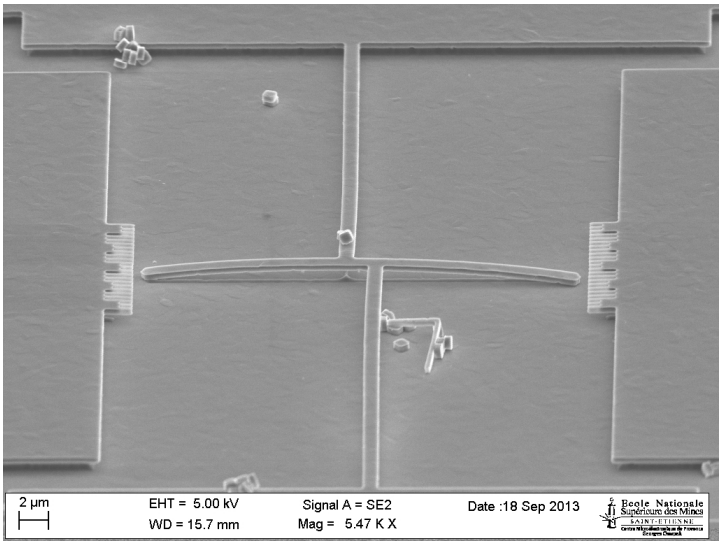

Fig. 2.7 Tilted SEM view of structure, with the pointer bent

This section aims at understanding, modelling and reducing this warp defect. In order to understand and quantify the bending in a composite layer, Timoshenko's analysis is recalled next.

2.2.1.1 Stress study in multilayer case

The beam deflection is a function of its thickness and the residual stress. It is derived from Timoshenko's analysis [19] of a thermal bimetallic cantilever. The next development considers Liu [20] and Vilms [21] studies, which analyse bending in a three-layer metallic composite.

The thin 7.5 nm *Ti* film (below *Al*), representing 1.6 % of *Al* thickness, is not considered in the following calculations. Thus a bilayer case is considered for the study.

The model considers no external forces imposed to the cantilever, assume two concentrated forces applied at the centre of their respective layer and the moment taken from the bottom of the *Al* layer. Forces (F_i) and moments (M_i) of the cantilever must be zero at equilibrium:

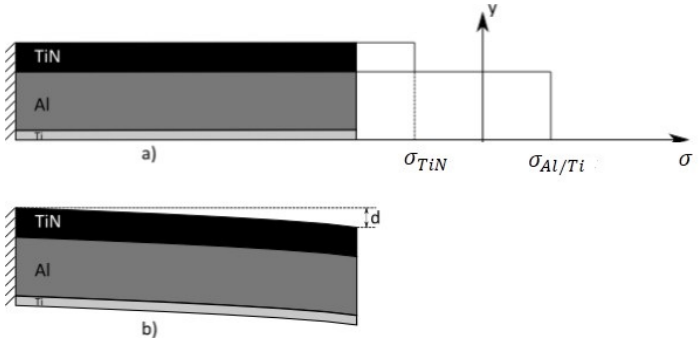

Fig. 2.8 Bending representation in a three-layer that became a bilayer for the analysis

$$F_{Al} + F_{TiN} = 0 \tag{2.4}$$

$$M_{Al} + M_{TiN} = -\left(F_{Al} \cdot \frac{t_{Al}}{2} + F_{TiN} \cdot \left(t_{Al} + \frac{t_{TiN}}{2}\right)\right) \tag{2.5}$$

From beam theory and Fertis' study [22]

$$M = -\frac{1}{\rho} \cdot (E_{Al} I_{Al} + E_{TiN} I_{TiN}) \tag{2.6}$$

where ρ is the radius of curvature of the cantilever beam, which is a function of its length L and tip deflection d:

$$d = \rho \left[1 - \cos\left(\frac{L}{\rho}\right)\right] \tag{2.7}$$

Taylor series expansion of $\cos(\theta)$ leads to,

$$\rho \approx \frac{L^2}{2 \cdot d} \tag{2.8}$$

For a cantilever beam having a rectangular cross section, the moment of inertia is given by:

$$I_i = \frac{w \cdot t_i^3}{12},\ i = Al, TiN \tag{2.9}$$

where w is the width of cantilever.

Equation 2.5 and Equation 2.6 express the beam equilibrium in terms of axial forces and radius of curvature:

$$\frac{1}{\rho}\cdot\sum_{i=Al,TiN}E_i\cdot I_i=-\left(F_{Al}\cdot\frac{t_{Al}}{2}+F_{TiN}\left(t_{Al}+\frac{t_{TiN}}{2}\right)\right) \tag{2.10}$$

For the bilayer, the total strain at the interface of paired layers must be equal. The total strain is due to a change in temperature, to the residual stress, the axial force and the bending deformation,

$$\varepsilon_{total}=\varepsilon_{temp}+\varepsilon_{stress}+\varepsilon_{shear}+\varepsilon_{bend} \tag{2.11}$$

Release is performed at room temperature, hence $\varepsilon_{temp}=0$

$$\frac{\sigma_{Al}}{E_{Al}}+\frac{F_{Al}}{E_{Al}W_{Al}t_{Al}}+\frac{t_{Al}}{2\rho}=\frac{\sigma_{TiN}}{E_{TiN}}+\frac{F_{TiN}}{E_{TiN}W_{TiN}t_{TiN}}+\frac{t_{TiN}}{2\rho} \tag{2.12}$$

Combining Equation 2.4, Equation 2.10 and Equation 2.12, the tip deflection of bilayer can be written as:

$$d=\frac{3L^2\left(E_{Al}t_{Al}\sigma_{TiN}t_{TiN}^2+E_{Al}t_{Al}^2\sigma_{TiN}t_{TiN}-\sigma_{Al}t_{Al}^2E_{TiN}t_{TiN}-\sigma_{Al}t_{Al}E_{TiN}t_{TiN}^2\right)}{E_{Al}^2t_{Al}^4+E_{TiN}^2t_{TiN}^4+4E_{Al}t_{Al}^3E_{TiN}t_{TiN}+6E_{Al}t_{Al}^2E_{TiN}t_{TiN}^2+4E_{Al}t_{Al}E_{TiN}t_{TiN}^3} \tag{2.13}$$

$$d=\frac{3L^2\cdot\left[t_{Al}t_{TiN}\cdot\left(t_{Al}+t_{TiN}\right)\cdot\left[E_{Al}\sigma_{TiN}-\sigma_{Al}E_{TiN}\right]\right]}{E_{Al}^2t_{Al}^4+E_{TiN}^2t_{TiN}^4+E_{Al}t_{Al}E_{TiN}t_{TiN}\cdot\left(4t_{Al}^2+6t_{Al}t_{TiN}+4t_{TiN}^2\right)} \tag{2.14}$$

The tip deflection depends on t_i and σ_i, *i.e.* the thickness and stress of each film layer respectively.

Using the longitudinal stress estimated in previous section[1], and their thickness:

- *TiN*, σ_{xx}=−750 MPa, 45 nm
- *Al*, σ_{xx}=+190 MPa, 470 nm

Solving numerically Equation 2.14, for the beam length L = 30 µm, the tip deflection is:

$$d=4.36\,\mu\text{m}$$

This value has been verified by FEM analysis and a deflection of 4.35 µm is obtained in the tip of cantilever.

Equation 2.14, shows a heterogeneity generated by the *Al* layer and the *TiN* layer. The bilayer, with the tensile and compressive stress for *Al* and *TiN* respectively, generates a bending

[1] x represent the longitudinal direction on the beam

of 4.36 µm. If the *TiN* layer is "removed" ($t_{TiN} \to 0$), Equation 2.14 shows that the curvature will be zero.

This flexion value is for a cantilever – *i.e.* anchored on one side – the geometry of the device studied is different. This first model points to the bilayer character as a probable cause of the observed bending. It apparently overestimates bending, and a more quantitative comparison with experiment will be performed by FEM analysis in subsection 2.2.2.1.

This calculation explains and justifies the choice of removing the *TiN* layer from a standard fabrication flow. Hereinafter, the *M3* metallic layer is only composed by aluminium with a uniaxial residual stress of +190 MPa. This introduces a change in the process flow, contrary to our initial intention, however this is not detrimental to the project.

2.2.1.2 Verification of the elimination of bending

In order to confirm a successful release, tilted images of structures fabricated without the *TiN* layer have been taken. They confirm that the structures are well suspended (Figure 2.9). This qualitative information has been also validated quantitatively by optical profilometry.

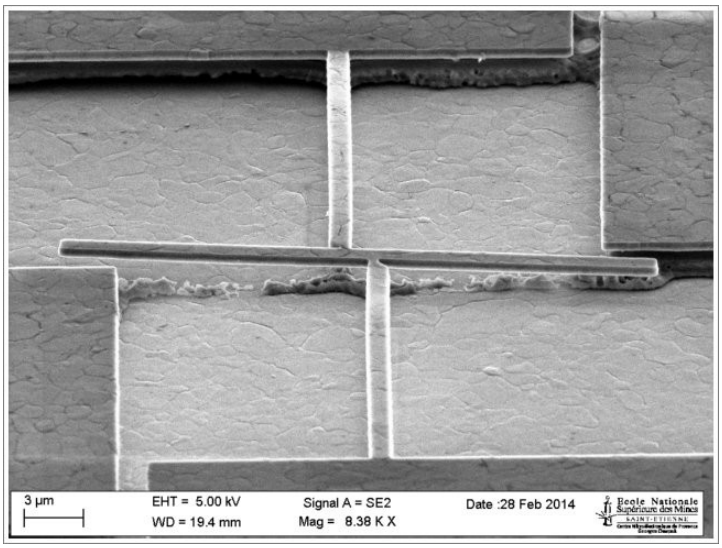

Fig. 2.9 Tilted SEM image of rotated structure without the *TiN* layer

With a simpler setup and measurement than the SEM observation, the optical profilometry gives an accurate quantitative information on release and bending. The vertical resolution is 3 nm in a Vertical Scanning Interferometry (VSI) mode. Figure 2.10 gives a top view scan of the device, confirming rotation and the absence of any significant bending of the pointer.

The cross-section profile (Figure 2.10b), from the upper arm to the lower pad, confirms a successful release step of structure of Figure 2.7 – without bending states. We retrieve the

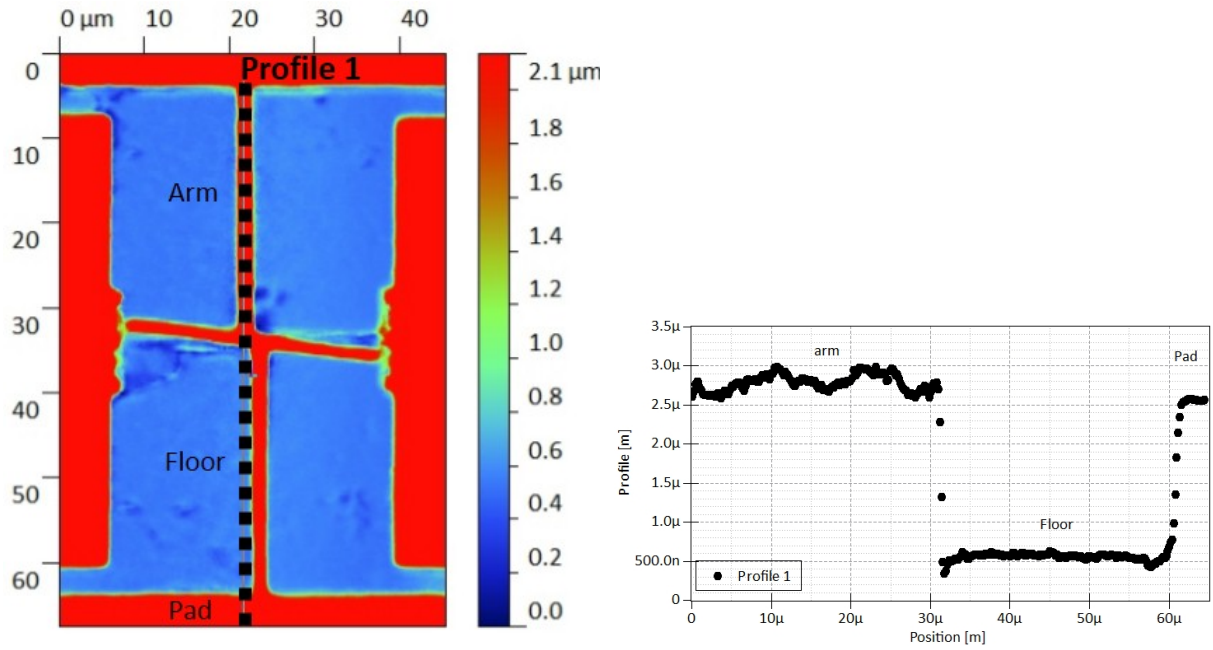

(a) (b)

Fig. 2.10 a) Optical profilometry and b) profile view of structure after release

2.12 µm (1.6 µm of oxide + 0.52µm of *M3* layer) from the top of *M1* layer to the top of *M3* layer – *i.e.* from 0.5 µm on the floor level to (2.6 ± 0.2) µm on the arm level.

The previous calculation, performed in a bilayer with opposite stress state shows a bending in the structure – *i.e.* *Al* in tension and *TiN* in compressive stress state. After removing the *TiN* layer, the optical profilometry shows that the improvement suggested by the model is confirmed by practical implementation.

2.2.2 FEM analysis

In order to create a robust FEM model, the first stage is modelling the mechanical behaviour. Only the arms and the pointer, the functional parts of the structure, are introduced in COMSOL MULTIPHYSICS V.5.0 FEM software (D). The pads are replaced by no-displacement boundary conditions, as they are bulky and fixed on the *M1* layer by the oxide. The "ECAD import" module has been used to define the device geometry (Figure 2.11). The relaxation of residual stress state, responsible for the pointer rotation, is realized at initial step.

In order to confirm the efficiency of the removal of the *TiN* layer, the release model is studied in two cases: first an *Al/TiN* bilayer is considered, then a single aluminium layer is studied.

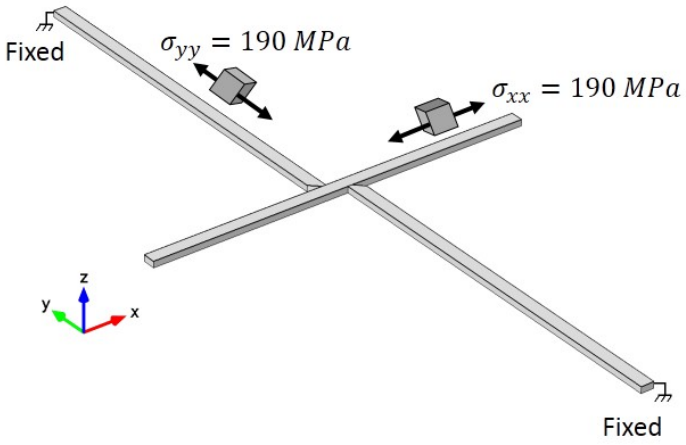

Fig. 2.11 Model of cross-shape structure used in release study by FEM

The *3D steady-state* simulations are performed by the "structural mechanics" option of COMSOL MULTIPHYSICS, using isotropic elastic behaviour.

The formulation used for structural analysis in COMSOL MULTIPHYSICS is a total Lagrangian one, referred to the material initial configuration. This means that the second Piola–Kirchhoff stress tensor S is used together with the Green-Lagrange strain tensor:

$$\varepsilon = \frac{1}{2}[(\nabla \mathbf{u})^T + \nabla \mathbf{u} + (\nabla \mathbf{u})^T \cdot \nabla \mathbf{u}] \tag{2.15}$$

The Duhamel-Hooke's law relates the stress tensor to the strain tensor:

$$S - \mathbf{S_0} = \mathbf{C} : (\varepsilon - \varepsilon_0) \tag{2.16}$$

where $\mathbf{C}$ is the 4^{th} order elasticity tensor, $\mathbf{S_0}$ and ε_0 are the initial stress and strain. For the boundary conditions, zero displacement is imposed at the arm/pad interface ($\mathbf{u} = \mathbf{0}$) – fixed points in Figure 2.11. The other boundaries without any interaction are free to move in any direction.

A linear elastic and isotropic Aluminium material chart was obtained from COMSOL MULTIPHYSICS materials library; Young's modulus is 70 GPa [9], Poisson's coefficient is 0.35 [9]. In the FEM study, the residual stress before release is supposed uniaxial and constant along the longitudinal direction of expansion arms (S_{Ayy}) and the central pointer (S_{Pxx}). Consistently, the estimated stress (+190 MPa) is applied to the device as a longitudinal stress in both arms and pointer (see Figure 2.12). Other assumptions were tested:

- Longitudinal stress in arms (A) and pointer (P) S_{Ayy}=S_{Pxx}=+190 MPa ; S_{Axx}=S_{Pyy}=0 MPa,
- Biaxial stress S_{Axx}=S_{Ayy}=S_{Pxx}=S_{Pyy}=+290 MPa,

- Biaxial stress on the line S_{Axx}=S_{Ayy}=S_{Pxx}=S_{Pyy}=+190 MPa,
- Homogeneous 'y' uniaxial stress S_{Ayy}=S_{Pyy}=+190 MPa, S_{Axx}=S_{Pxx}=0 MPa,
- Homogeneous 'x' uniaxial stress S_{Ayy}=S_{Pyy}=0 MPa, S_{Axx}=S_{Pxx}=+190 MPa,

but uniaxial stress was the choice which fits measurements best – longitudinal stress in arms (A) and pointer (P).

The hinge zone is considered as an extension of the arms, with a longitudinal stress. This simplification may generate an error in rotation estimation, due to the stress concentration due to the narrowing of the hinge at its connection with central pointer. Indeed, the stress relaxation in the arm length prevails – helped by the small contact area with the pointer.

The adaptive mesh option is activated in the FEM software, which first solves on an initial mesh and iteratively inserts elements into regions where the error is estimated to be high, and then re-solves the model. The mesh evolves from 5205 to 47 801 tetrahedral elements (*3D*) after 2 refinement steps Figure 2.12.

2.2.2.1 Study of the bending of the cross

A linear elastic and isotropic titanium nitride material was defined in COMSOL MULTIPHYSICS materials – Young's modulus is 500 GPa, Poisson's coefficient is 0.25 [9]. Consistently, the uniaxial stress (σ_{yy}=−750 MPa, subsection 2.1.4) is applied to the device as a longitudinal stress in both arms and pointer in the *TiN* layer.

The *TiN* layer (45 nm), 10 times thinner than *Al* (470 nm), is meshed in the 'swept mode': it copies the surface mesh pattern of the aluminium layer, creating triangular prism elements.

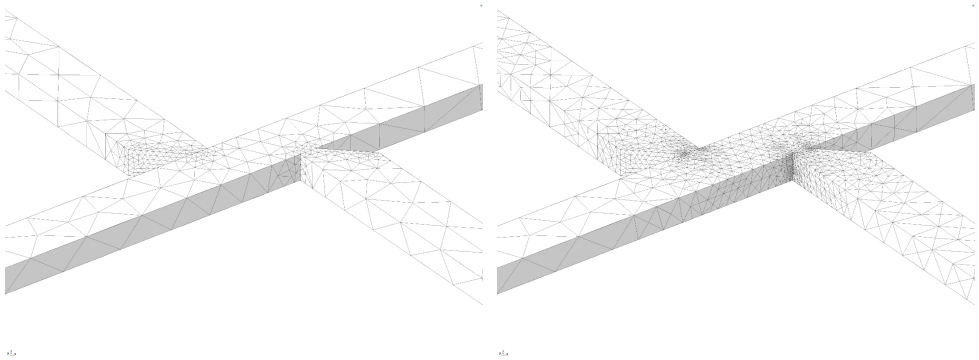

(a) (b)

Fig. 2.12 Adaptive tetrahedral mesh refined in the hinge vicinity: a) 5205, b) 47 801 elements

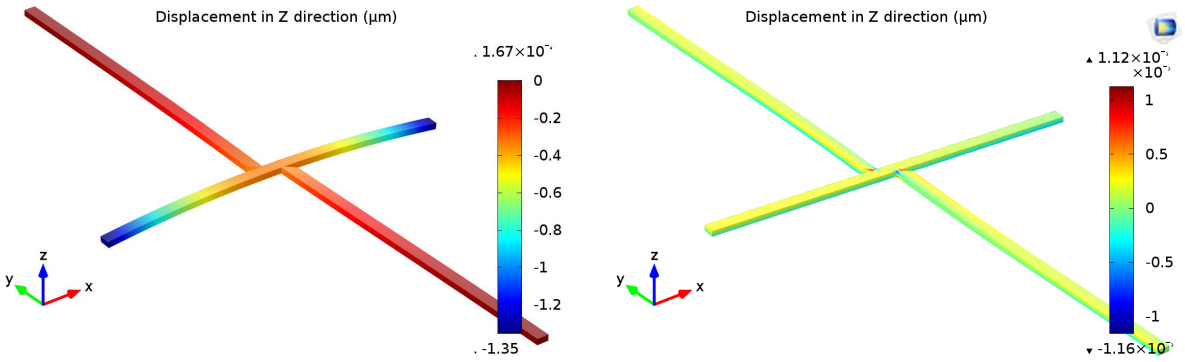

(a) (b)

Fig. 2.13 FEM analysis of stress relaxation at release. a) Bending of 1.35 µm for bilayer *Al/TiN*, b) cancelling bending by elimination of *TiN* layer

The end of pointer bends by 1.35 µm downward (Figure 2.13a) when *TiN* is present. The bow detected by simulation corresponds to SEM images observed in previous subsection 2.2.1 – *i.e.* around 1.6 µm, the *IMD* layer.

Figure 2.13b, shows that the "cross device" remains in the plane, slightly raised from 0.2 µm, and a difference between left and right cross pointer – *i.e.* a small tilting occurs in the plane.

In order to identify the thickness of *TiN* for which the flexion is acceptable, a FEM study is carried out. The thickness of *TiN* evolve from 45 nm to 1 nm and the deflection is simulated. note that 5 or 1 nm of *TiN* is not realistic, it would be oxidized into TiO_2 and the constants should be changed. However the purpose is just to understand quantitatively the origin of bending and to guide towards a solution to this problem.

This measure is carried out for both a cantilever and the cross-shape structure. Figure 2.14 shows the flexion of central pointer in function of the *TiN* thickness. An acceptable deflection less than 0.5 µm is obtained by 1 nm of *TiN*, it means in practice that *TiN* should be elimitated.

For central pointer an acceptable deflection is obtained for a *TiN* thickness representing less than 1 % of *Al* thickness. It is also confirmed that by simple elimination of *TiN* layer, the bending at release step is avoided and the cross-shape structure stays and rotates in the plane (Figure 2.13b).

2.2.2.2 Study of the rotation of the cross

Now that the in-plane movement is obtained without perturbation using only an aluminium layer for the structure, rotation can be studied reliably. The apparent stress (+190 MPa) is

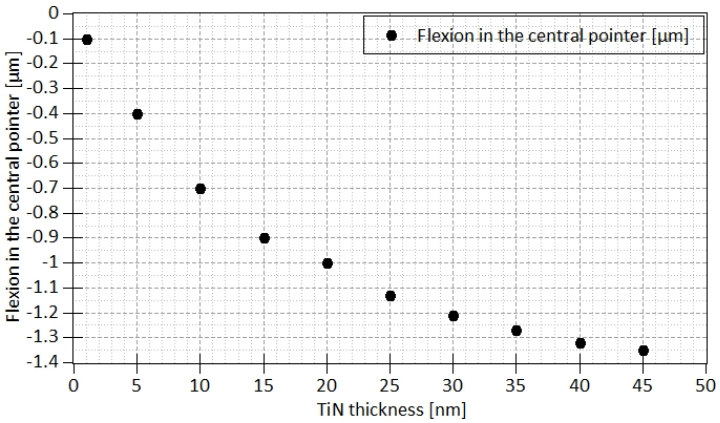

Fig. 2.14 Deflection simulated in a cantilever and in the central pointer of the device

applied to the device as a longitudinal stress in both arms and pointer, which generates a rotation of central pointer at release stage (Figure 2.15).

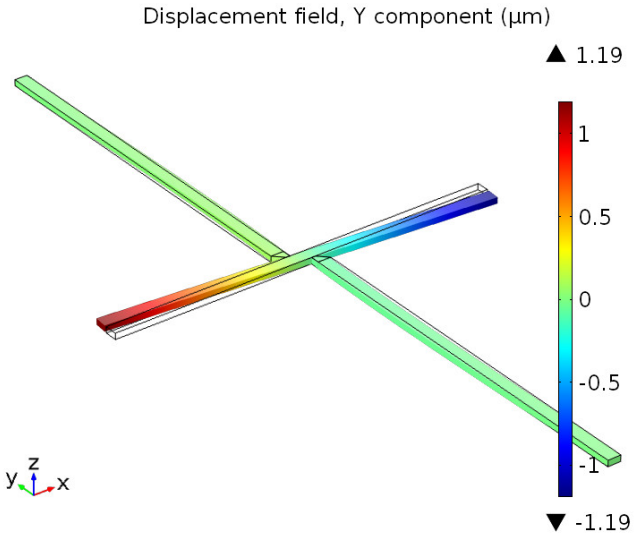

Fig. 2.15 *3D* simulation – illustrating the distance between the final position and the initial position (before release)

Their resulting movement leads to a rotation angle θ=0.08 rad=4.6°. Likewise, it can be easily characterised by the final position-initial position distance (y-displacement of the pointer tip).

$$a = \frac{L}{2} \cdot \theta = 1.2\,\mu\text{m} \tag{2.17}$$

The next sections compares this numerical result with a theoretical model and with measurement on real structures.

2.2.2.3 Analytical model of rotation

The isotropic elastic model proposed by Kasbari [23] describes the mechanical equilibrium of the sensor (Figure 2.16). It assumes that the whole structure remains in its initial plane – which is now true theoretically and in practice.

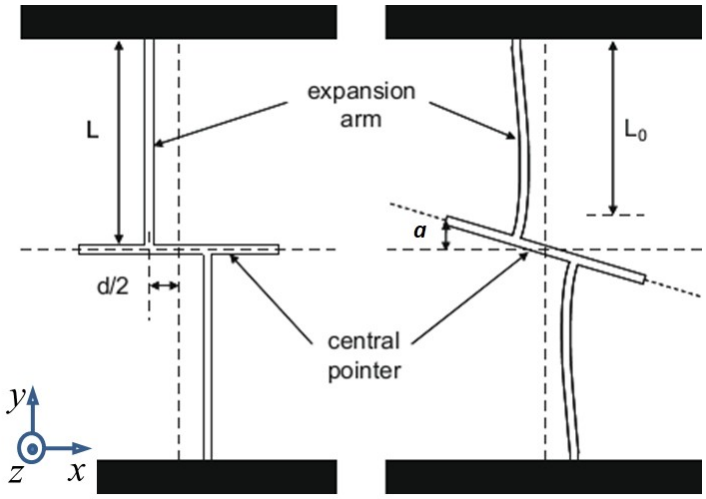

Fig. 2.16 Sensor diagram, central pointer before (left) and after (right) release

The residual stress is considered uniaxial and constant along the longitudinal direction of expansion arms. An analytical model derived from Kasbari [23] is proposed by Vayrette [15]. The model is formulated as the equilibrium between a force due to the arm relaxation and its bending moment in the plane *XOY*. The rotation stops when the reaction moment counterbalances the relaxation force. The model gives the distance a (Figure 2.16) between initial position before release and final position after release.

$$a = \frac{L_p}{L} \cdot \frac{d \cdot L \cdot L_0 \cdot (L - L_0)}{d^2 \cdot (2L - L_0) + \frac{4}{3} \cdot w_a^2 \cdot L_0 \cdot \alpha} \tag{2.18}$$

L is the arm length, before release, L_p is the total pointer length, L_0 is the unstressed length of the arm and α is a coefficient accounting for the shape of the anchoring of the pointer on the arms (Figure 2.17).

$$L_0 = \frac{L}{1 + \frac{\sigma_{yy}}{E}} \tag{2.19}$$

$$\alpha = \frac{w_h}{w_a} \tag{2.20}$$

where σ_{yy} is the average longitudinal residual stress in the arms and E the Young's modulus.

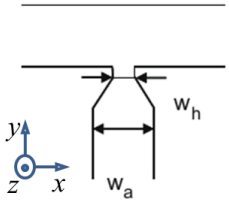

Fig. 2.17 Hinge design used in the Vayrette model

Parameter	w_a	w_h	α	L	E	σ_{yy}	L_0	**a**
Value	1 µm	0.3 µm	0.3	30 µm	70 GPa	+190 MPa	29.92 µm	**1.3μm**

Table 2.3 Values, from Figure 2.1, used to calculate the pointer deviation a

Thus, using the numerical values from Table 2.3 in Equation 2.18 to Equation 2.20 a pointer distance from original position – before release – of $a = (1.3 \pm 0.2)$ µm was found.

This value of a, is in good agreement with the 1.2 µm obtained in FEM analysis.

2.2.3 Rotation measurement after release

After the fabrication process modifications (single *Al* layer instead of *Al/TiN* layer), the functional structure has been measured and characterized after release step. In sample preparation, full wafer is sawn into small parts for easy handling. These parts are released in a HF process. The rotation upon release has been measured by SEM image and compared with the analytical and FEM model predictions.

Released structures are observed in the SEM (Zeiss ultra 55), at a tension of 2 kV to avoid charging electrically the metal surface, in the Secondary Electron (SE) mode to enhance relief.

The rotation of central pointer is measured by the separation between the end of the pointer and the contact pad (Figure 2.18).

The rotation due to stress relaxation in the arms has been found to be identical for all the released samples. The rotation angle is $5.0 \pm 0.8°$. Likewise, it can be characterised by the pointer-pad distance a^*.

$$a^* = a_0 + a = a_0 + \frac{L}{2} \cdot \theta \tag{2.21}$$

where a_0 is the distance from the pointer to the pad before release (0.24 µm) and θ is the rotation angle in rad.

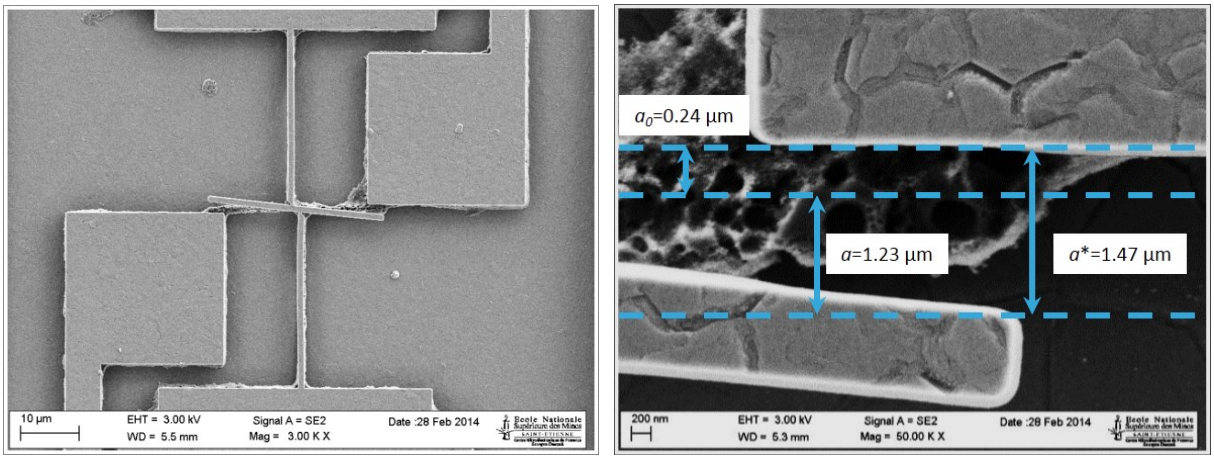

(a) (b)

Fig. 2.18 Measurement of rotation after release

The distance of the pointer from its original position, obtained in the previous FEM analysis in subsection 2.2.2.2 (a=1.19 µm) and analytical subsection 2.2.2.3 (a=1.3 µm) corroborates the Figure 2.18 separation of a=$a^* - a_0$=1.23 µm measured.

Summary

The functional configuration of the structure is ensured by its stress relaxation – the stress originated at the fabrication process. Three main parts have been presented in this chapter.

First, the study of the origin of the stress, which is analysed from the wafer fabrication process. In order to do so, Stoney's formula has been used in various full wafer configurations. This study allows identifying the principal stresses in the main layers – *i.e.* aluminium (Al) and titanium nitride (TiN). Then, the stress has been analysed in the structures, which are principally in the shape of lines. The estimated biaxial stress in a full wafer has thus been redefined as a uniaxial stress using the approximation of Maniguet [6]: $\sigma_{line} = (1-\nu) \cdot \sigma_{wafer}$.

Secondly, the functional device has been studied at its release stage. This stage consists in etching away the SiO_2 layer (using HF) which completely prevents any movement of the device (Figure 2.2a). The expansion arms are in tension, they shorten at release – asymmetrically pushing the pointer which rotates clockwise (Figure 2.2b) positioning at 1.2 µm from its original position. This release generates a rotation movement in the plane, but also an undesirable bending in the freestanding part – *i.e.* the pointer. After a study of the stress level in the composite metallic layer, in which theoretical and numerical models showed that the stress in TiN was the cause of the bending, the TiN layer has been removed and experiments have confirmed that this process change does eliminate bending.

Once the structure correctly released, the last part uses FEM as a virtual laboratory. The structure has been simulated to represent its release (rotation) – *i.e.* a displacement of 1.2 µm for this particular design, sufficient to actuate the switch. Results agree very well with measurement. The numerical model verifies also the correct release – *i.e.* the device stays in its plane.

Résumé français

La configuration initiale de la structure est assurée par la relaxation des contraintes résiduelles qui ont été créées lors du processus de fabrication. Trois grandes parties sont abordées dans ce chapitre.

Premièrement, l'origine de la contrainte est analysée depuis son processus de fabrication jusqu'à la libération de la structure. La formule de Stoney est utilisée pour identifier la contrainte présente dans les couches principales. Pour cela, différentes configurations de dépôts pleine plaque sont étudiées. Ceci permet d'identifier la contrainte dans les couches supérieures de l'empilement, c'est-à-dire l'aluminium (Al) et le nitrure de titane (TiN). L'étape suivante consiste alors à trouver la contrainte dans les structures qui sont constituées principalement par des lignes. Ainsi la contrainte bi-axiale mesurée en pleine plaque (σ_{wafer}) est transformée en contrainte uniaxiale telle qu'elle doit exister dans une ligne (σ_{ligne}), grâce à des relations expérimentalement validées extraites de la littérature, Maniguet [6] : $\sigma_{ligne} = (1-\nu) \cdot \sigma_{wafer}$.

L'étape de fonctionnement de la structure a été étudiée : l'étape de libération. Elle consiste à dissoudre l'oxyde (SiO_2) qui entoure la structure et qui empêche tout mouvement (Figure 2.2a). Les bras d'expansion libèrent leurs contraintes résiduelles (en tension), raccourcissent, puis poussent le pointeur central, ce qui génère une rotation (Figure 2.2b). La libération génère aussi une flexion hors plan indésirable du pointeur central. Après une étude de l'état de contrainte des couches qui composent la structure, dans laquelle des modèles théoriques et numériques ont montré que la flexion est due aux contraintes de compression présentes dans la couche de TiN, la flexion du pointeur a pu être annulée en supprimant du procédé de fabrication le dépôt de la couche de TiN.

Une fois la structure correctement libérée, une simulation par éléments finis, analysée dans la dernière partie de ce chapitre, a été réalisée. Cette simulation permet de faire le lien entre la contrainte résiduelle et la rotation de 1.2 µm obtenue après libération. La bonne corrélation entre ces deux paramètres constitue le premier pas vers la construction d'un laboratoire virtuel. Ce laboratoire virtuel sera amélioré au fil des chapitres pour le convertir en un outil de prédiction fiable.

Bibliography

[1] A. Horsfall, J. dos Santos, S. Soare, N. Wright, A. O'Neill, S. Bull, A. Walton, A. Gundlach, and J. Stevenson, "A novel sensor for the direct measurement of process induced residual stress in interconnects," in *Electrical Performance of Electrical Packaging (IEEE Cat. No. 03TH8710)*. Estoril, Portugal: IEEE, 2003, pp. 115–118. [Online]. Available: http://ieeexplore.ieee.org/lpdocs/epic03/wrapper.htm?arnumber=1256824 63

[2] M. Kasbari, C. Rivero, S. Blayac, F. Cacho, O. Bostrom, and R. Fortunier, "Direct Local Strain Measurement In Damascene Interconnects," *MRS Proceedings*, vol. 990, pp. 0990–B07–06, jan 2007. [Online]. Available: http://journals.cambridge.org/abstract{_}S1946427400034977 63

[3] P. Flynn, D. Gardner, and W. Nix, "Measurement and Interpretation of stress in aluminum-based metallization as a function of thermal history," *IEEE Transactions on Electron Devices*, vol. 34, no. 3, pp. 689–699, mar 1987. [Online]. Available: http://ieeexplore.ieee.org/lpdocs/epic03/wrapper.htm?arnumber=1486692 64, 65, 66

[4] D. Gardner and P. Flinn, "Mechanical stress as a function of temperature in aluminum films," *IEEE Transactions on Electron Devices*, vol. 35, no. 12, pp. 2160–2169, 1988. [Online]. Available: http://ieeexplore.ieee.org/lpdocs/epic03/wrapper.htm?arnumber=8790 64, 65, 66

[5] S. Wang, J. Chen, D. Li, Y. Huang, Z. Li, and W. Zhang, "Evaluating Interface Effect On Stresses In Thin Films By A Local Curvature Metrology With High Accuracy And Resolution," in *2006 1st IEEE International Conference on Nano/Micro Engineered and Molecular Systems*. IEEE, jan 2006, pp. 1513–1516. [Online]. Available: http://ieeexplore.ieee.org/lpdocs/epic03/wrapper.htm?arnumber=4135231 65

[6] L. Maniguet, M. Ignat, M. Dupeux, J. Bacmann, and P. Normandon, "X-ray Determination and Analysis of Residual Stresses in Uniform Films and Patterned

Lines of Tungsten," *MRS Proceedings*, vol. 308, p. 285, jan 1993. [Online]. Available: http://journals.cambridge.org/abstract{_}S1946427400320814 65, 69, 70, 71, 85, 87

[7] A. Bohg, "Measurement of stresses in thin films on single crystalline substrates," *Physica Status Solidi (a)*, vol. 46, no. 2, pp. 445–450, apr 1978. [Online]. Available: http://doi.wiley.com/10.1002/pssa.2210460206 65

[8] G. G. Stoney, "The Tension of Metallic Films Deposited by Electrolysis," *Proceedings of the Royal Society A: Mathematical, Physical and Engineering Sciences*, vol. 82, no. 553, pp. 172–175, may 1909. [Online]. Available: http://rspa.royalsocietypublishing.org/cgi/doi/10.1098/rspa.1909.0021 65

[9] L. B. Freund and S. Suresh, *Thin Film Materials*. Cambridge: Cambridge University Press, 2004. [Online]. Available: http://ebooks.cambridge.org/ref/id/CBO9780511754715 65, 68, 77, 78

[10] W. D. Nix, "Mechanical properties of thin films," *Metallurgical Transactions A*, vol. 20, no. 11, pp. 2217–2245, nov 1989. [Online]. Available: http://link.springer.com/10.1007/BF02666659 65, 66

[11] R. Machunze and G. Janssen, "Stress gradients in titanium nitride thin films," *Surface and Coatings Technology*, vol. 203, no. 5-7, pp. 550–553, dec 2008. [Online]. Available: http://linkinghub.elsevier.com/retrieve/pii/S0257897208003526 68, 69

[12] H. Liu, Q. Xu, X. Zhang, C. Wang, and B. Tang, "Residual stress analysis of TiN film fabricated by plasma immersion ion implantation and deposition process," *Nuclear Instruments and Methods in Physics Research Section B: Beam Interactions with Materials and Atoms*, vol. 297, pp. 1–6, feb 2013. [Online]. Available: http://linkinghub.elsevier.com/retrieve/pii/S0168583X12007598 68, 69

[13] J.-D. Kamminga, T. de Keijser, R. Delhez, and E. Mittemeijer, "A model for stress in thin layers induced by misfitting particles," *Thin Solid Films*, vol. 317, no. 1-2, pp. 169–172, apr 1998. [Online]. Available: http://linkinghub.elsevier.com/retrieve/pii/S0040609097006147 68

[14] O. Bostrom, "Wafer shape control. Study of the reactivity in Ti/Al dual layers and its effect on the stress," Ph.D. dissertation, Aix-Marseille 3, 2001. 69

[15] R. Vayrette, C. Rivero, B. Gros, S. Blayac, and K. Inal, "Residual stress estimation in damascene copper interconnects using embedded sensors," *Microelectronic*

Engineering, vol. 87, no. 3, pp. 412–415, mar 2010. [Online]. Available: http://linkinghub.elsevier.com/retrieve/pii/S0167931709004390 69, 81

[16] P. A. Flinn and C. Chiang, "X-ray diffraction determination of the effect of various passivations on stress in metal films and patterned lines," *Journal of Applied Physics*, vol. 67, no. 6, p. 2927, 1990. [Online]. Available: http://scitation.aip.org/content/aip/journal/jap/67/6/10.1063/1.345411 69, 70

[17] A. Sauter and W. Nix, "Thermal stresses in aluminum lines bounded to substrates," *IEEE Transactions on Components, Hybrids, and Manufacturing Technology*, vol. 15, no. 4, pp. 594–600, 1992. [Online]. Available: http://ieeexplore.ieee.org/lpdocs/epic03/wrapper.htm?arnumber=159891 69, 70

[18] I.-S. Yeo, P. S. Ho, and S. G. H. Anderson, "Characteristics of thermal stresses in Al(Cu) fine lines. I. Unpassivated line structures," *Journal of Applied Physics*, vol. 78, no. 2, p. 945, 1995. [Online]. Available: http://scitation.aip.org/content/aip/journal/jap/78/2/10.1063/1.360288 69, 70

[19] S. Timoshenko, "Analysis of bi-metal thermostats," *Journal of the Optical Society of America*, vol. 11, no. 3, p. 233, sep 1925. [Online]. Available: https://www.osapublishing.org/josa/abstract.cfm?uri=josa-11-3-233 72

[20] R. Liu, B. Jiao, Y. Kong, Z. Li, H. Shang, D. Lu, C. Gao, and D. Chen, "Elimination of initial stress-induced curvature in a micromachined bi-material composite-layered cantilever," *Journal of Micromechanics and Microengineering*, vol. 23, no. 9, p. 095019, sep 2013. [Online]. Available: http://stacks.iop.org/0960-1317/23/i=9/a=095019?key=crossref.69e3985166c29b7df348c40da29a80d1 72

[21] J. Vilms, "Simple stress formula for multilayered thin films on a thick substrate," *Journal of Applied Physics*, vol. 53, no. 3, p. 1536, 1982. [Online]. Available: http://scitation.aip.org/content/aip/journal/jap/53/3/10.1063/1.330653 72

[22] D. G. Fertis, "Advanced Mechanics of Structures," in *Advanced Mechanics of Structures*, 1st ed. CRC Press, 1996, ch. Chapter 2, p. 512. 73

[23] M. Kasbari, "Intégration de capteurs pour le suivi des contraintes mécaniques sur une ligne de production microélectronique," Ph.D. dissertation, Ecole Nationale Supérieure des Mines de Saint-Etienne, 2008. 81

Chapter 3

Actuation

Contents

Now that the rotational device has been correctly released and characterised, by FEM analysis and measurements, this chapter focuses on the actuation step. The function requested from the device is to act as a switch activated by a heat source – *i.e.* an actuating current inducing Joule heating. In order to find the thermal characteristics of the device, this chapter is divided into two parts.

Firstly, in order to relate unambiguously the rotation with the applied temperature, a homogeneous heating is performed. A model of the thermal characteristics of the device during actuation is thus achieved and the FEM model created in the previous chapter is improved to include the thermal properties.

Secondly, in order to achieve the contact by a localized heat source, a Joule heating actuation is performed. This part then begins with a FEM model, used as a virtual laboratory tool. With the results of simulation – *e.g.* the electric current limits to avoid any mechanical deformation – the Joule actuation test is achieved.

The device must be able to commute between the *On* and *Off* states. This is why two devices are analysed in this chapter.

The NORMALLY *Off* structure, studied earlier, moves away from the pad at release step. Thus, in actuation stage, the NORMALLY *Off* structure moves to reach contact with the pad. On the other hand, a NORMALLY *On* structure grants a contact at release step and moves away from pad to lose the contact in actuation step.

The NORMALLY *Off* structure is used in the first part of this chapter to explain the actuation principle. On the contrary, the NORMALLY *On* structure is used in the last part to measure the contact force obtained at release step. To finish, the numerical model is used to estimate the contact force in actuation step – using a NORMALLY *Off* design.

3.1 Thermal actuation (NORMALLY *Off* structures)

The thermal actuation is performed by a hot plate placed below the sample that heats the bottom of sample homogeneously. The top part of the sample is heated by conduction through the different layers of the stack (*Si*, *Al*, and SiO_2).

An advantage of thermal actuation against Joule heating is to perform a measurement without perturbation by electromigration or temperature gradients for instance.

3.1.1 *In situ* heating in the SEM

A hot stage embedded in the SEM [1] allows applying a controlled temperature and observing the rotation at the same time.

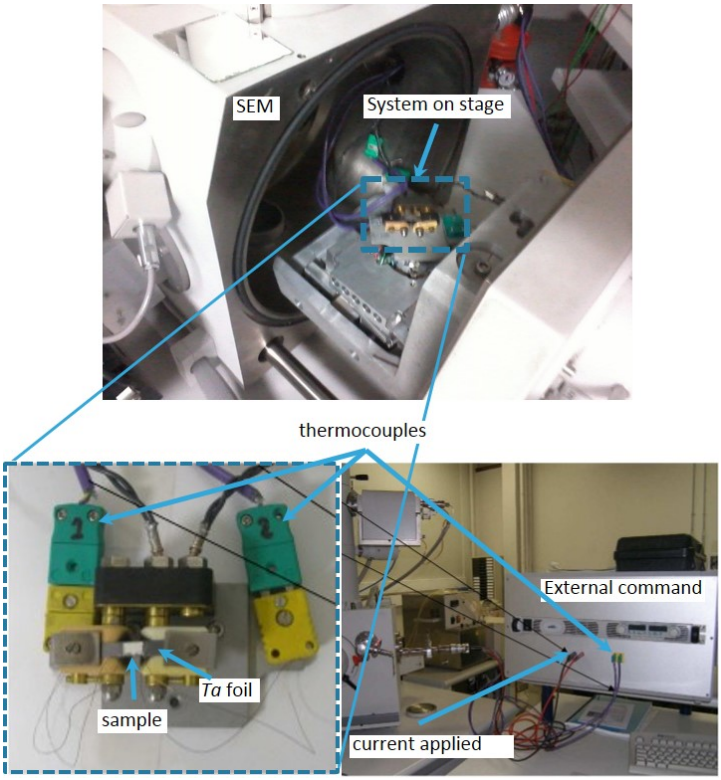

Fig. 3.1 Equipment used in *in-situ* SEM-heating test

3.1.1.1 Experimental description

In practice, a sample is glued on a 50 µm thick Tantalum (*Ta*) foil. The system is attached to a SEM support. Two thermocouples are fixed to the system (Figure 3.1):

- The first one is in the *Ta* foil to measure its temperature and close the loop of auto control of the electric current applied,

- The second one is in the top of the sample to verify its temperature, which should be close to the chosen nominal temperature.

The system (the sample on the stage) is put inside the SEM. Then the *Ta* foil is heated by Joule effect.

The imposed temperature steps are programmed as shown in Figure 3.2. The temperature is increased by steps of 50 °C per minute, then held during 6 min to allow enough time to measure the rotation. Both increase and decrease of temperature are performed.

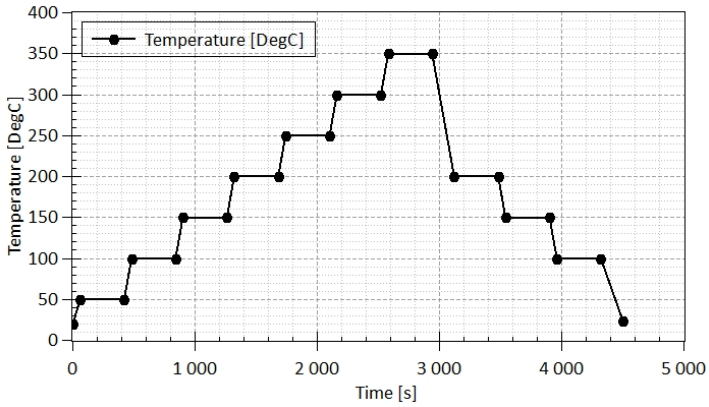

Fig. 3.2 Set point of temperature applied in the bottom of sample

The SEM (*FEI/Philips XL30 ESEM*), used at high tension of 20 kV in the Back-Scattered Electron (BSE) mode, which charges electrically the surface of the sample. To evacuate this charge, a variable pressure environment (0.2 mbar) is used. The SEM images obtained (Figure 3.3) relate the rotation observed to the temperature imposed.

The temperature applied at the bottom of the sample induces a movement in the pointer. For a NORMALLY *Off* device, the anti-clockwise rotation is observed when the temperature increases from room temperature (20 °C) (Figure 3.3a) to 200 °C (Figure 3.3b). This rotation proves the operating principle. The sample is then cooled to room temperature; the pointer is expected to return to the original position.

3.1.1.2 Discussion of results

The pointer-pad distance starts from 1.7 µm at room temperature and reaches contact at 200 °C (Figure 3.4).

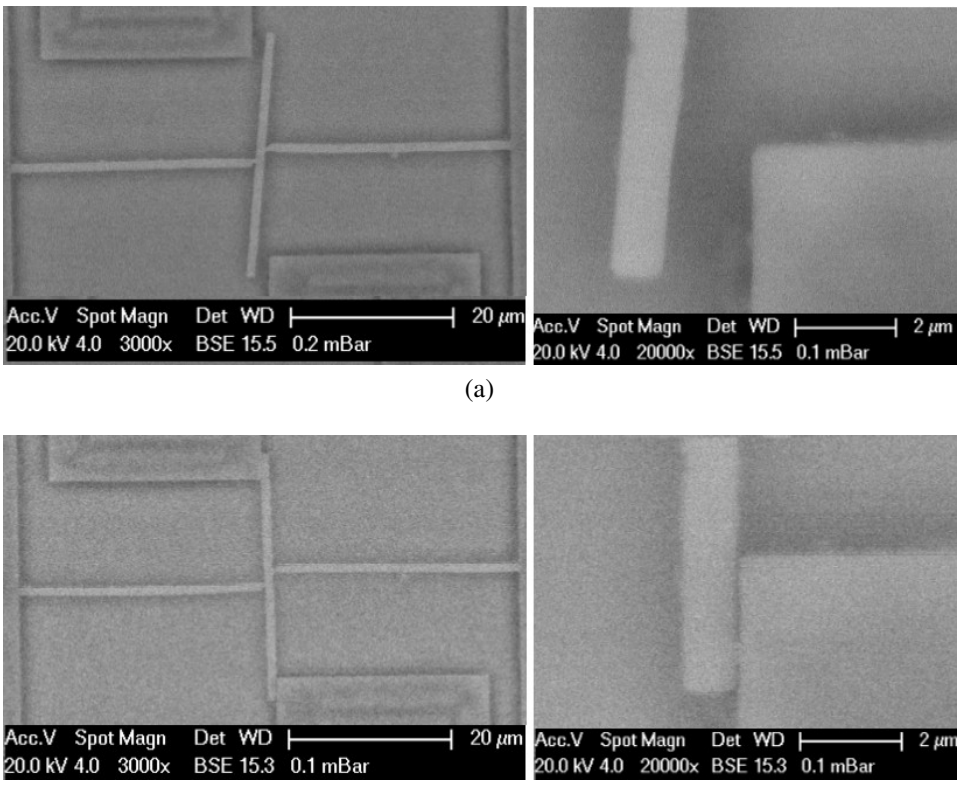

Fig. 3.3 SEM image of *Off* structure a) at room temperature (20 °C), b) at 200 °C, when the pointer reaches the contact pad

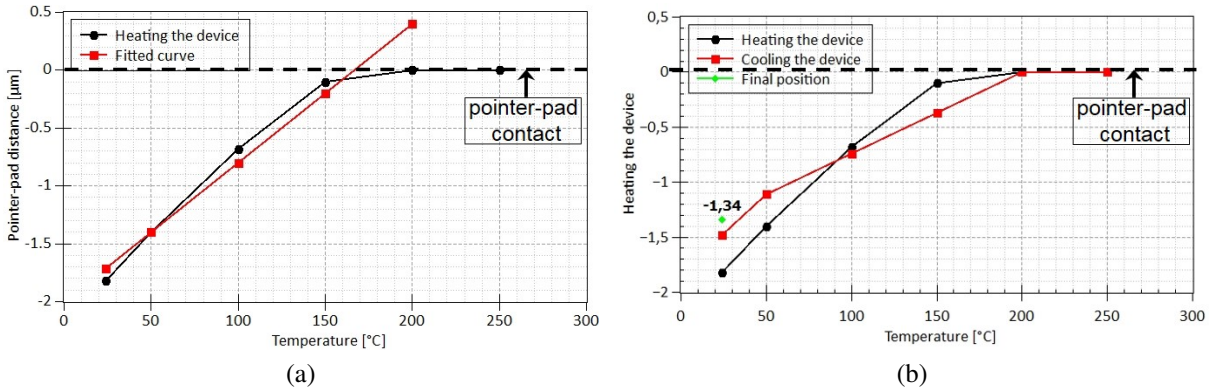

Fig. 3.4 a) pointer-pad distance (a^*) in function to the temperature of *Ta* foil and the fitted curve Equation 3.1, and b) a heating-cooling cycle and the pointer-pad distance after 2 cycles

Except above 150 °C where contact takes place with the pad, a linear relationship between the applied temperature (T) and pointer-pad distance (a^*) is observed.

$$a^* = 0.02 \cdot T - 2 \quad [\mu m] \tag{3.1}$$

After two heating/cooling cycles, the pointer does not return to its original position. A difference of 0.5 ± 0.2 µm is observed at room temperature – in its rest position. The difference between initial and final state could be caused by the plastic deformation. This deformation will be described in next chapter (chapter 4) using FEM analysis.

In the next section, the theoretical model of heat transfer is studied to check that temperature is homogeneous in the experiment. Then the FEM study is carried out and all the results, experimental, theoretical and numerical, are compared.

3.1.2 Theoretical model, first check of the cross temperature

To perform quantitative analyses, we need to verify that the cross temperature, which governs its movement, is approximately equal to the nominal temperature imposed below the device. The estimation of the heat transferred in the system is, in fact, quite complex. There are three distinct modes of heat transfer: conduction, convection and radiation (Figure 3.5).

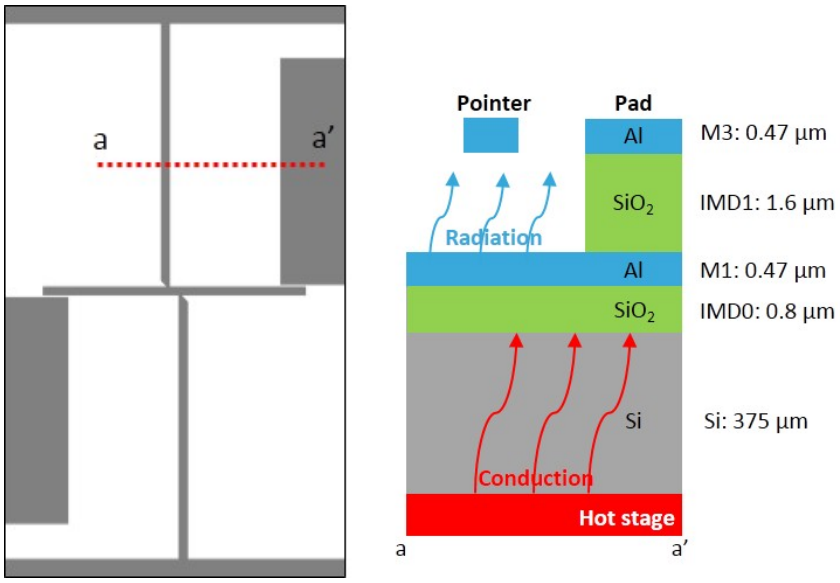

(a) (b)

Fig. 3.5 a) Cross section of cross shape system, and b) schema of heat transfer in hot stage actuation test

The average heat flux $\left(q^* = \frac{Q^*}{A}\left[\frac{W}{m^2}\right]\right)$ is the rate of heat transfer (Q^*) per unit area (A). The heat equation (Fourier's law):

$$q = -k\frac{dT}{dx}[W] \tag{3.2}$$

where $\frac{dT}{dx}$ is the temperature gradient $\left[\frac{K}{m}\right]$ and k is the thermal conductivity $\left[\frac{W}{mK}\right]$.
The total steady heat flux [2] is composed by:

- CONDUCTION, combining the Fourier's law of heat conduction and conservation of energy, in the steady-state case:

$$\rho C_p\frac{\partial T}{\partial t} + \rho C_p\mathbf{u}\cdot\nabla T + \nabla\cdot(-k\nabla T) = q \tag{3.3}$$

if the velocity is set to zero ($\mathbf{u} = \mathbf{0}$), and the analysis is performed at steady state $\left(\frac{\partial T}{\partial t}\right) = 0$, the equation governing pure conductive heat transfer is then:

$$\nabla \cdot (k \nabla T) + q = 0 \tag{3.4}$$

- CONVECTION, the heat conducted away by the fluid/solid interface to the heat transfer, expressed in terms of a convective heat transfer coefficient (h):

$$q^*_{conv} = h \cdot (T_s - T_\infty)[W] \tag{3.5}$$

where $h = \frac{q}{\Delta T}\left[\frac{W}{m^2 K}\right]$, T_s is the temperature on the surface and T_∞ is the surrounding medium temperature.

- RADIATION, the heat radiated between a surface A at T_s and the surrounding air at T_∞ is:

$$q^*_{rad} = \varepsilon \cdot \sigma \cdot (T_s^4 - T_\infty^4)[W] \tag{3.6}$$

where ε is the emissivity of the surface, σ is the Stefan-Boltzmann constant $\left(\sigma = 5.67 \cdot 10^{-8}\left[\frac{W}{m^2 K^4}\right]\right)$

The studied system does not involve heat generation and the analysis is performed at steady heat transfer.

Thus, the thermal resistance $\left(\left[\frac{K \cdot m^2}{W}\right]\right)$ concept can be adopted.

Conduction through a wall of thickness (L):

$$R_{cond} = \frac{L}{k} \tag{3.7}$$

Convection, fluid/solid:

$$R_{conv} = \frac{1}{h} \tag{3.8}$$

Radiation, surface to environment:

$$R_{rad} = \frac{1}{h_{rad}} \quad \text{,where} \quad h_{rad} = \varepsilon \cdot \sigma (T_s^2 + T_\infty^2)(T_s + T_\infty) \tag{3.9}$$

Considering a one direction heat flow through the stack (Figure 3.5), with only the top layer exposed to convection, under steady-state condition on the metallic layer ($M1$):

$$q^* = k_{Si}\left(\frac{T_{Si}-T_{Si/SiO_2}}{L_{Si}}\right) = k_{SiO_2}\left(\frac{T_{SiO_2}-T_{SiO_2/Al}}{L_{SiO_2}}\right) = k_{Al}\left(\frac{T_{Al}-T_{Al/air}}{L_{Al}}\right) = h_{Al}(T_{Al}-T_\infty) \tag{3.10}$$

$$= \frac{T_{Si}-T_{Si/SiO_2}}{R_{cond,1}} = \frac{T_{SiO_2}-T_{SiO_2/Al}}{R_{cond,2}} = \frac{T_{Al}-T_{Al/air}}{R_{cond,3}} = \frac{T_{Al}-T_\infty}{R_{conv}} \tag{3.11}$$

$$= \frac{T_{Si}-T_\infty}{R_{total}} \tag{3.12}$$

where $T_{Si} = 200\,°\text{C} = 473.15\,\text{K}$, $T_\infty = 20\,°\text{C} = 293.15\,\text{K}$ and $R_{total} = R_{cond,1} + R_{cond,2} + R_{cond,3} + R_{conv}$

For a natural convection on a metallic layer, the h value is between 5 to 250 $\text{W m}^{-2}\,\text{K}^{-1}$ [3–5]. In this manner, considering the previous values as limit values in our case, the heat flux should be from:

$$q_T^* = h\cdot(T_s - T_\infty) \approx 5\cdot 180 = 900\left[\frac{W}{m^2}\right] = q_1 \tag{3.13}$$

to

$$q_T^* = h\cdot(T_s - T_\infty) \approx 250\cdot 180 = 45000\left[\frac{W}{m^2}\right] = q_2 \tag{3.14}$$

The simplified model considers only the upside convection model and is valid for the pad only. The freestanding structure and *M3* metallic level have lateral and backside heat transfers that are not considered in the approximation.

From the two previous q_T^* values, the temperature T_2 for the interface *Si/SiO*$_2$ are [1]:

$$T_2 = T_1 - \frac{q_1\cdot dx}{k} = 473.15 - \frac{\mathbf{900}\cdot 375\times 10^{-6}}{130} \approx 473.147K \tag{3.15}$$

$$T_2 = T_1 - \frac{q_2\cdot dx}{k} = 473.15 - \frac{\mathbf{45000}\cdot 375\times 10^{-6}}{130} \approx 473.02K \tag{3.16}$$

where dx is the thickness of the layer, k the thermal conductivity and T_1 the temperature in the bottom (*Si*) of layer. These two values represent the limits according to the literature – *i.e.* 5 to 250 $\text{W m}^{-2}\,\text{K}^{-1}$ [3–5].

All the interface temperatures of the stack presented in Figure 3.5 are calculated and summarized in Table 3.1 for both q_1 and q_2 estimated values.

[1] the temperature applied at the bottom of sample, *i.e.* in *Si* layer, with a thickness of 375 µm=dx, a thermal conductivity k=130 $\text{W m}^{-1}\,\text{K}^{-1}$, and T_1=473.15 K

Material in the stack	Thickness µm	Thermal conductivity $W\,m^{-1}\,K^{-1}$[6]	q	Temp. in the bottom (T_1K), for q_1 and q_2	Temp. in the top (T_2K), for q_1 and q_2
Al	0.47	237	q_2	473.118	473.117
			q_1	473.098	473.097
SiO_2	1.6	1.27 [7]	q_2	473.138	473.118
			q_1	473.099	473.098
Al	0.47	237	q_2	473.138	473.118
			q_1	473.099	473.099
SiO_2	0.8	1.27	q_2	473.148	473.138
			q_1	473.10	473.099
Si	375	130	q_2	473.15	473.147
			q_1	473.15	473.02

Table 3.1 Interfacial temperatures in the different layer of the sample produced by a thermal actuation of 200 °C

The theoretical model proves a quasi-null variation between the temperature applied and the one estimated in surface of the sample. The next section studies the thermal transfer in the solid by a FEM analysis. The heat flux is also corroborated in the next section with the FEM improved model.

3.1.3 FEM study

The previous mechanical FEM model (chapter 2) is improved in order to take into account the thermal behaviour of the device, considering now its complex geometry. In this way, both physics are applied simultaneously to consider a thermal actuation case.

Under the conditions studied, the heat provided at the bottom of the sample is conducted to the patterned top *Al* layer – almost 375 µm above the heat source.

In order to model the heat transfer in the structure, the "heat transfer in solid" COMSOL MULTIPHYSICS module uses the heat Equation 3.3.

For a steady-state problem and a velocity field (**u**) defined as zero, the first and second term disappear and the equation becomes:

$$\nabla \cdot (-k\nabla T) = 0 \tag{3.17}$$

So as to reduce the computation time of FEM model, the process is divided into two steps.

First, the *2D* model with the entire material stack is performed in order to identify the temperature and Heat Transfer Coefficient (HTC) at the device top surface. Then, a *3D* model is built to relate the temperature with the obtained rotation.

3.1.3.1 Thermal properties in technological stack: *2D* approximation

The natural convection cooling is studied by *2D* model first. Two different approaches can be considered to describe the thermal dissipation:

- Using heat transfer coefficients,

Or

- Modelling the convective flow of air around the structure, which solves the total energy and momentum balance between the device and the outside air flow around the structure.

The second approach is complex (many physical properties are needed) and very costly; we therefore consider that the Heat Transfer Coefficient approach has a better quality / cost ratio for our purpose to refine the previous *1D* analytical model.

The geometrical *2D* model, including the material stack in the structure from the bottom to the top is defined by Figure 3.6:

- Silicon (*Si*), 375 µm
- Silicon dioxide (SiO_2), 0.8 µm

- Aluminium (Al), 0.47 µm
- Silicon dioxide (SiO_2), 1.6 µm
- Patterned aluminium (Al), 0.47 µm

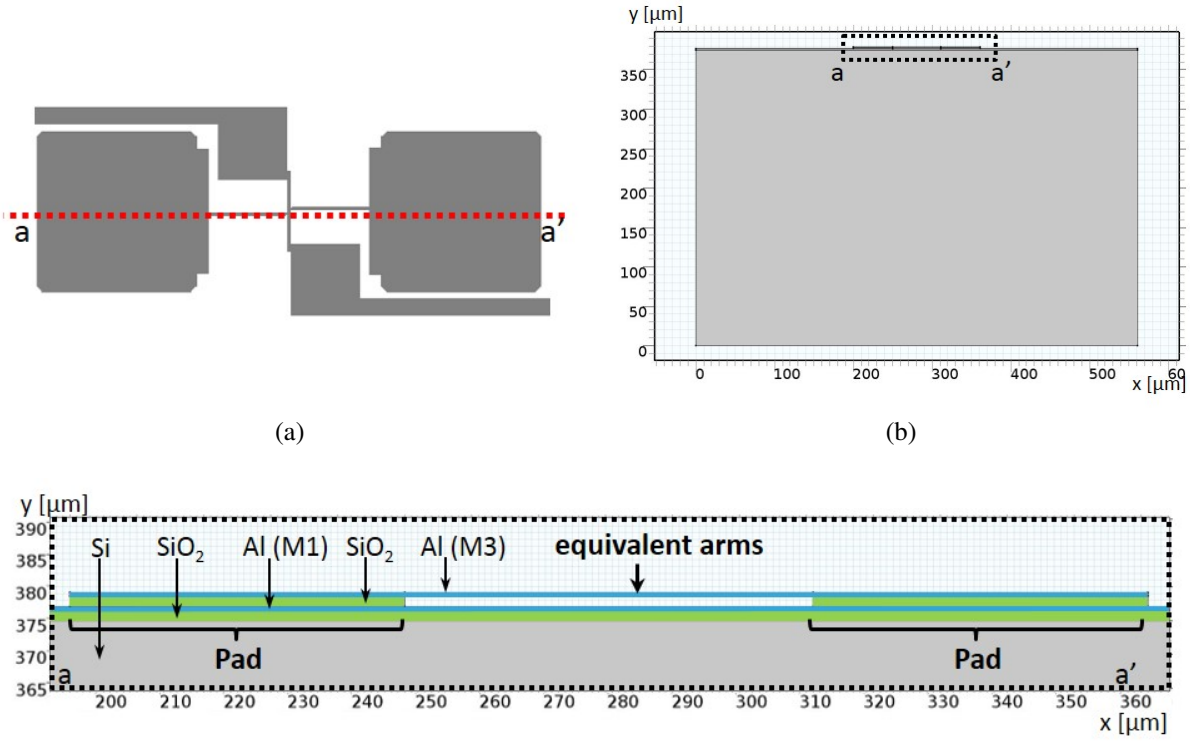

Fig. 3.6 *2D* model of the main structure, a) geometry used, b) cross section simulated, and c) detail of layer and structure description

The stack of the cross device (Figure 3.6) is defined in *2D* using the real dimensions (Figure 3.6b). The cross section of device is simplified as two pads connected by a hanging equivalent arm (Figure 3.6c). The thermal conductivities (k) for each material are: k_{Si}=130 W m^{-1} K^{-1} (100 W m^{-1} K^{-1}<k_{Si}<150 W m^{-1} K^{-1}), k_{SiO_2}=1.4 W m^{-1} K^{-1}, k_{Al}=237 W m^{-1} K^{-1}. The initial temperature in all system T_i=20 °C is also defined as initial condition. A radiative flux is defined on the free surfaces. The emissivity of oxidized aluminium at 200 °C (0.11 [8]) is added in the model.

The HTC can be either calculated by the software or defined by the user. In this part the calculation of the HTC value is entrusted to the software. As an external natural convection is

chosen, the value of L (area/perimeter), the air absolute pressure p_A and the external temperature T must be defined. The software obtains HTC (h) by the function $h = h_{air}(L, p_A, T_{ext})$[1] [9] – where $L = 51.4\mu m$. A temperature T_0=200 °C is applied on the bottom of the sample – *i.e.* at the bottom of the silicon substrate.

Figure 3.7 shows the temperature and the HTC on the top of *M1* metallic layer (red dotted line in Figure 3.7a). In order to simplify the display of results, the *M1* layer is divided (vertical black dotted line) into: *M1* (free layer), pad and equivalent arms zones.

The 200 °C applied in the bottom of the sample remains almost invariant in the top of *M1* metallic layer (199.8 °C). The arm is less heated by conduction than the pads (Figure 3.7b), because it loses heat by radiation and convection with the air. The arm temperature will be treated in next section.

Both the temperature and the HTC (30.2 $W m^{-2} K^{-1}$) are consistent with the values obtained in the previous section (subsection 3.1.2) – *i.e.* 199.95 °C and for a HTC from 5 to 250 $W m^{-2} K^{-1}$.

In order to relate the temperature in the structure with the rotation of the arms a *3D* model is realized in the next section. An average of the temperature estimate on *M1* layer (*2D* FEM model) is used as initial condition in the next section. Meanwhile, the HTC value will be defined in the same way as for the *2D* model.

[1] If $T > T_{ext}$ then $h = \begin{cases} \frac{k}{L}0.54Ra_L^{1/4} & \text{if} \quad Ra_L \leq 10^7 \\ \frac{k}{L}0.15Ra_L^{1/3} & \text{if} \quad Ra_L > 10^7 \end{cases}$
while if $T \leq T_{ext}$ then $h = \frac{k}{L}0.27Ra_L^{1/4}$
Ra_L is the Rayleigh number, L is the plate characteristic length (defined as area/perimeter) is a correlation input, and k is the thermal conductivity. The material data are evaluated at $\frac{T+T_{ext}}{2}$.

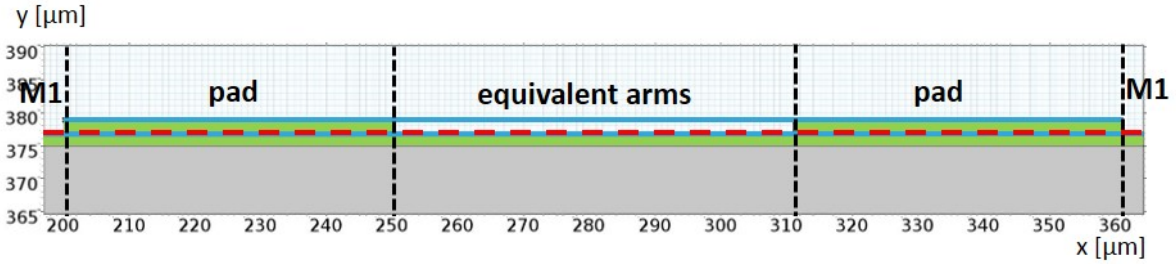

(a)

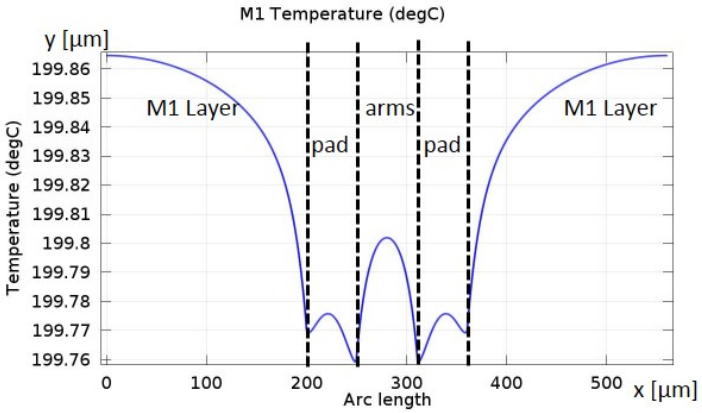

(b)

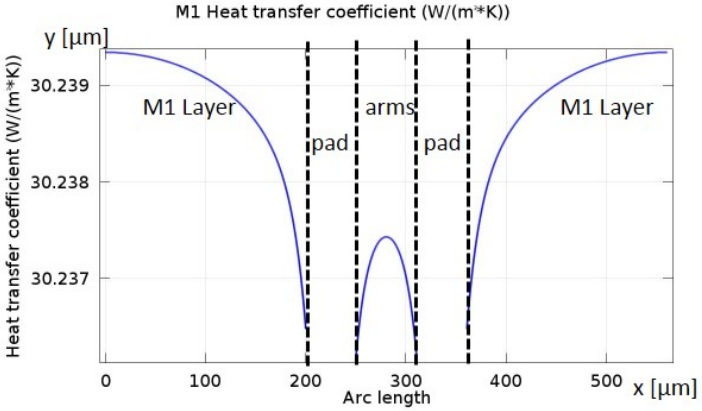

(c)

Fig. 3.7 Result of *2D* FEM that represented in *M1* metallic layer, a) detail of layer and structure descriptive b) temperature, and c) heat transfer coefficient

3.1.3.2 Rotation of structure: *3D* approximation

A simpler *3D* FEM model that does not include all layers is performed. To do that, the geometry model considers the *M1* full metallic layer, the residual SiO_2 (under the pads) and the patterned *M3* layer (Figure 3.8).

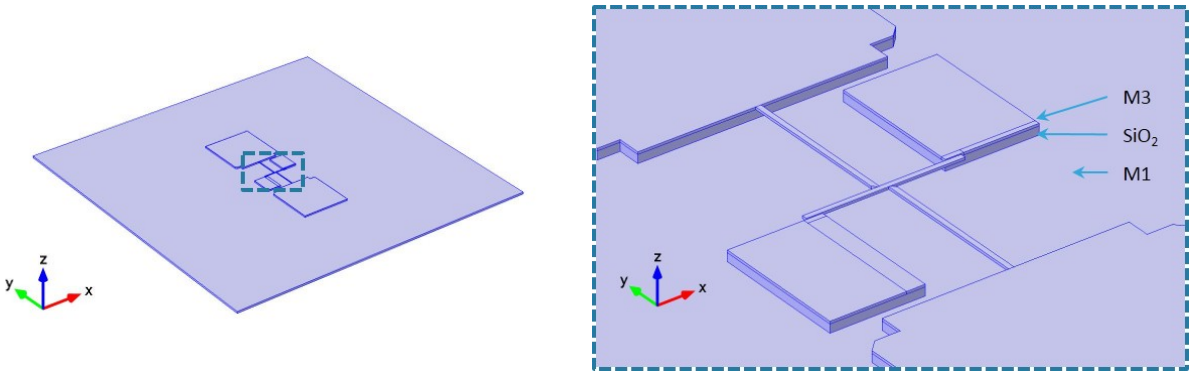

(a) (b)

Fig. 3.8 Geometry used in FEM *3D* model

The "heat transfer in solid" Comsol module is used in this FEM part. Only the initial value of temperature and the emissivity of oxidized *Al* ($\varepsilon_{th} = 0.11$) needs to be set on the initial conditions.

The boundary conditions, that is to say the thermal insulation ($\mathbf{n} \cdot (k\nabla T) = 0$) and the applied temperature (T_0 =200 °C) are defined in Figure 3.9a. The initial temperature in all system T_i =20 °C is also defined as initial condition. The HTC is calculated by the software as external natural convection (like the *2D* FEM model) for the following conditions: the external temperature of 20 °C; the absolute pressure of 1 *atm*; and the plate diameter (area/perimeter) of diffusive surface of 5.14×10^{-5} m are defined.

The mesh is composed with 72 313 tetrahedral elements, 139 602 prism elements, 11 250 hexahedral elements and 95 946 triangular elements, which are condensed in thinner metallic layers (Figure 3.9b).

Figure 3.10a shows the rotation of the cross-shape structure. Even if a NORMALLY *Off* structure is studied, no contact conditions are defined in the pad to observe free pointer rotation at all temperatures and compare with the fitted experimental curve of Figure 3.4.

As the temperature of 200 °C is applied at the top of *M1* layer, it can be seen:

- The pad is close to 200 °C

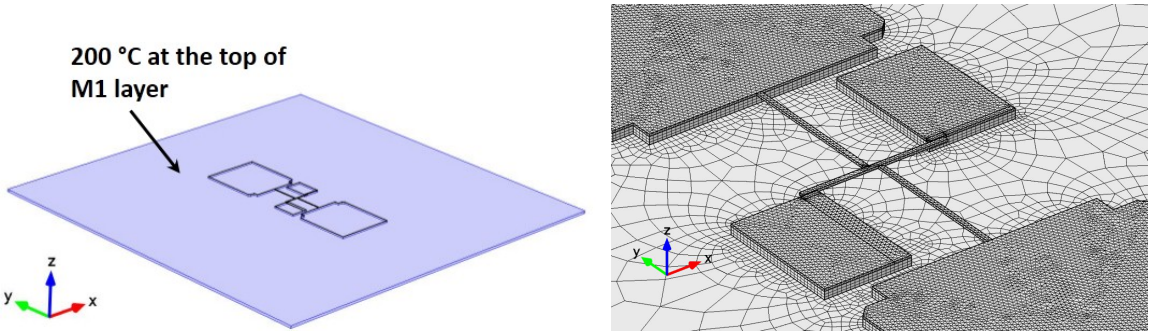

(a) (b)

Fig. 3.9 a) The boundary conditions, initial temperature imposed at the top of *M1* layer, the thermal radiation is defined (surface emissivity $\varepsilon_{th} = 0.11$) in all free surfaces (*M1* and *M3*), and b) Mesh of *3D* model

- The cross is less heated by conduction, and it loses heat by radiation ($h_{rad} \sim 2Wm^{-2}K^{-1}$) and convection ($h_{conv} \sim 21Wm^{-2}K^{-1}$, which is near to the $30Wm^{-2}K^{-1}$ obtained in *2D* FEM Model for the M1 metallic layer). Thus, the centre of the cross has the minimum temperature (165 °C). Meanwhile, the average temperature in the arm can be considered at 180 °C

- When the contact is reached, the ends of the pointer should warm up a bit, but the thermal contact is not handled here.

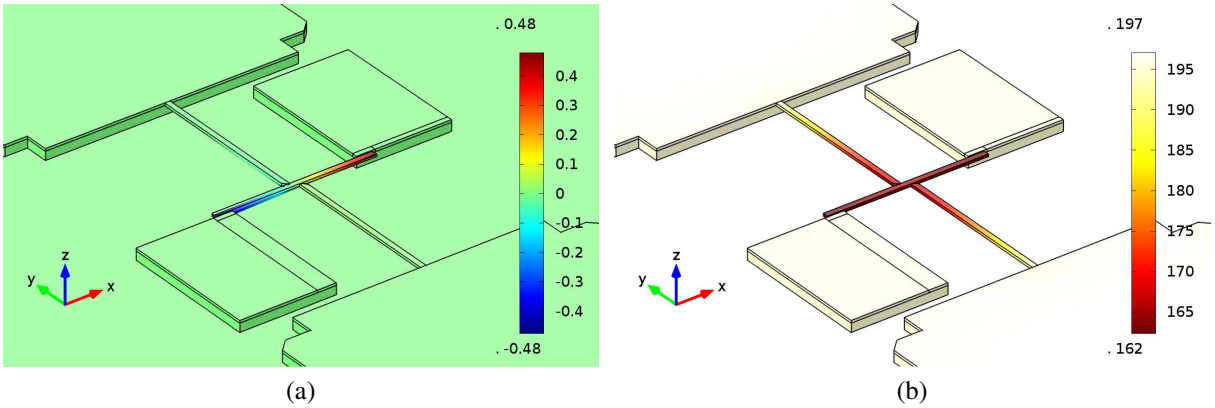

(a) (b)

Fig. 3.10 FEM model of thermal actuation and rotation induced in the cross-shape structure, a) the displacement in '*y*' from its original position and b) temperature gradient on the cross-shape

Figure 3.10a shows the distance between pointer and its original position of 0.48 µm. This distance assures the contact, originally at 0.25 µm from the pointer's original position. Remember that contact is not managed in the pad, so a free rotation of pointer is linear.

We can then compare the experimental data (*in-situ* SEM test) with the fitted curve (subsection 3.1.1) from the FEM analysis. Figure 3.11 shows this comparison: the three curves are very similarly shaped.

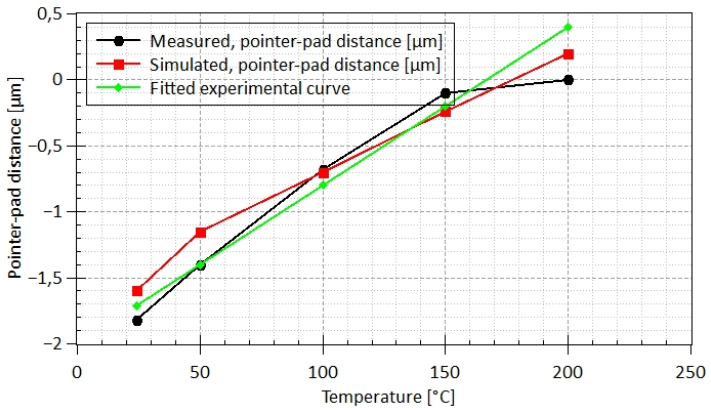

Fig. 3.11 Nominal temperatures applied and distance pointer-pad obtained – comparison between FEM study and previous *in-situ* test data

The FEM model corroborates the data obtained in *in-situ* SEM test (subsection 3.1.1). The temperature for the *M1* metallic layer is identified by a *2D* FEM Model, which is then used in a simplified *3D* version. Using the *3D* model, a temperature of 180 °C in the arms, required to activate the structure, are validated through the arms rotation. As this actuation temperature is well below Al melting point, the structure can be considered viable at this stage.

In order to simulate a voluntary actuation, the next section studies a Joule heating actuation.

3.2 Joule effect actuation (NORMALLY *Off* structures)

A controlled actuation of the device is performed using Joule effect. Joule's first law relates the heat produced (q) to the electrical power – the square of current (I) by the resistance (R).

$$q = I^2 \cdot R \tag{3.18}$$

In the first stage, the Joule effect actuation is simulated using the thermal characteristics established in the previous thermal actuation. Then, the experimental electrical characterization is realized with SEM nanoprobing experiment.

3.2.1 Extension of FEM study: Thermal to electrical actuation

The previous FEM model considered the mechanical and the thermal models, now it is upgraded with the electrical model. The material properties of aluminium include this time an electrical conductivity (σ_{elec}) of $35.5 \times 10^6 \mathrm{S\,m^{-1}}$ [6].

A *steady-state* FEM analysis is performed for each current step – 0 to 20 mA by step of 5 mA. Thus the temperature and displacement values obtained are measured from equilibrium state.

Boundary conditions are separated according to the studied physics:

- MECHANICAL: The initial stress is applied in arms and pointer that are shown in Figure 3.12. The pads of the structure are defined as blocked surfaces ($u = 0$).

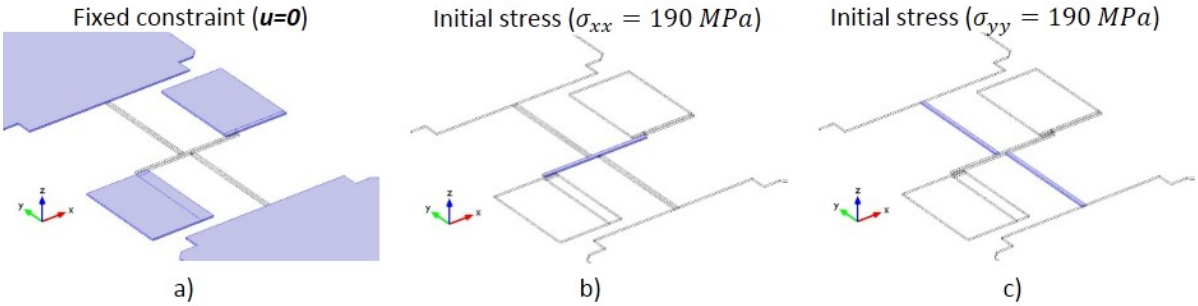

Fig. 3.12 Boundary conditions of mechanical modulus of COMSOL MULTIPHYSICS, in a NORMALLY *Off* structure at initial state – before stress relaxation

- ELECTRICAL: The boundary condition on the ground (V=0) and the electrical terminal (I applied) are defined in Figure 3.13.
- THERMAL: The entire structure has an initial temperature of 20 °C. The HTC is calculated by the software as external natural convection (like the pure thermal FEM Model)

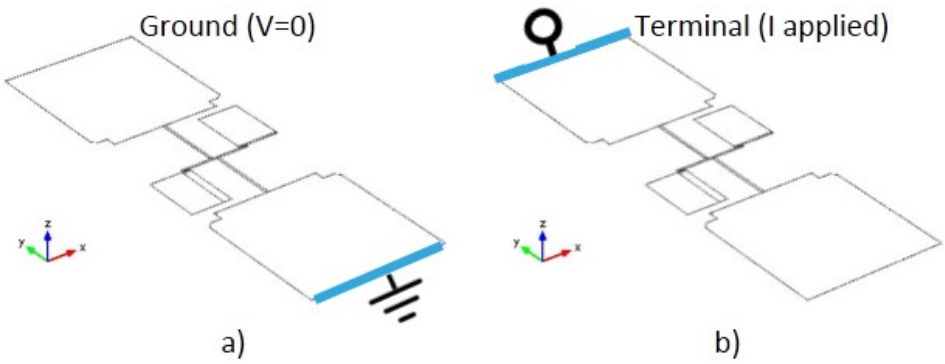

Fig. 3.13 Boundary conditions of electrical module of COMSOL MULTIPHYSICS

for this: the external temperature of 20 °C and the absolute pressure of 1 atm are defined. The emissivity of oxidized *Al* ($\varepsilon_{th} = 0.11$) is also set on the initial conditions.

The Mesh is made of 20535 tetrahedral elements (Figure 3.14a). The FEM model of the structure represents the rotation and the temperature reached with a flux of 20 mA through the actuation arms (Figure 3.14b).

The entire structure is originally at room temperature (20 °C). The contact is not managed by the FEM model – *i.e.* the contact pads conserves the initial 20 °C. The temperature shown in Figure 3.14b probably overtimates the temperature in the pointer tip area. The hottest point (181 °C) in the structure is the centre of the pointer, at the hinge zone.

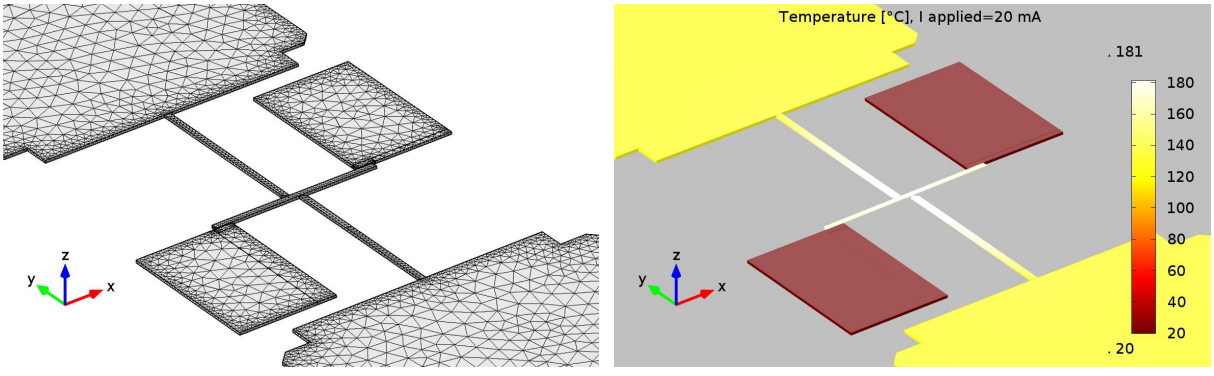

(a) (b)

Fig. 3.14 a) Mesh composed by 20535 tetrahedral elements, and b) the temperature in the structure with a maximum in the centre of the cross, which is generated by a flux of 20 mA

The maximum temperature obtained in this actuation model (181 °C) supports the temperature needed in a thermal actuation. Indeed, in the thermal actuation experiments the contact is

reached at 195 °C in the pad, while in the centre of cross a temperature of 165 °C is estimated. Thus, for a thermal actuation the hottest part is the pad (Figure 3.10b), while for a Joule actuation, the hottest point is in the centre of the freestanding cross (Figure 3.14).

The pointer-pad distance as a function of the applied current is shown in Figure 3.15. A current of 20 mA is needed to reach the contact, which corresponds to 80 mV. The non-linearity of the rotation, as a function of current, will be explained by the Joule heating temperature [10] – *i.e.* heating of the suspended beam causes its resistance to rise.

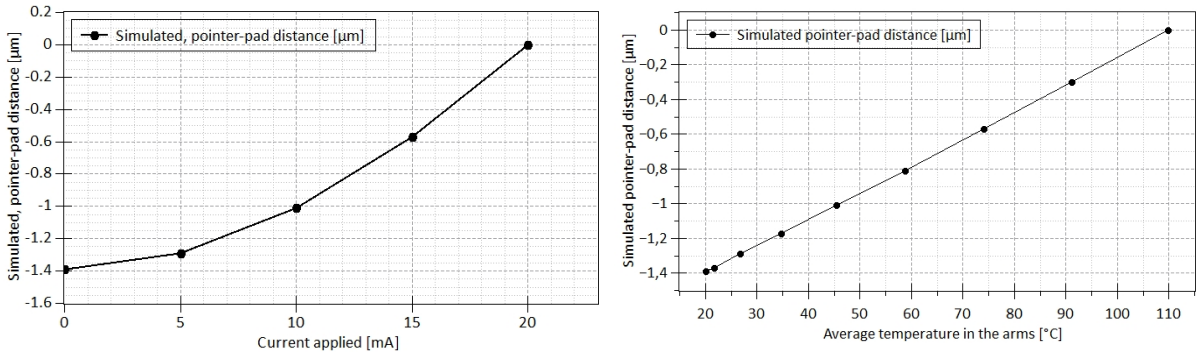

(a) (b)

Fig. 3.15 Evolution of pointer-pad distance as a function of a) current applied, and b) average temperature in the arms

Figure 3.15 shows a linear evolution of the pointer-pad distance as a function of the average temperature in the arms. It is confirmed that the average temperature of the arms is less than 181 °C. The temperature needed by Joule effect to reach the contact is ∼160 °C. This temperature, which is close to the 165 °C found in the thermal actuation, proves the feasibility of integrating these devices in a CMOS manufacturing flow.

In order to validate this numerical model an electrical test is performed in the next section. Using a nanoprober system, embedded in a SEM, the rotation of a few tens of nanometers can be measured.

3.2.2 Model verification: SEM nanoprobing

In order to characterize the displacement of the structure as a function of the electric current applied, a SEM nanoprobing test is performed. The accuracy of the displacement is in the range of 50 nm and the measurement uncertainly of electric equipment is ± 5 %.

3.2.2.1 Test performed in NORMALLY *Off* structure

The test is performed on the NORMALLY *Off* structure. The SEM stage has four motorized tips connected – shown in Figure 3.16. To ensure a current flux in actuation step, tips *C* and *D* are connected to actuation pads. Tip *B* is connected to the right contact pad to detect an electrical contact of the pointer – chosen randomly. Finally, tip *A* is connected to the metallic *M1* layer – the stop layer of the release process. Tip *A* evacuates the charges generated by the current flow, which otherwise reduces the quality of SEM images.

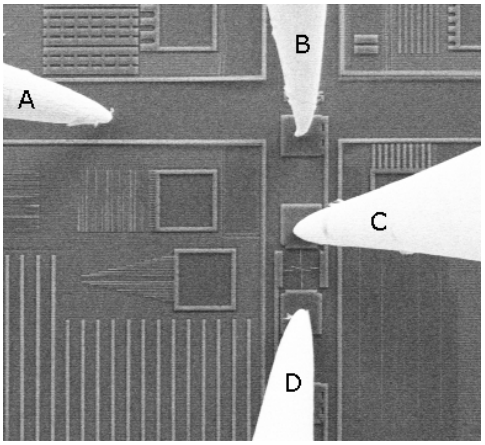

Fig. 3.16 Example of tips connections during SEM Nanoprobing test

The equivalent circuit defined by the tips connections of Figure 3.17a is shown in Figure 3.17b. The electrical resistances R_{arms1} and R_{arms2} are the equivalent resistances in the top and bottom arms respectively.

3.2.2.2 Discussion of results

The tested structure, after release, has an initial pointer-pad distance of 1.7 µm (Figure 3.18) – *i.e.* at 0 V and 0 A.

The electrical current is increased in the arms, activating the mechanism that generates the rotation of the pointer. The current is increased by steps of 2 mA (instantly), then held during 2 min to allow enough time to measure the rotation – the measurement of pointer-pad distance

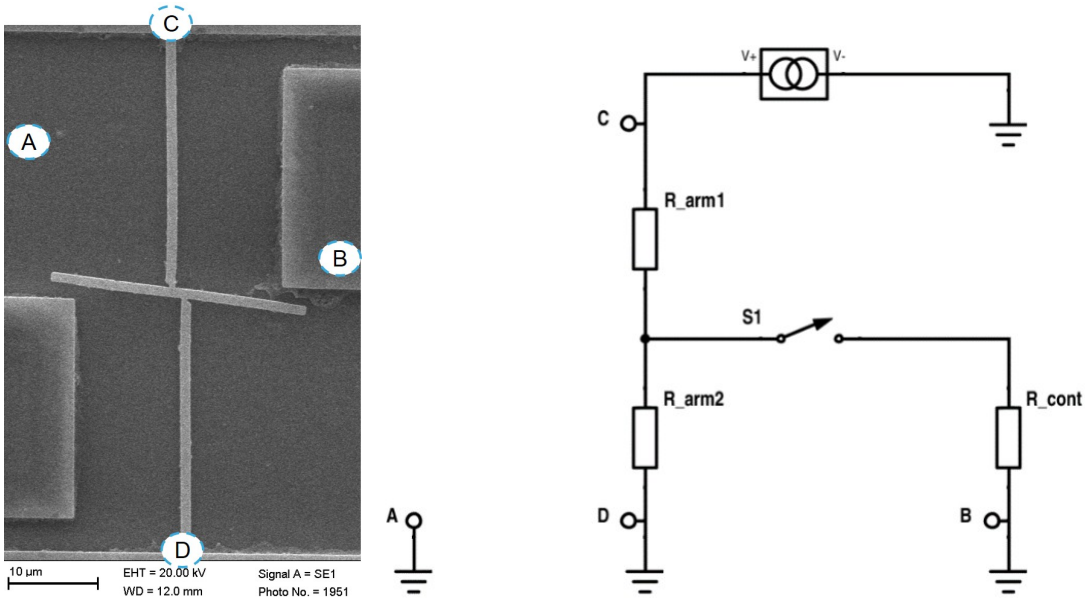

(a) (b)

Fig. 3.17 a) The nodes represented on the device, and b) equivalent circuit obtained by connections used in SEM nanoprobing test

is performed only when the current is increased (when the structure is heated). Since Senturia's model [11] will be used to derive an estimate of the temperature from the current.

The pointer moves towards the contact pad, which reaches contact at 23 mA/0.56 V (13 mW). Intermediate positions between start and contact, with the corresponding voltage/current pairs, are also shown in Figure 3.18.

The relationship between the voltage applied and the pointer-pad distance obtained in nanoprobing test is shown in Figure 3.19. The relationship established in previous section (subsection 3.2.1) is show as "Simulated, pointer-pad distance". Because the pointer-pad distance at rest position is not equal between simulated (1.4 µm) and nanoprobing test (1.7 µm), the "offset of nanoprobing test" curve is added to the graph for easier comparison.

Both the nanoprobing test and the FEM study have the same tendency. However, the pointer/pad distance was estimated at 1.5 ± 0.2 µm, so the results are in the variability of the pointer-pad distance in the structure.

The current needed to reach the contact is 23 mA measured in electrical test, which is close to the 20 mA needed to reach contact for the FEM model.

The difference found for the voltage measured and the voltage simulated, can be explained by the access resistance generated by the probes. The FEM model is an ideal case without

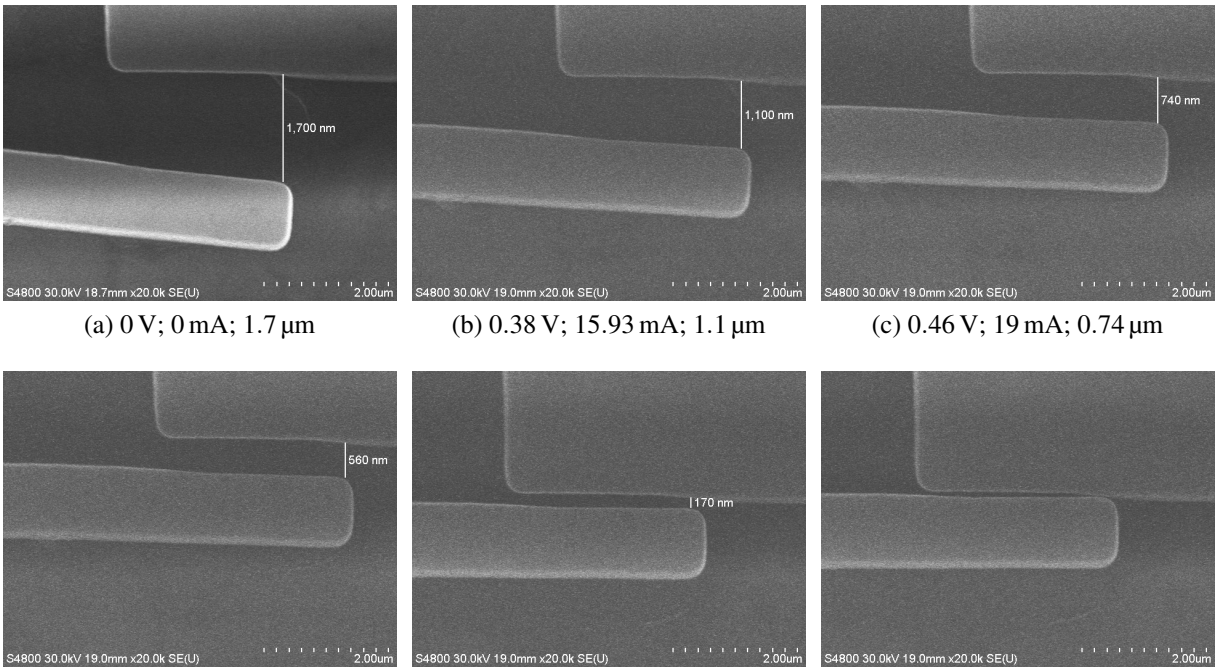

(a) 0 V; 0 mA; 1.7 µm (b) 0.38 V; 15.93 mA; 1.1 µm (c) 0.46 V; 19 mA; 0.74 µm

(d) 0.49 V; 20.15 mA; 0.56 µm (e) 0.55 V; 22.1 mA; 0.17 µm (f) 0.56 V; 23 mA; 0 µm

Fig. 3.18 SEM images of contact zone, where the pointer rotates to the contact pad for a high temperature generated by Joule heating.

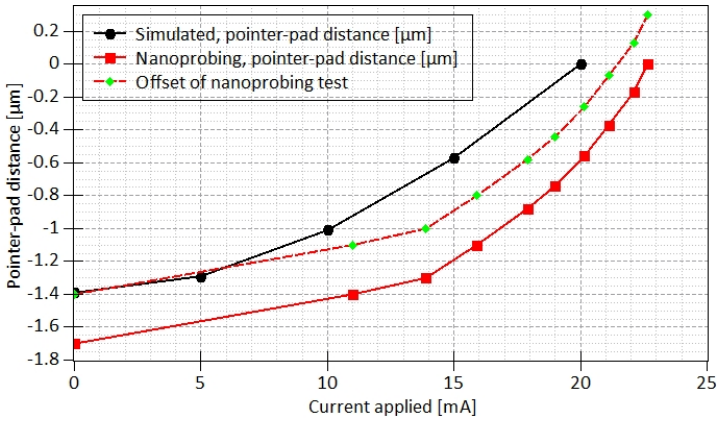

Fig. 3.19 Experimental current / displacement relationship for a NORMALLY *Off* structure obtained in a nanoprobing test – reaching a contact at 23 mA (0.56 V)

access resistance, therefore the data allow to model a resistance – *e.g.* I=20 mA, V=80 mV and R=4 Ω.

Knowing an $I-V$ characteristic for the cross structure, the access resistances can be calculated. The resistance and the tension drop in the actuation arms, obtained by FEM model, 4 Ω and 80 mV respectively are used in the next equivalent circuit model.

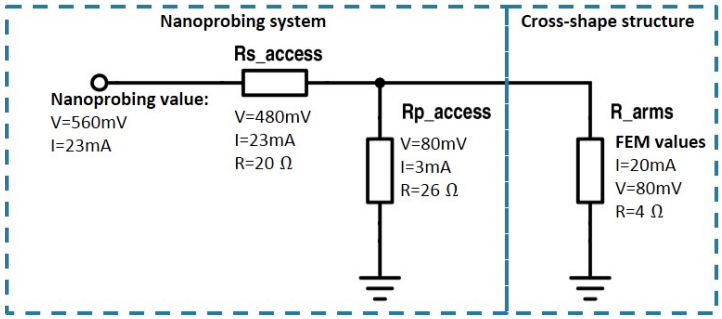

Fig. 3.20 Equivalent circuit of nanoprobing test, which consider the ideal FEM electrical values and parasitic resistances of nanoprobing system

In order to understand the mechanism linking the applied current with the temperature reached on the system, the Senturia model is used next.

3.2.2.3 Theoretical model

First, using an analytical model on self-heating of a resistor Equation 3.19, the global temperature of the structure is determined. The analytical model from S.D. Senturia ([11]) is used to adjust the self-heating phenomenon and determine the increase in temperature Equation 3.20.

For moderate temperature excursions, the temperature coefficient of resistance (using first order Taylor series expansion), shows a linear variation of resistance with temperature:

$$R = R_0[1 + \alpha_R(T - T_0)] \tag{3.19}$$

where R_0 [Ω] is the resistance at reference temperature T_0 (293.15 K), R [Ω] is the resistance at temperature T, and α_R is the temperature coefficient of resistance, 3.75×10^{-3} K^{-1} for *Al*. The electrical resistance along the arms at room temperature R_0=2.47 Ω was measured under low current condition using a *4-point probes method*.

The steady-state temperature (T_I) for a steady current I is [11] [1]:

$$T_I = T_0 + \frac{R_0 R_T I^2}{1 - \alpha_R R_0 R_T I^2} \tag{3.20}$$

[1] This equation explains how a metal fuse works. For a sufficiently large current, the denominator vanishes, the temperature rise diverges, and the fuse melts.

where R_T is the thermal resistor [$\mathrm{K\,W^{-1}}$], representing the heat conduction from the resistor to a thermal reservoir held at temperature T_0.

Using Equation 3.20, the only unknown parameter is the constant R_T. To adjust all the measured values of R in the 0-23 mA range, using Equation 3.19, R_T is determined by linear regression method. The electrical resistance values are well fitted by the Senturia's model using,

$$R_T = 100000 \left[\frac{K}{W}\right] \tag{3.21}$$

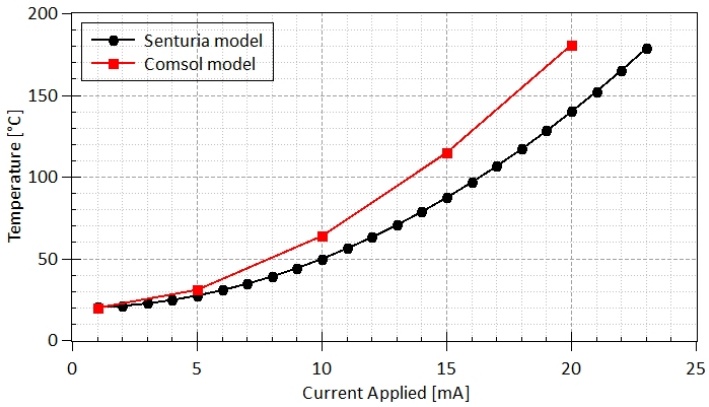

Fig. 3.21 Current applied in function to temperature generated in the arms – Senturia and FEM model

Figure 3.21 shows both the Senturia model and the FEM model. The curves fit in the small current densities, but for equivalent higher current, the FEM results has the highest temperature. This difference can be explained by the fitted linear first-order model of Senturia, which is valid for low temperature variations.

The actuation of NORMALLY *Off* structure was conducted by structure heating both homogeneous and localized. Both show that the temperature needed is far from the melting point of aluminium (660 °C), which shows that actuation is feasible in practice.

The theoretical studies, Senturia model for Joule heating and heat equation for thermal actuation, match well with experiments and with the FEM model.

The FEM study fits well the temperature at which the contact is achieved in both cases. Moreover, the FEM model takes into account the mechanical behaviour and the thermal/electrical part, forming a complete actuation cycle *i.e.* release and actuation.

In the next section, a test structure will be used to determine de contact force for both NORMALLY *On* and NORMALLY *Off* design. Then the FEM model is improved to take account of the mechanical contact.

3.3 Mechanical contact

3.3.1 Contact at release step (NORMALLY *On* structures)

In order to measure the contact force after release, another test structure with identical dimensions is created:

- Inverting the expansion arms, like a NORMALLY *On* structure, the switch turns counter-clockwise at release.
- A flexible beam is used instead of a pad (Figure 3.22). Its deflection gives the contact force.
- The vertical pointer (parallel to actuation arms) is a reference to measure the deflection in the contact beam.

The structure with this operation mode is called NORMALLY *On*– because it stays in contact in its rest position (in the absence of actuation).

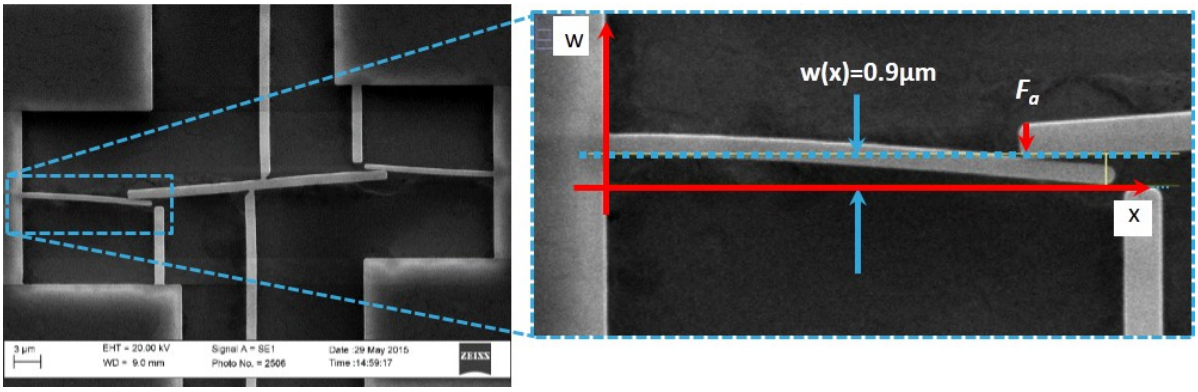

Fig. 3.22 SEM image of the test structure after release. The cross structure rotates and pushes the horizontal flexible beam 0.9 µm from its original position

3.3.1.1 Theoretical model: Euler-Bernoulli beam theory

Despite an apparent contact area of 0.2 μm^2, for this model, the contact is considered as a point contact. The contact of NORMALLY *On* structure is modelled as a force applied that bends in the plane a flexible beam (Figure 3.22). To obtain the force F_a that generates the displacement w at x position ($w(x)$) on the pointer of length L, the Euler-Bernoulli beam theory is used in a beam with a point load case.

$$w(x) = \frac{F_a}{6EI} \cdot x^2(3L - x) \tag{3.22}$$

$$F_a = \frac{6EIw(x)}{x^2(3L - x)} \tag{3.23}$$

where F_a is the force applied at point x, E is the elastic modulus, I is the second moment of inertia of the beam cross section and L is the beam length. Comparing with the measured deflection, an equivalent force F_a of 2.0 ± 0.5 µN for the device is obtained. The estimated error of 0.5 µN comes from the approximation made in the deflection measurement of SEM image. This estimate will be useful for electrical contact study (chapter 4).

3.3.1.2 FEM analysis of mechanical contact at release stage in a "NORMALLY *On*" structure

The FEM analysis is performed on the standard structures, which at release stage reaches the contact pad – *e.g.* the NORMALLY *On* structure.

The boundary conditions (Figure 3.23) are similar to those defined previously in the mechanical study. The definition of a contact pair, which in COMSOL MULTIPHYSICS, is composed of a "destination" and a "source" (Figure 3.24) makes possible the study of the mechanical contact.

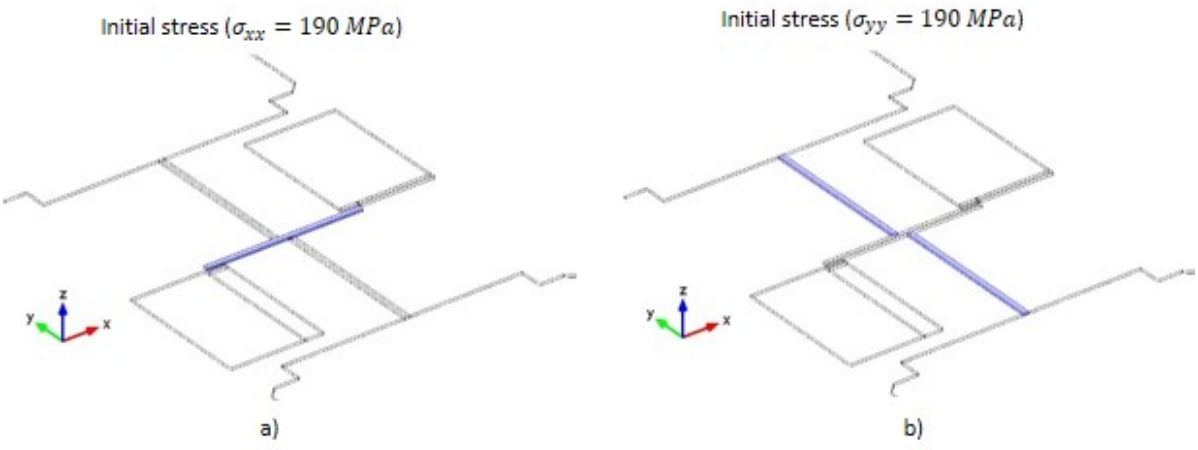

Fig. 3.23 Boundary conditions in mechanical model for the NORMALLY *On* structure, performed to measure the contact force, a)the initial stress along the pointer (σ_{xx}), b) the initial stress along the arms(σ_{yy}).

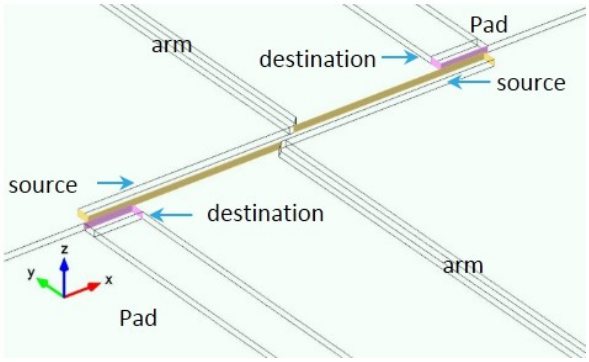

Fig. 3.24 The contact boundary conditions, source and destination of contact pair

Figure 3.24 shows the boundary defined as a contact pair – *i.e.* the couple "pointer/pad". The "source" is defined as mobile (pointer), while the "destination" is defined as fixed and "receives" the contact (pad).

The simulation results of Figure 3.25 show the contact zone and the contact pressure, which reaches a maximum of 50 MPa – *i.e.* an average pressure of 40 MPa.

The zoom of the contact area (Figure 3.26) allows measuring the surface in contact 4×10^{-14} m^2 (0.04 µm^2) which multiplied by the contact pressure gives the contact force:

$$F = P \cdot A = 40[MPa] \cdot 4 \times 10^{-14}[m^2] \approx 1.6[\mu N] \tag{3.24}$$

This value corresponds with the estimation made previously, by the theoretical model of the experiment (2 µN), and confirms again the correctness of the FEM model. Similarly, it confirms once again the correct choice of σ_{yy}=190 MPa along the arms.

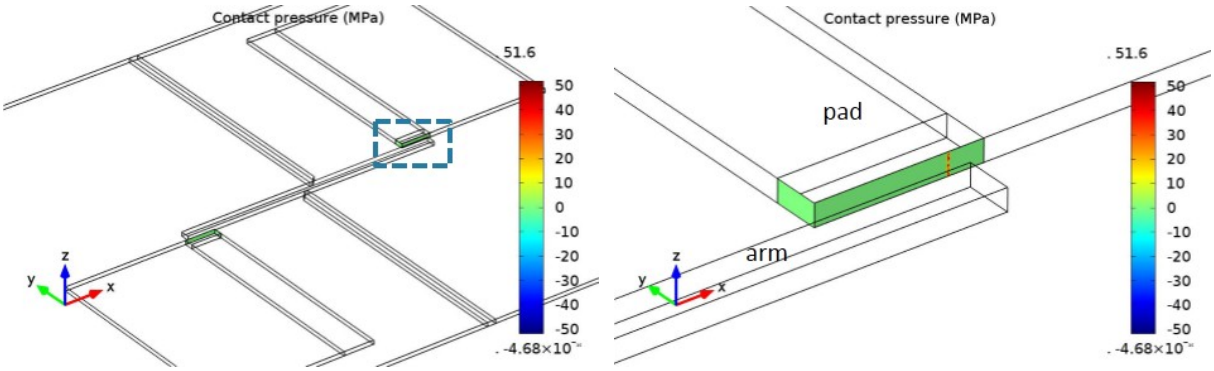

(a) (b)

Fig. 3.25 FEM result of the contact pressure on the pad, which is inflicted by the pointer

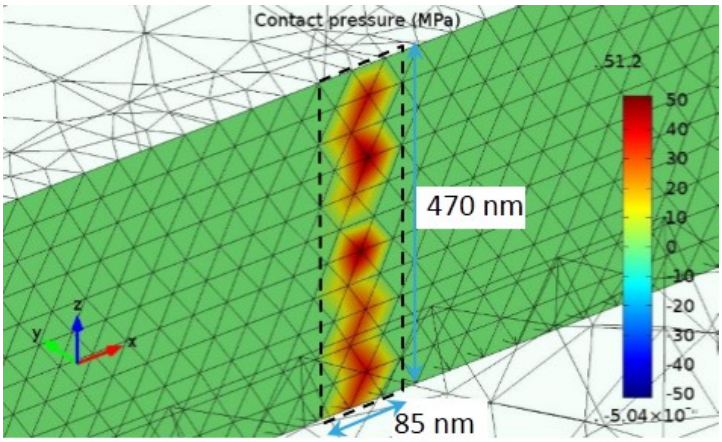

Fig. 3.26 Zoom of the contact zone on the pad

The FEM model allow to estimate the real contact area, which evidences the difference between the apparent contact area observed on SEM images – *e.g.* 0.2 µm^2 estimated (subsection 3.1.2) versus 0.04 µm^2 simulated.

Measuring the contact force in a structure during its actuation is difficult, because of the small dimensions of the contact (less than 1 µm) as well as the complexity of the lateral contact. In order to identify the contact force reached at actuation step in a NORMALLY *Off* structure a FEM analysis is performed in next section.

3.3.2 Contact at actuation step: study of the expansion of the contact (NORMALLY *Off* structures)

In previous section the contact force is estimated and simulated for a NORMALLY *On* structure – contact is reached at release step. In this section a contact is modelled by FEM analysis for a NORMALLY *Off* structure – *i.e.* the contact is reached at actuation step.

It was demonstrated in previous sections that both the Joule heating and the thermal actuations reached the same temperature at the end of actuation (contact). Therefore, in order to obtain a mechanical contact and measure the contact force, only a Joule actuation is done.

The FEM model is similar to the one built in previous subsection 3.3.1.2, where a multiphysical model considers mechanical, thermal and electrical behaviour. In this section the mechanical contact defined by a contact pair is implemented – the same as Figure 3.24.

The contact is reached by an actuation realised with a current of 25 mA through the actuation arms. Figure 3.27 shows the contact area and the pressure applied by the pointer in the pad – only a part of the pad is simulated.

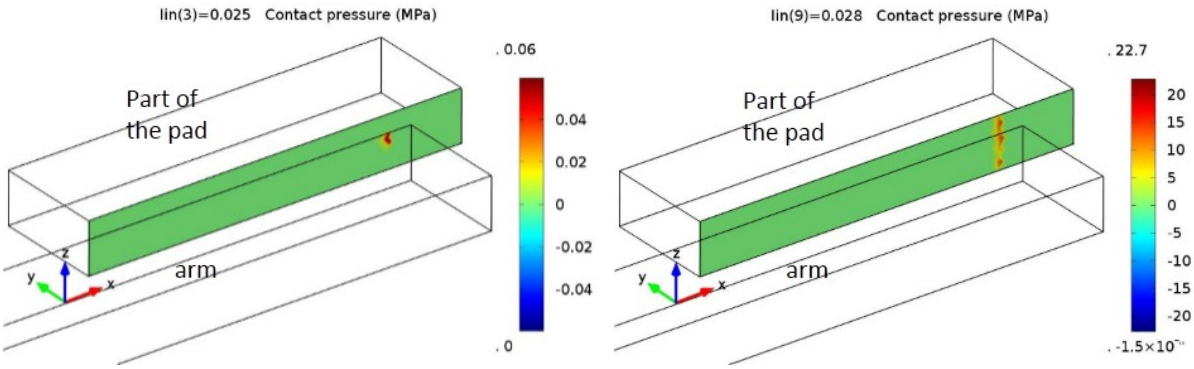

(a) (b)

Fig. 3.27 FEM image of contact pressure for a current applied of 25 mA and 28 mA

When the pointer barely touches the pad at 25 mA, the contact pressure is only 0.06 MPa in an area of around 80 nm × 80 nm (0.0064 µm^2). Then, the contact area increases to reach the 470 nm × 85 nm (0.04 µm^2) obtained for a NORMALLY *On* device. The contact pressure increases as the applied current increases.

The simulation results of Figure 3.28 show the contact zone and the contact pressure, which reaches a maximum of 22 MPa in this case.

The zoom of the contact area (Figure 3.28) allows estimating prudently the surface in contact 4×10^{-14} m^2 (0.04 µm^2) – similar to Figure 3.26 – which multiplied by the average contact pressure gives an approximation of the contact force:

$$F = P \cdot A = 15[MPa] \cdot 4 \times 10^{-14}[m^2] \approx 0.6[\mu N] \tag{3.25}$$

This value of the contact force is obtained for an actuation current near the maximum allowed by the device (see chapter 4) – *i.e.* 29 mA. For this reason, the contact force cannot be greater than 0.6 µN.

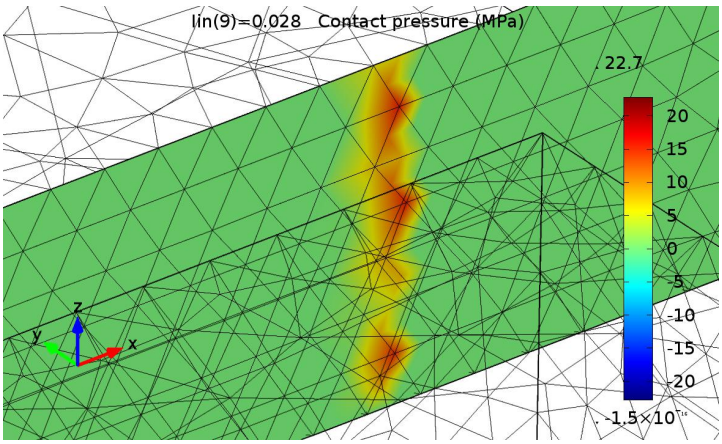

Fig. 3.28 Zoom of the contact zone (Figure 3.27b) with a pressure applied on the pad

This contact force, is weaker than with a NORMALLY *On* structure. The weaker force of NORMALLY *Off* structure can be explained by the larger rotation needed just to reach the contact.

This section has studied the actuation step generated by a heating expansion arms both the Joule heating and the hot stage heating.

The Multiphysics FEM model is now complete, including: the mechanical part, to manage the stress relaxation, material deformation and mechanical force; the thermal module, to consider the thermal properties of material (*e.g.* thermal conductivity and heat transfer coefficient) and study of the material dilatation; electrical module, to manage the electrical behaviour, material resistivity, ground and electrical terminal and as well as heat source.

3.4 Optimization

The knowledge acquired at this point, after the study of the release and the actuation, allows proposing improvement to the structures for the future implementations, in order *e.g.* to enhance the contact, both electrical and mechanical, and to make the structures insensitive to the action of external temperatures excursions.

Thus the next section will explain the following new design. Temperature invariant structure: to avoid undesirable actuations caused either during fabrication (or encapsulation process) or by an uncontrolled homogeneous heating. This device has been designed, fabricated, simulated and tested.

3.4.1 Temperature invariant structure

In the first part of the research work described before, the only source of movement at release stage, to bring the structure either in the *On* or *Off* state, was residual stress. However, in a functional operation cycle and for certain applications, the device should only be enabled through a voluntary actuation. To prevent incidental thermal actuation *e.g.* by the remaining CMOS fabrication steps – annealing of 400 °C – a design improvement, the *X-MEMS*, is created (see Figure 3.29).

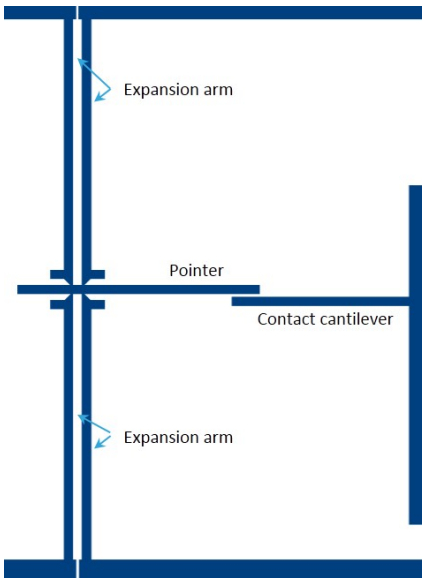

Fig. 3.29 Design of new robust design, invariant to external temperature variations and auto balanced for a residual stress

It consists of four symmetric counterbalanced arms connected to a pointer. The arms positioning counteracts the residual stress relaxation and avoids any rotation at release stage.

Moreover, if the four arms are heated homogeneously, the dilation is uniform and the rotation is avoided. Heating the arms heterogeneously by an actuating current, connecting either *C* and *B* or *D* and *A*, the pointer pulls asymmetrically and rotates clockwise or counter-clockwise respectively (Figure 3.31).

In order to confirm the operating principle, a FEM study was performed. In a first stage (Figure 3.30a) it was confirmed that the structure does not rotate after the release of an initial longitudinal stress state of +190 MPa in the arms. Then, a heat source of 400 °C was applied at the bottom of the sample (Figure 3.30b), producing a homogeneous conductive and radiative heating. Thanks to the symmetry of the arms, a negligible displacement of 0.9 nm at the end of the pointer is observed (Figure 3.30b).

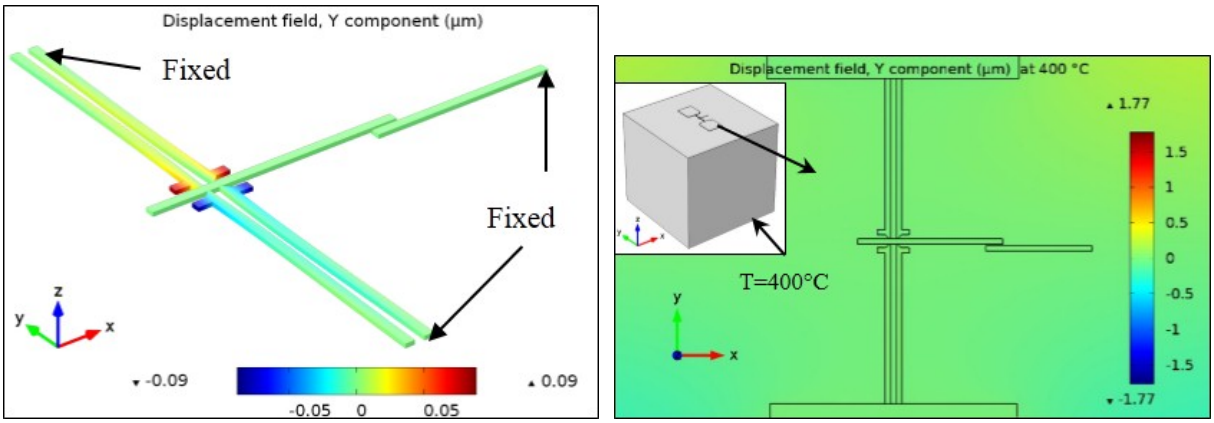

(a) (b)

Fig. 3.30 FEM result show no movement in both a) release stage and b) heated sample at 400 °C

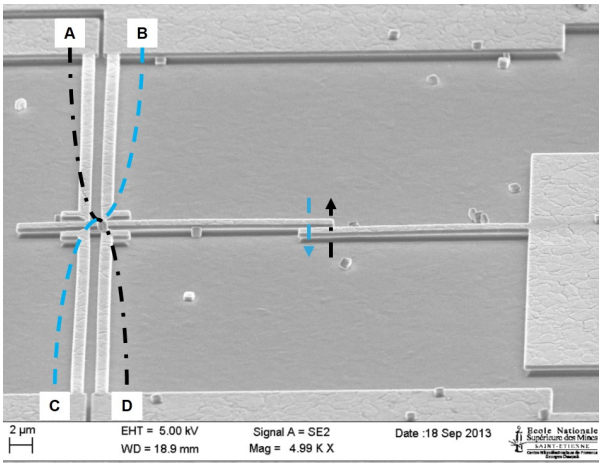

Fig. 3.31 Zoom of the contact zone (Figure 3.27b) with a pressure applied on the pad

Moreover, the stiction failure in the lateral contact zone at the *'On'* state can be avoided thanks to an opposing actuation. Thus for instance if the pointer is stuck due to the actuation of the arms *C* and *B*, a *D–A* actuation generates a contrary rotation and takes off the pointer, provided it is not welded. This case of reversibility is not present in a standard design – *i.e.* NORMALLY *On* or NORMALLY *Off* structure.

The proper functioning of the structure has been verified in a testing structure, without a contact beam. The rotation of the structure both clockwise and counter-clockwise are observed in the actuation trial test. The current needed to observe a rotation in the semiautomatic prober is slightly higher than for a standard structure – *i.e.* 28 mA.

Summary

Now that the rotational device has been correctly released and characterised, by FEM analysis and physical measurements, this chapter focuses on the actuation step. In this chapter, a study of actuation is carried out, using both thermal and electrical triggering.

The thermal actuation is performed in a hot stage embedded in a SEM. This experiment, visualizes the rotation of the device in function of the temperature applied. A linear relationship is found between the pointer-pad distance and the temperature applied as the arms dilate linearly. A theoretical model and the FEM study found the temperature on the top full metallic layer (*M1*) is quasi invariable from the 200 °C applied at the bottom of the sample.

The electrical actuation uses the Joule effect as trigger. Starting by an extension of previous FEM model a temperature of 110 °C is obtained when the pointer reaches the contact pad. The characterisation experiment is achieved by a SEM nanoprobing (a prober embedded in a SEM). The contact in this experiment is reached by 23 mA applied through the arms – *i.e.* similar to 20 mA obtained in FEM model.

The last part of this chapter is focused on the mechanical contact in a NORMALLY *On* structure (the structure reaches the contact at release stage). A design modification is carried-out. The contact pad is changed by a flexible beam, which allows to estimate the contact force at release stage. Both the experiment and the FEM model obtained a similar contact force, 2 µN and 1.6 µN respectively.

Finally, a new design to prevent accidental thermal actuation is proposed. This structure has been fabricated, simulated and passes the feasibility test.

Résumé français

La structure a été libérée, caractérisée et modélisée dans le chapitre précédent. Ce chapitre est consacré à l'étude de l'actuation des structures analysées. L'actuation est causée par l'échauffement des bras et leur dilatation, qui par conséquent fait tourner le pointeur central (chapter 2). La fonction attendue des structures est une actuation thermique contrôlée, c'est-à-dire une actuation par effet Joule. Pour cela deux grandes parties sont abordées dans ce chapitre.

Premièrement, et afin d'estimer des caractéristiques thermiques propres au système, une actuation thermique est réalisée. L'échantillon est chauffé à sa surface inférieure dans une platine chauffante, la chaleur est transférée jusqu'aux structures, dilatant les bras et provoquant une rotation. Cette expérience, embarquée dans un Microscope Electronique à Balayage (MEB), permet d'obtenir une relation entre la température imposée et la rotation obtenue. A partir de ce test, le modèle FEM, qui à l'origine ne modélisait qu'un comportement mécanique, est amélioré et maintenant c'est un modèle couplé mécanique/thermique qui a été élaboré.

Deuxièmement, l'actuation provoquée par une source de chaleur localisée, c'est-à-dire une actuation par effet Joule, est effectuée. Le modèle FEM qui a été développé précédemment est encore amélioré en introduisant un module électrique, qui prend en compte un échauffement par le passage d'un courant.

La position du pointeur central de la structure par rapport au plot de contact, après l'étape de libération, est associée aux deux modes de fonctionnement, "NORMALLY *On*" et 'NORMALLY *Off*". Pour les tests d'actuation précédents, une structure "NORMALLY *Off*" a été utilisée, cette structure s'éloigne du plot de contact dans l'étape de libération, ainsi la structure rentre en contact à l'étape d'actuation.

Dans la dernière partie, une structure "NORMALLY *On*" est utilisée ; au contraire, c'est dès l'étape de libération que le pointeur rentre en contact avec le plot de contact. En modifiant cette structure (le plot de contact est remplacé par une poutre mobile), la force de contact après libération est mesurée dans cette partie, elle vaut 1.6 µN. Comme dans les parties précédentes, cette étude est effectuée en trois temps : caractérisation physique, simulation multi physique et modèle théorique.

Bibliography

[1] N. Bozzolo, S. Jacomet, and R. Logé, "Fast in-situ annealing stage coupled with EBSD: A suitable tool to observe quick recrystallization mechanisms," *Materials Characterization*, vol. 70, pp. 28–32, aug 2012. [Online]. Available: http://dx.doi.org/10.1016/j.matchar.2012.04.020http://linkinghub.elsevier.com/retrieve/pii/S1044580312001179 95

[2] H. S. Carslaw and J. C. Jaeger, *Conduction of Heat in Solids*, 2nd ed. Oxford University Press, 1986. 99

[3] S. T. Todd and H. Xie, "Steady-state 1D electrothermal modeling of an electrothermal transducer," *Journal of Micromechanics and Microengineering*, vol. 16, no. 3, pp. 665–665, mar 2006. [Online]. Available: http://stacks.iop.org/0960-1317/16/i=3/a=C01?key=crossref.aeaa374dc77e0aca99d706e22d82b6af 101

[4] P. Gilgunn, Jingwei Liu, N. Sarkar, and G. Fedder, "CMOS–MEMS Lateral Electrothermal Actuators," *Journal of Microelectromechanical Systems*, vol. 17, no. 1, pp. 103–114, feb 2008. [Online]. Available: http://ieeexplore.ieee.org/lpdocs/epic03/wrapper.htm?arnumber=4441701

[5] B. Arrazat, S. Orellana, C. Rivero, P. Fornara, A. Di Giacomo, and K. Inal, "From stress sensor towards back end of line embedded thermo-mechanical sensor," *Microelectronic Engineering*, vol. 120, pp. 41–46, may 2014. [Online]. Available: http://linkinghub.elsevier.com/retrieve/pii/S0167931713007016 101

[6] L. B. Freund and S. Suresh, *Thin Film Materials*. Cambridge: Cambridge University Press, 2004. [Online]. Available: http://ebooks.cambridge.org/ref/id/CBO9780511754715 102, 110

[7] M. Burzo, P. Komarov, and P. Raad, "Thermal transport properties of gold-covered thin-film silicon dioxide," *IEEE Transactions on Components and Packaging Technologies*, vol. 26, no. 1, pp. 80–88, mar 2003. [Online]. Available: http://ieeexplore.ieee.org/lpdocs/epic03/wrapper.htm?arnumber=1202906 102

[8] Mikron, "Table of emissivity of various surfaces," Tech. Rep. 104

[9] T. L. Bergman, A. S. Lavine, F. P. Incropera, and D. P. DeWitt, *Fundamentals of Heat and Mass Transfer*, 6th ed. John Wiley & Sons, Inc., 2006. 105

[10] L. L. W. Chow, Z. Wang, B. D. Jensen, K. Saitou, J. L. Volakis, and K. Kurabayashi, "Skin-Effect Self-Heating in Air-Suspended RF MEMS Transmission-Line Structures," *Journal of Microelectromechanical Systems*, vol. 15, no. 6, pp. 1622–1631, dec 2006. [Online]. Available: http://ieeexplore.ieee.org/lpdocs/epic03/wrapper.htm?arnumber=4020258 112

[11] S. D. Senturia, *Microsystem Design*. Boston: Kluwer Academic Publishers, 2002. [Online]. Available: http://link.springer.com/10.1007/b117574 114, 116

Chapter 4

Performance

Contents

The structure has now been released and activated. A robust FEM model takes into account the multiphysical character of devices – mechanical, electrical and thermal. In this chapter the functionality of the structure (switch) is studied in terms of electrical contact (conduction efficiency) and reliability upon cycling – both electrical and mechanical. An ohmic electrical contact, repeatable and reversible, is desired. Then, in order to optimize the electrical contact resistance, two topics are studied:

- the repeatability of the movement upon Joule actuation (section 4.1),
- characterization of the surface in contact, in particular the oxides (section 4.2)

4.1 Structural reliability of the devices

To achieve a reliable and durable device in functional life cycle, the mechanical performances are studied in this section. Two problems are addressed:

- The structure, in its life cycle, will undergo thermal cycles from room temperature (25 °C) to 200 °C. Thus, the potential plastic material deformation during thermal actuation cycles is studied ([1]).
- The current flow through the arms occasionally results in melting and fracture of the arms, possibly triggered or accelerated by electromigration ([2, 3]). Thus, the overheating during the actuation stage is treated in subsection 4.1.3.

4.1.1 Displacement study and residual stress after release step

Residual stress is the driving force of the initial positioning of the switch (NORMALLY *On*/ NORMALLY *Off*). During the release stage, part of this stress is relaxed. The structure is then confronted to cycling and switching, which both generate microstructure modification and stress relaxations. The study of this residual stress is a key element in order to determine the functional life and reliability of device. The analysis of the stress which is not released is treated by non-linear FEM analysis (including plasticity) in this section[1].

The stress relaxation produces a rotation and a bending respectively in the pointer and in the arms. Figure 4.1 shows both the pointer displacement in 'y' direction (a) and the arms bending in 'x' direction (dx), which is quasi not measurable in SEM observation but can be modelled in FEM study.

The central pointer prevents the complete release of stress in arms, and causes arms to bend along x direction. This flexion in the XOY plane generates additional stress – largest in the hinge zone. The FEM calculus thus shows that on the internal side of the lower arm, next to the pointer centre, a tensile stress state is present. On the contrary, the external side undergoes a compressive stress state.

Using the same FEM model defined in subsection 2.2.2, an initial homogenous longitudinal stress of +190 MPa has been imposed along the arms and the pointer. Almost all of this stress is released.

The *3D steady-state* simulations are performed by the elasto-plastic behavior on the "structural mechanics" option of COMSOL MULTIPHYSICS.

[1] A limited trial licence of the non-linear mechanics module of Comsol is used to simulate the plasticity in the hinge.

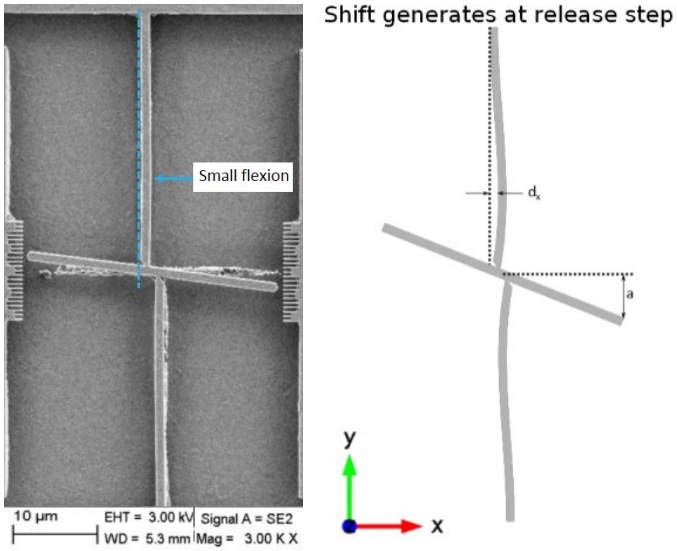

(a) (b)

Fig. 4.1 Demonstration of the bending in the arms, a) SEM image shows a small flexion, b) FEM image that amplifies by 5 the 'x' and 'y' shift generated at release step

The elasto-plastic deformation is observed in hinge vicinity. The maximum (red area) and minimum (blue area) y component of plastic strain tensor ε^{p}_{yy} are represented in Figure 4.2.

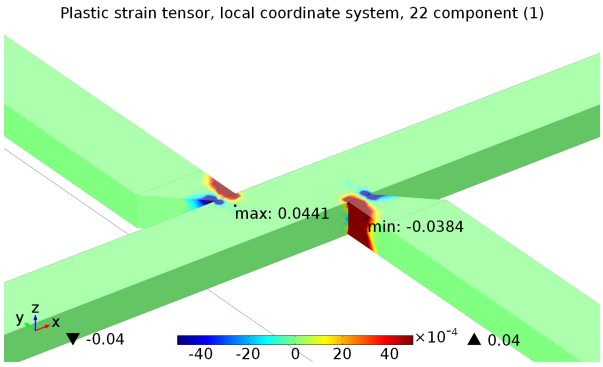

Fig. 4.2 Computed *y-component* of strain tensor (ε_{yy})in the hinge: 4 % of plastic deformation

The maximum strain reaches 4 % around the hinge; there is no gradient in the 'z' (thickness) direction. The internal side of the hinge (close to the centre of the pointer) shows a tensile strain which is opposed to the external side which has a compressive strain.

This plasticity observed by FEM (at release step), as well as the temperature actuation produces a thermal stress, which can plastify the structure and that will be present during the

device life. The next section studies experimentally the repeatability of the movement in the electrical actuation.

4.1.2 Repeatability of the movement

The reversibility of the movement is essential, as switching is supposed to occur thousands of times. In real operation, both ends of the pointer should therefore enter in contact with their pad at the same time. This is not necessarily the case initially (see Figure 4.3), as the pointer may not be strictly straight.

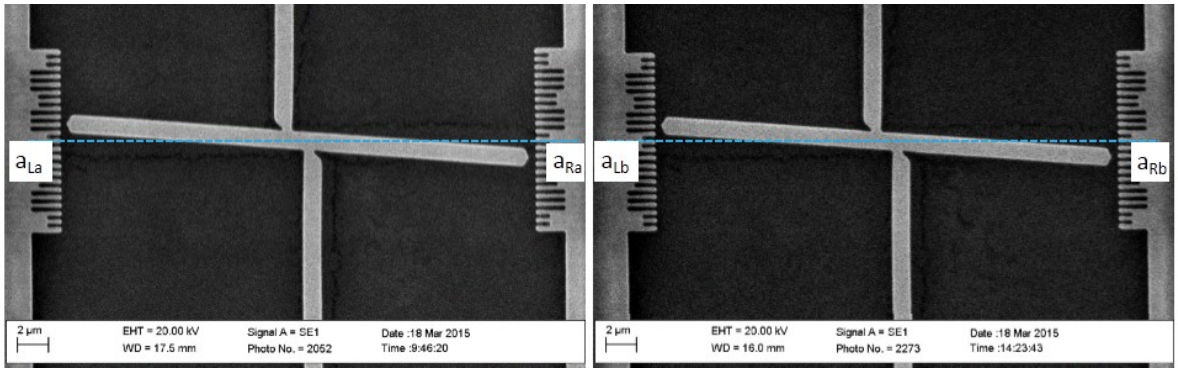

Fig. 4.3 SEM image with microscopic distance measurements of test structure, a) after release step, and b) after 1110 actuation cycles

To measure the displacement, a current of 12 mA is applied in the arms to activate the structure. The measurements are done on a specific structure where contact pads are replaced by micro-rulers; precise distance measurement is based on SEM image magnification.

The distance of pointer to their original position (a) is measured after release for left (a_{La}) and right (a_{Ra}) sides – blue lines in Figure 4.3 represent the distance measured. This distance is compared to distances after actuation cycling – a_{Lb} and a_{Rb} for left and right sides respectively, after 1, 10, 100 and 1000 cycles.

The distances a_L and a_R are not identical initially due to fabrication micro-defects. Figure 4.4 shows the evolution of a_L and a_R from the initial state after release to the final state after 1000 cycles. Initially, a_L differs from a_R by about 10 %. During the first 100 cycles, they slightly decrease and converge to a common value of 1.2 µm, then remain stable until 1000 cycles.

In this case, the effect of plastic deformation is positive as it makes the system symmetric as it should be. This deformation solves the irregularity of release (which could prevent simultaneous contact of pointer on both pads and the current flow), and suggests a running-in step before operation.

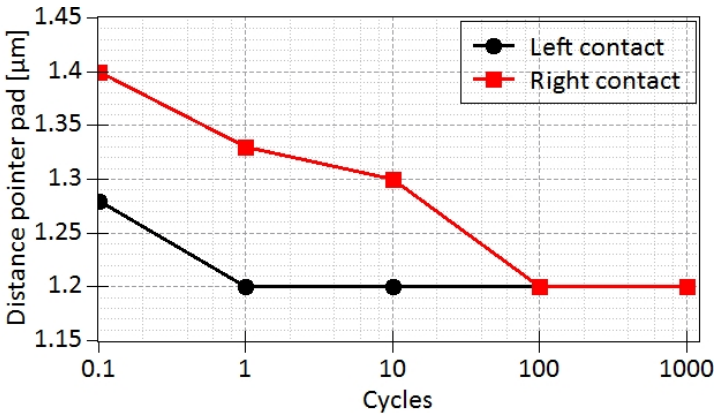

Fig. 4.4 Cycling test shows stability in pointer–pad distance up to 1110 *On-Off* cycles, after an initial running-in stage of 100 cycles

4.1.3 Maximum current allowed in a Joule actuation

The structure in Figure 4.1a has undergone the electrical break test, where high current is applied to force melting. It proves that a current of 30 mA damages the structure.

The failure, as shown in Figure 4.5, did not occur at the hot spot expected to be at the cross centre by symmetry (subsection 3.2.1). In order to explain the break position in the arms, a FEM study of the actuation has been carried out. The experimental electrical resistance and failure current are measured and related to the maximum temperature calculated from FEM at break ([3]).

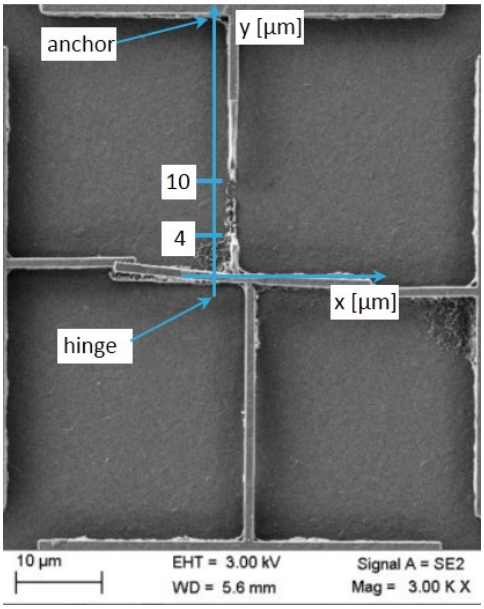

Fig. 4.5 SEM image showing the failure at $1/3$ of arm from hinge, around 8 µm from hinge

A pure thermal heating is not able to melt the arm, because in the chapter 'actuation' (chapter 3) it has been proved that the structure does not exceed 200 °C, much lower than the melting temperature of *Al*, 660 °C – temperature that is similar for *AlCu* ([4]).

The reason for fracture is therefore to be found in a combination of thermal and mechanical effects.

The computed displacement of the arm in *'x'* direction is plotted as a function of the current applied (Figure 4.1). The arms are fixed to the anchor, so no displacement is allowed at this point (on the right). In the initial state (after release) the arm is slightly curved toward centre of pointer – on the picture, upward in the real device; this is an effect of the stress that remains even after release (Figure 4.1). Under 29 mA, the line is strongly curved. The maximum of curvature is found around 8 µm from the hinge, which corresponds to the observed failure location.

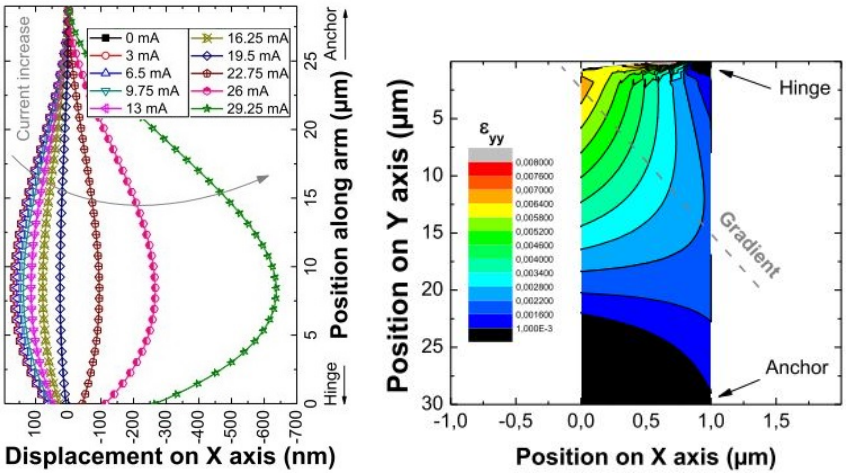

(a) (b)

Fig. 4.6 a) Displacement in *'x'* direction of the arm as a function of applied current, b) Top view of FEM study of the strain ε_{yy} on the surface of the arm

Figure 4.6a shows the flexion along the upper arm as a function of the applied current. The hinge zone moves from its initial rest position 0.3 µm, which proves that the whole cross structure moves to the right.

The strain ε_{yy} along the arm is showed at the top surface of the arms in Figure 4.6b. It is maximal in an area from 4 to 15 µm from the hinge, the maximum gradient is centred on 8 µm, which fits with the failure location.

Remarks:

1. This part of the work has given the maximum allowed current for these particular structures. To generalize it to all structures, it would be necessary to build a complete stress-based damage model, with a fracture parameter depending on temperature ([5]).

2. In a homogenous heating by an external source (hot stage) a similar break failure is not expected, since the maximal temperature to activate the structure in this case is about 180 °C (section 3.1).

4.2 Electrical switch functionality: contact conductance

To standardize the study of the electrical contact, only the NORMALLY *On* structures are tested in this section – contact is reached at release stage.

First electrical tests have shown very small electrical current (or very high contact resistance). Indeed, aluminium is easily oxidized in contact with air, so that oxidation could be the reason. Therefore, a chemical characterisation of contact surfaces is done to check oxide thickness.

4.2.1 Chemical analysis: contact surfaces oxidation

Aluminium in interaction with the air oxidises within 1 min [6]. The etching step in the fabrication process (B) is performed in an equipment under a vacuum, but the wafer fabrication process continues in a non-protected environment.

In contact with air, 4 to 5 nm of native oxide grows on aluminium surfaces [7–9]. It is generally termed alumina (Al_2O_3), although oxides and hydroxides may be mixed. This oxide is a good insulator: for Al_2O_3, dielectric permittivity 7.5 to 15 , volumic mass of 3000 to 3400 m^{-3}, and volume resistivity $>10 \times 10^{17}\,\Omega$m [10].

In order to characterise this insulating layer, both X-ray Photoelectron Spectroscopy (XPS) and Auger Electron Spectroscopy (AES) analyses were performed to identify the surface contaminants. XPS provides molecular study to identify accurately the chemical component. Complementary, the AES has a better spatial resolution, allowing the chemical identification on small zones.

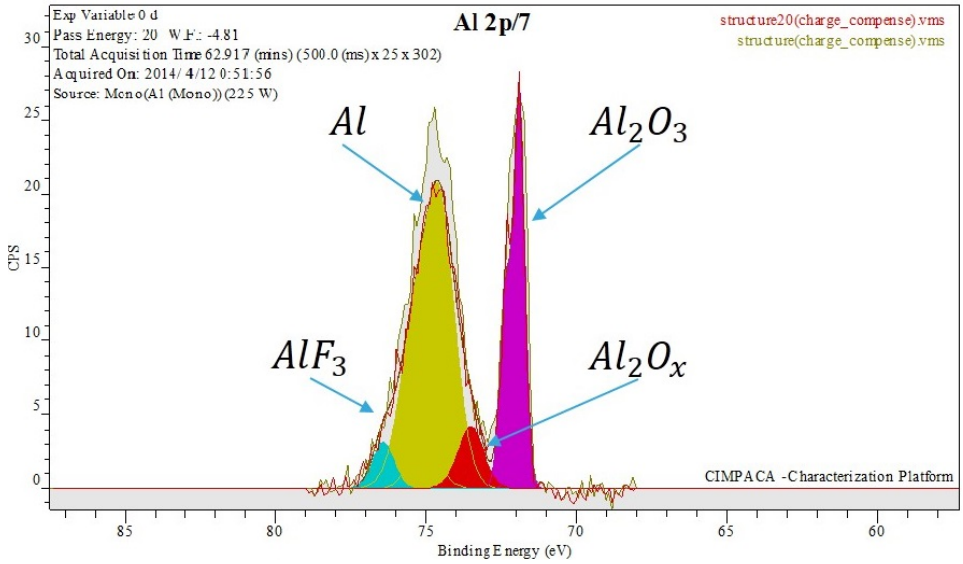

Fig. 4.7 XPS spectrum on the side of a pad – *Al* peaks analysis confirms the presence of aluminium oxides in the structure

The series of performed chemical measurements are explained in E. They confirm that on top of *Al* layer, a native *Al* oxide is present. The detailed analysis shows that it is mainly Al_2O_3. On the side, three compounds are detected by XPS analysis (Figure 4.7): aluminium oxide (Al_2O_3), aluminium fluoride (AlF_3) and a group of complex aluminium oxides and hydroxides defined as Al_2O_x. The fluoride detected is coming from the etching steps – as HF is utilised. Al_2O_x can be composed by an aluminium oxide hydroxide ($AlO(OH)$) or aluminium hydroxide ($Al(OH)_3$), which are difficult to distinguish by XPS analysis ([11]).

The thickness of alumina on the top of the sample could be obtained, from XPS analysis, using the calculation of Carlson ([12]) and Strohmeier ([13]).

$$d = \lambda_{Al_2O_3} \cdot \sin\theta_a \cdot \ln\left(1 + \frac{N_{Al} \cdot \lambda_{Al} \cdot I_{Al_2O_3}}{N_{Al_2O_3} \cdot \lambda_{Al_2O_3} \cdot I_{Al}}\right) \tag{4.1}$$

where θ_a is the photoelectron take-off angle, I represents the intensities (*i.e.* peak areas) of the metal and oxide photoelectron peaks, λ ($IMFP$) is the inelastic mean free path, and N is the volume densities of atoms in the metal and in the oxide, respectively. Using the λ and N proposed by Strohmeier ([13]) and the values obtained in XPS analysis (Table 4.1) an estimated Al_2O_3 thickness of 4 nm is obtained.

	% At Conc.	IMFP (nm)	$N_{Al_2O_3}/N_{Al}$	take-off angle
Al oxide	69.6	28	1.5	90
Al metal	30.4	26	1.5	90

Table 4.1 Theoretical and measured values, which allow measuring aluminium oxide thickness

In order to observe the insulating layer and verify the thickness obtained by the analytical approximation of Equation 4.1, a physical verification is performed by Transmission Electron Microscopy (TEM) analysis. Figure 4.8 shows a generic sample preparation, which is achieved in three steps:

- First, in order to protect the zone of interest, metal deposition is performed in several layers over a surface of 20 µm × 1 µm:
  - First Gold-Palladium, followed by
  - Platinum deposited electrochemically (to avoid damage on surfaces),
  - Platinum deposited ionically (to paste a tip and manipulate the sample).
- Second, in order to obtain an electron-transparent sheet, the sample is thinned (0.1 µm) by ion milling

- Finally, the sample is then ion milled again to shape a sheet 0.1 µm thick by 2 µm high and 10 µm long and manipulated with a tungsten (W) tip.

A Focused Ion Beam (FIB) is used for this purpose – installed on a dual beam TEM, a system with both electron and ion beam columns and a platinum injector. The ion milling is performed by the ion beam, using a gallium source, with an acceleration tension of 30 kV, in a vacuum environment (10×10^{-6} mbar).

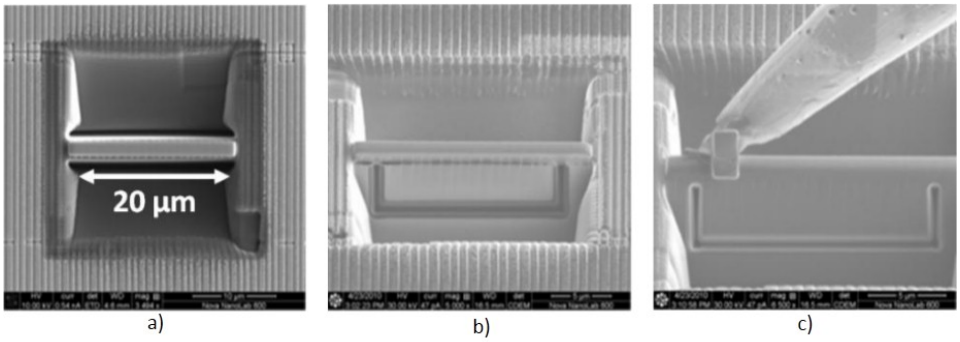

Fig. 4.8 Principal steps of the preparation of a standard TEM sheet by FIB dual beam machine, a) metallization over 20 µm, b) thinning of the sample and c) manipulation with a W tip

Figure 4.9 shows a TEM cross section of the contact interface, which allows visualizing the aluminium oxide layer on the top (4 nm) and on the sidewall (6 nm) of a pad. The difference of Al_2O_3 thickness can be explained by the fabrication process, where the top of Al layer undergoes anisotropic chemical attack, reducing the thickness of the oxide – *i.e.* process of photolithography like resin removal and the clean step.

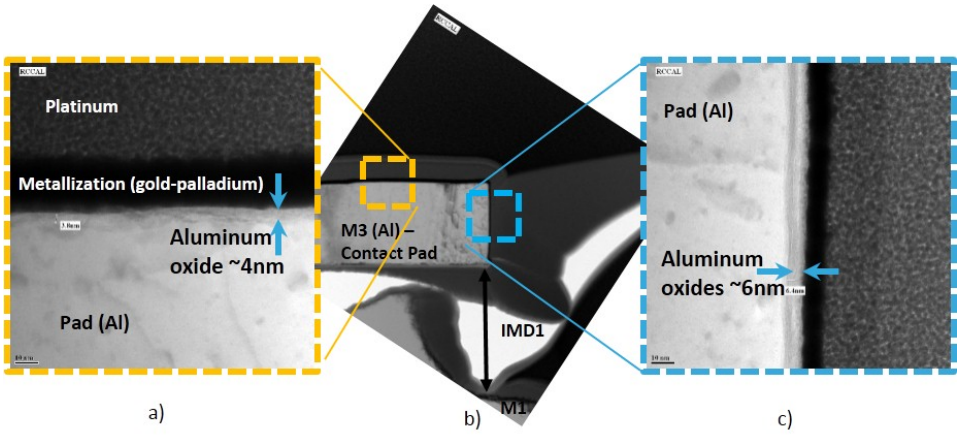

Fig. 4.9 Cross-section TEM images of the contact zone in a NORMALLY *Off* structure, a) top of the contact pad showing 4 nm of Al_2O_3, b) the contact pad, and c) contacting side showing an oxide layer of 6 nm

Electrically, the aluminium oxide prevents ohmic current through the contact. In order to pass an electrical current from pointer to contact pad, or vice versa, two possibilities are analysed:

- Either ensure a measurable tunnel current through the insulator layer, for applications where low current could be sufficient.
- Or add an oxidation-resistant interfacial material on the contacting surfaces to avoid or minimize the native oxide.

4.2.2 Tunnelling through the oxide

The 6 nm of aluminium oxides, measured on the sidewall of the pointer and the pad, becomes 12 nm in contact. It makes it difficult to expect an ohmic conduction. Instead of this, this section concentrates on the possibility to obtain and control a measurable and repeatable tunnel current.

4.2.2.1 Definition and electrical model

The cross section view of the contact zone shows a configuration similar to a MIM capacitor for a NORMALLY *On* structure (Figure 4.10). The interfacial layer configuration is represented in Figure 4.11 – *Al-Oxide-Al* sandwich.

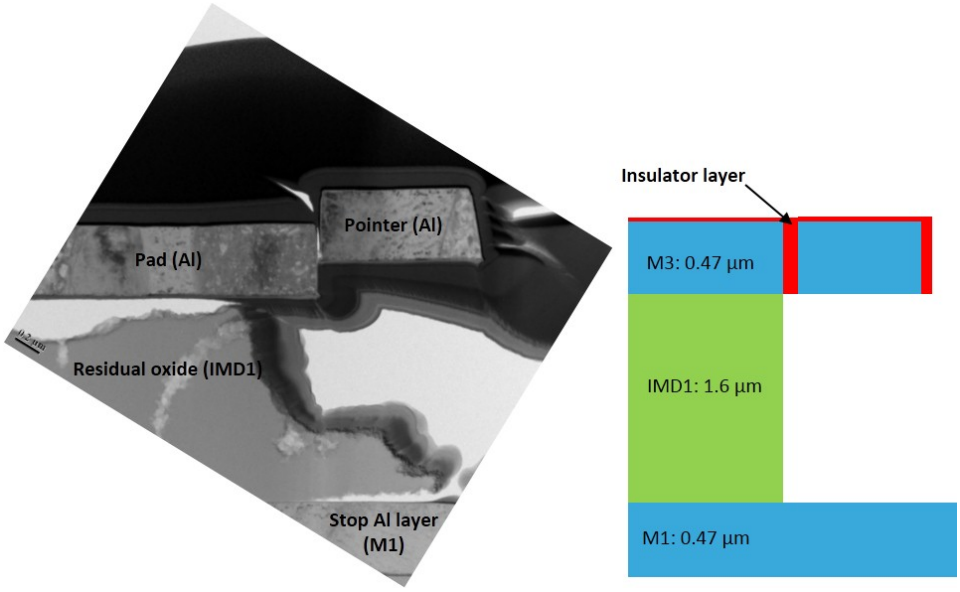

Fig. 4.10 Representation of MIM capacitor by a NORMALLY *On* structure after release step, a) cross-section TEM view, and b) schematic view, representing the contact

Consider an ideal symmetrical MIM structure. Temperature and the field-penetration effect in the metal electrodes are neglected. Thus, for a voltage higher than the potential energy barrier ($V > q\phi_B$), the well-known Fowler-Nordheim tunnelling equation characterizes the current density J_{FN} through the insulator [8, 14]:

$$J_{FN} = K_1 \cdot \xi^2 \cdot exp\left(\frac{-K_2}{\xi}\right) \tag{4.2}$$

where

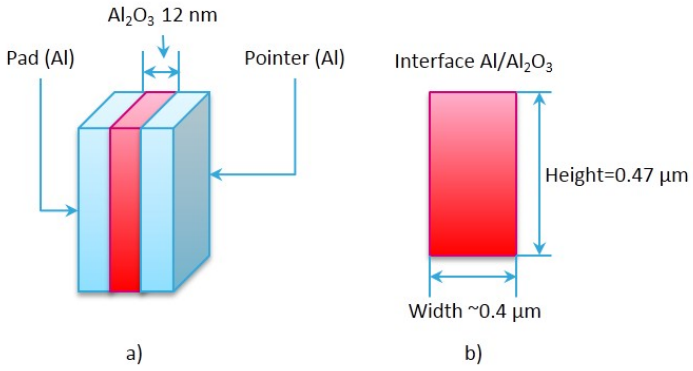

Fig. 4.11 Dimensions of the interfacial oxide at contact state (pointer/pad)

$$K_1 = \frac{q^2}{8\pi h \phi_B} = 1.538 \times 10^{-6} (\phi_B)^{-1} \left[\frac{A}{V^2}\right] \tag{4.3}$$

and

$$K_2 = \frac{8\pi\sqrt{2m^*}}{3hq} \cdot (q\phi_B) = 6.8 \times 10^9 \left(\frac{m^*}{m_0}\right)^{1/2} \cdot (\phi_B)^{3/2} \left[\frac{V}{m}\right] \tag{4.4}$$

where

m^*	electron effective mass in the dielectric
m_0	electron rest mass,
q	electron charge,
$q\phi_B$	Schottky barrier height (*i.e.* conduction band offset),
ξ	electric field in the dielectric,
h	Planck's constant.

Gloos [8] has studied the same material stack configuration – $Al/Al_2O_3/Al$. The electrical properties of native aluminium oxide vary between different studies [8, 9, 15]. Thus, considering $q\phi_B$=2.9 eV ([16]) (ϕ_B=2.9 V), m^*=3.64 $\times$ 10^{-31} kg ([8]), the Fowler-Nordheim current density is:

$$J_{FN} = 5.3 \times 10^{-7} \cdot \xi^2 \cdot exp\left(\frac{-2.13 \times 10^{10}}{\xi}\right) \tag{4.5}$$

An electric current of the order of nano-ampere (1 nA) is obtained for an electric field of 2.5×10^9 V m^{-1} (*e.g.* 30 V applied on an oxide 12 nm thick), in order to verify the theoretical data, an electrical test is performed.

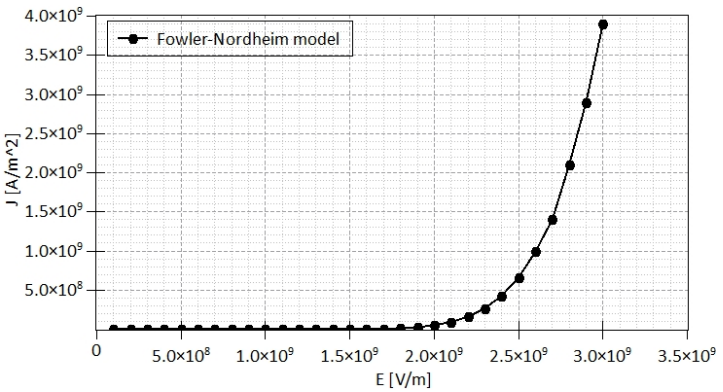

Fig. 4.12 Representation of Fowler-Nordheim model of Al_2O_3 native layer obtained in Equation 4.5

4.2.2.2 Electrical characterisation

The tunnel current flow is obtained by an imposed high electric field in the electrodes connecting the oxide – pad and pointer in this study. To carry out the test, two probes are connected: the ground (B) and the voltage source (A), meanwhile the current and voltage are measured in both terminals. The equivalent circuit of Figure 4.13a is modelled in Figure 4.13b. The contact is represented by a capacitor in parallel with a resistance, C_{S1} and R_{S1} respectively.

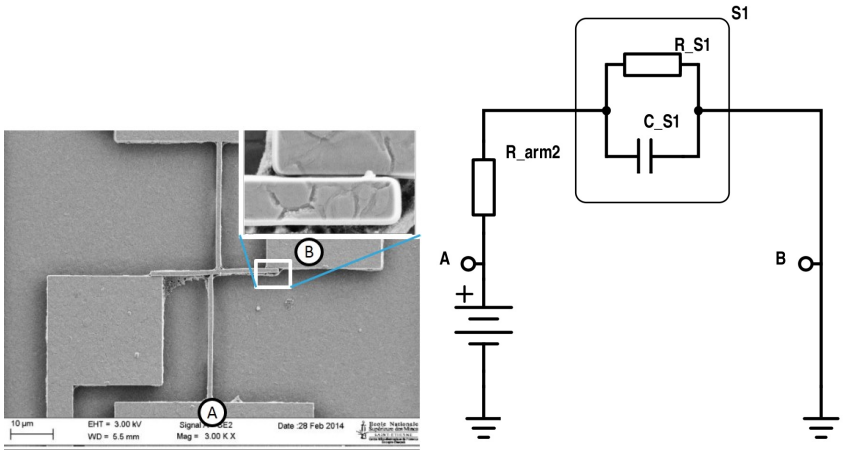

(a) (b)

Fig. 4.13 a) original device, and b) equivalent circuit created by the connection of the probes

In both A and B probes, the current and the voltage are measured. The current measured at B as a function of the voltage applied in A gives the I-V characteristic of the contact (Figure 4.14a).

In a FEM section of the previous chapter (subsection 3.3.1.2) the contact surface has been estimated as 0.04 µm^2 (4×10^{-14} m^2). For an applied electric field of 1×10^9 V m^{-1} the measured current density J_{FN}=1×10^4 A m^{-2}, represents a current:

$$I = J \cdot A = 1 \times 10^4 \left[\frac{A}{m^2}\right] \cdot 4 \times 10^{-14}[m^2] = 0.4[nA] \tag{4.6}$$

The weak current measured (Figure 4.14a) is comparable to the literature ([15]) (Figure 4.14b). Spahr's study ([15]) found a *I-V* characteristics for various aluminium oxide thicknesses (2 nm, 6 nm, 12 nm and 24 nm), the difference between them corresponds to different conduction mechanisms – *i.e.* Poole-Frenkel, Schottky emission, direct tunnelling and thermionic-field emission ([14]). Identifying the conduction mechanism and the traps present in the oxide is a complex work, especially for the small contact area.

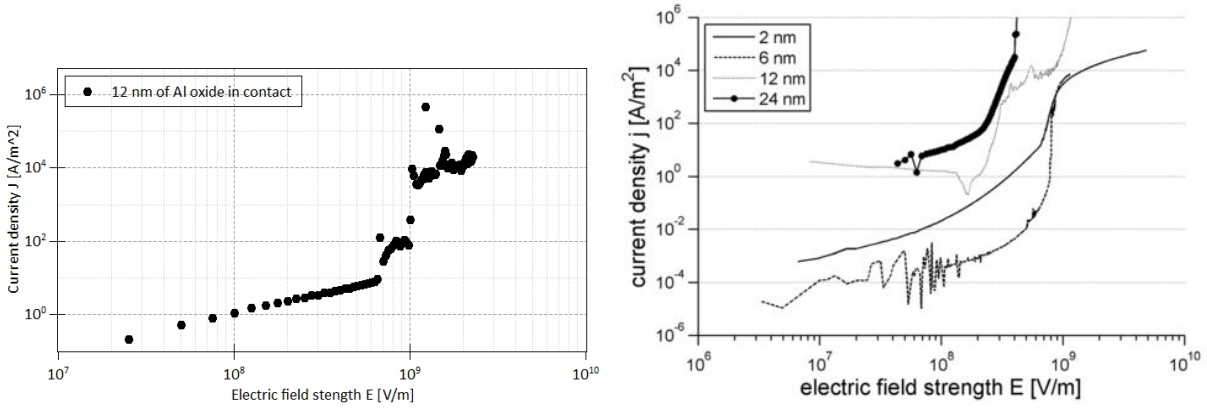

(a) (b)

Fig. 4.14 Current density vs electric field strength characteristics of contact, a) this study for 12 nm of Al_2O_3, b) Spahr [15] study of Al_2O_3 thicknesses of 2 nm, 6 nm, 12 nm and 24 nm

The oxide thickness in the contact state is 12 nm. The breakdown is obtained at 23 V, which represents an electric field of 19 MV cm^{-1} (1.9×10^9 V m^{-1}). The literature values of the breakdown electric field ([17, 18]) can be higher than 60 MV cm^{-1} for 1.2 nm, and 10 MV cm^{-1} for 6 nm thick of Atomic Layer Deposition (ALD) Al_2O_3 layer. In Gloos' study ([8]), on native aluminium oxide, a breakdown electric field of 50 MV cm^{-1} was found. In the same study, it is explained that for Al_2O_3 the breakdown voltage decreases strongly with the barrier height and the density of tunnelling electrons.

The differences observed in breakdown electric field have been the subject of many studies. Thus, electric field at breakdown depends on ([19]): the oxide thickness, the electrode material,

the mode of sample preparation, the material characteristics and the electron trap density present in the oxide layer.

When the oxide breakdown is achieved, the pointer and the contact pad or cantilever may melt (Figure 4.15). An ohmic resistance is then achieved but no further movement is possible.

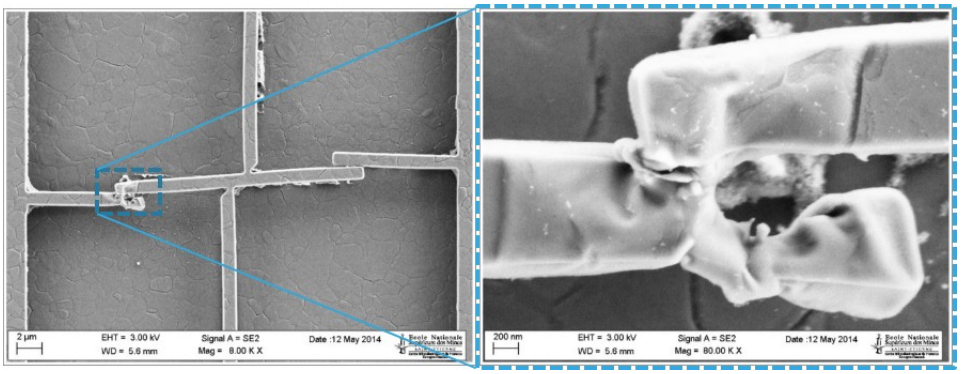

Fig. 4.15 SEM image after oxide breakdown and contact fusion

The switch concept is not yet achieved. The ohmic contact in the µA range, without damage to the structure, is not yet granted, neither for NORMALLY *On* nor for NORMALLY *Off* structures. A modification in fabrication process is then proposed and tested in next section.

In order to minimize the impact of the oxidation, an oxidation-resistant interfacial material is added in contact zone. A tungsten (W) coating on the side of Al structures has been chosen. This layer aims at protecting from oxidation, or at least at avoiding oxide growth. This protective layer is called spacer layer – similar to that used in transistor fabrication in the microelectronics industry ([20]).

4.2.3 Adding an interfacial material to improve electrical contact

The sidewall spacer concept ([20]) consists in adding a new material on the sidewall of a patterned structure. Used in the microelectronics industry to optimize the transistors electric performance, we have tested it in our structures to improve the electrical contact.

From the materials easily available in the microelectronics industry which are resistant to oxidation and are fabrication process compatible, tungsten is the material chosen here. It has an acceptable electrical resistivity and thermal conductivity, 1.1 $m\Omega m$ and 174 $W m^{-1} K^{-1}$ respectively ([21]). It belongs to refractory metals, therefore withstands high temperatures (melting point 3422 °C) and it does not oxidize below 200 °C ([22, 23]) – *i.e.* the typical operation temperature in the structures. The fabrication method is a standard used in microelectronics industry ([21]) – *i.e.* *CVD-W* deposition over *Ti/TiN* as adhesive layer with *Al*.

In order to check the quality of the spacer, TEM images are made. The fabrication process is represented by Figure 4.16 and Figure 4.17, respectively the sample state after *W* deposition and the final spacer state. In both images an interfacial layer is observed between *Al* and *W*.

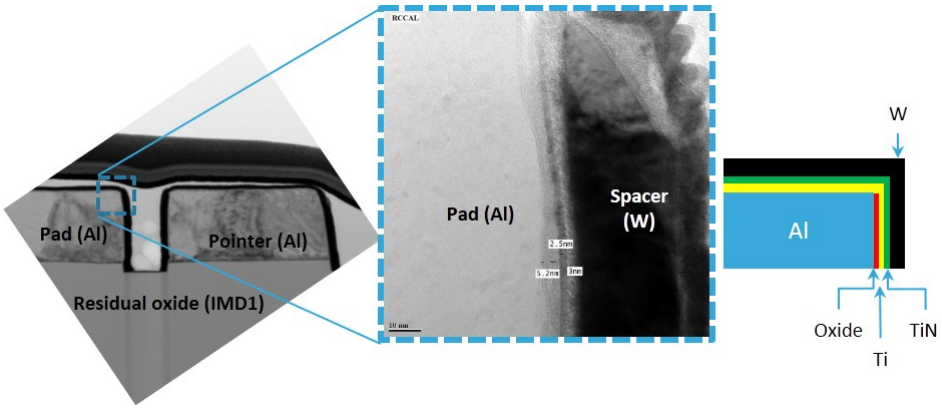

Fig. 4.16 The TEM view after CVD-W deposition of a) pointer-pad interface, b) a zoom in the *Al/ W* interface and c) schematic with all the layers observed: oxide (∼6 nm), *Ti* (2.5 nm), *TiN* (3 nm) and *W* (50 nm)

The interfacial layer, between Pad (*Al*) and Spacer (*W*), is composed by an oxide layer and the adhesive *Ti/TiN* layer:

- ∼6 nm of aluminium oxides, the undesirable insulator that might endanger electrical contact
- ∼2.5 nm of *Ti* layer: compound of the adhesive layer
- ∼3 nm of *TiN* layer: compound of the adhesive layer

The 6 nm of aluminium oxide, grows when the aluminium comes into contact with the air – during the manufacturing process.

A wafer with full layer of *Al* enters the etching machine, in a vacuum chamber, at the end of etching, the wafers move out from the protected environment and wait in the air to make the *TiN* deposition.

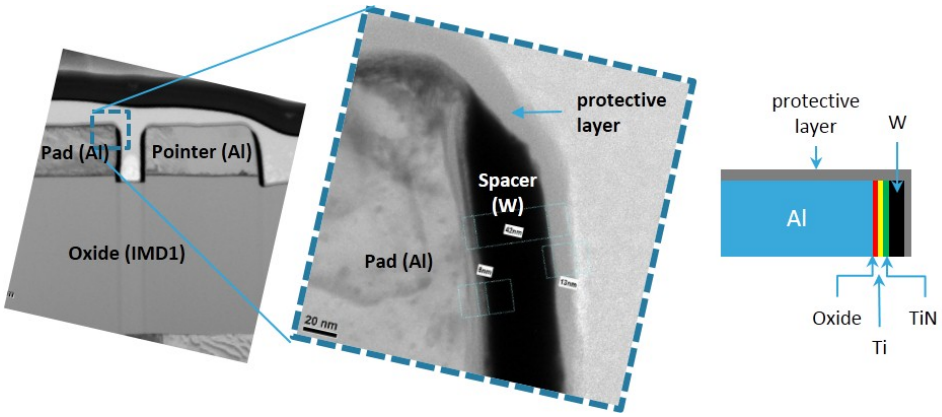

Fig. 4.17 The TEM view of *W-Spacer* in the final step before release a) pointer-pad interface, b) a zoom in the *Al*/*W* interface and c) schematic with all the layer observed: oxide (∼6 nm), *Ti* (2.5 nm), *TiN* (3 nm), *W* (∼50 nm) and protective layer (Al_2O_3 ∼15 nm)

The material fusion shown in Figure 4.15, in an Al_2O_3 / Al_2O_3 contact is here avoided thanks to protective tungsten layer. The aluminium oxide is now imbedded between *Al* and *W* layer. The *W* layer melts at 3422 °C, contrary to the *Al* which melts at 660 °C, even Al_2O_3 melts at lower temperature (2070 °C) than *W*. Therefore a fusion of contact is not expected.

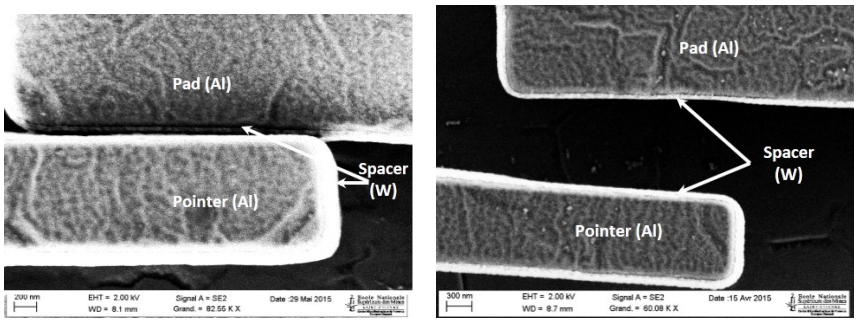

(a) (b)

Fig. 4.18 SEM image of contact zone in a structure after the release step. b) NORMALLY *On* and a) for a NORMALLY *Off* structure distance pointer-pad of (1.2 ± 0.2) µm is measured.

In order to ensure an electrical contact, the tungsten spacer is not the only improvement achieved in the fabrication process. After the fabrication process, and in order to promote easy

manipulation of samples, the wafer needs to be thinned (backlap) to be cut in the sawing step – *e.g.* this fabrication step can contaminate the wafer surface. In order to avoid any environment contamination, which could deteriorate the future electrical performances, a protective layer is added at the end of the manufacturing process, namely a Al_2O_3 layer of 30 nm (Figure 4.17) – $\sim$15 nm on each side – which will be removed at release step.

After release, the pointer rotation is smaller than with standard (*W-less*) samples. The additional material has a Young's modulus 7 times larger than *Al*– *i.e.* 411 GPa versus 70 GPa. Thus, the distance pointer-pad measured in the *W-Spacer* samples is (1.2 ± 0.2) µm (turn less due to the rigidity of the tungsten) (Figure 4.18), instead of (1.5 ± 0.2) µm measured in a standard samples (subsection 2.2.3).

4.2.3.1 FEM model (NORMALLY *Off* structure)

In order to validate a correct first rotation, generated by the relaxation of residual stress in *Al* layer, FEM analysis of the release of a NORMALLY *Off* cross is performed. As *W* is deposited on the sides, symmetrically, it has no bending effect around any axis, and it does not contribute to rotation either. Therefore, we do not need to know the residual stress within *W*.

The FEM model used in this part is similar to subsection 2.2.2 – *i.e.* only a release stage is studied.

A linear elastic and isotropic Tungsten material chart was obtained from COMSOL MULTIPHYSICS materials library; Young's modulus is 411 GPa ([24]), Poisson's coefficient is 0.28 ([24]).

The *W* layer (50 nm), 10 times less thick than *Al* (470 nm), is meshed in the *'swept mode'*: it copies the surface triangular mesh pattern on the top of *Al* and *W* layers, creating triangular prism elements (Figure 4.19).

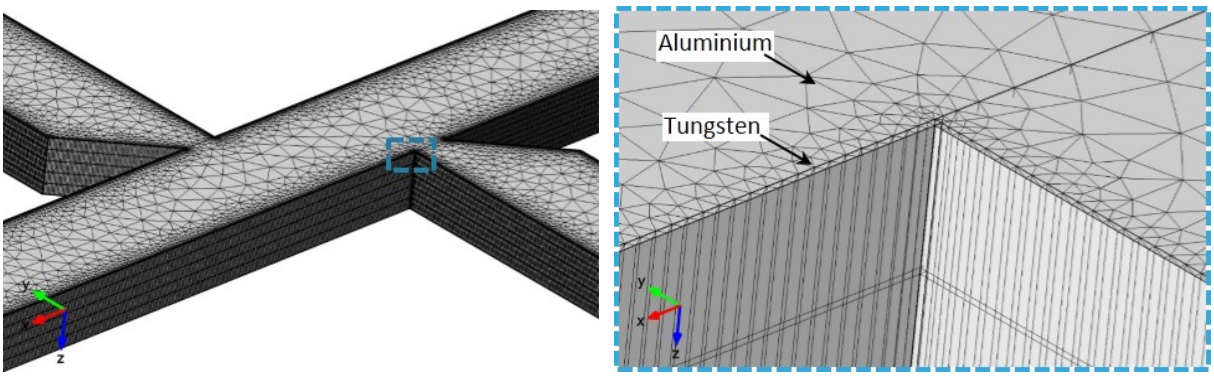

(a) (b)

Fig. 4.19 a) Mesh with 692 587 prism elements, b) zoom of hinge zone with the thin coat of tungsten

The in-plane movement is obtained without perturbation using an aluminium layer, laterally protected by a *W* coat for the structure, rotation can be studied reliably. The apparent stress (+190 MPa) is applied to the *Al* part of device as a longitudinal stress in both arms and pointer, which generates a rotation of central pointer at release stage (Figure 4.20).

In resume, the pointer/pad distance on a *W-Spacer* sample is:

- in simulation: 1.1 µm versus 1.2 µm obtained in a standard sample, *i.e.* ∼10 % less than with *non-W-coated* devices,

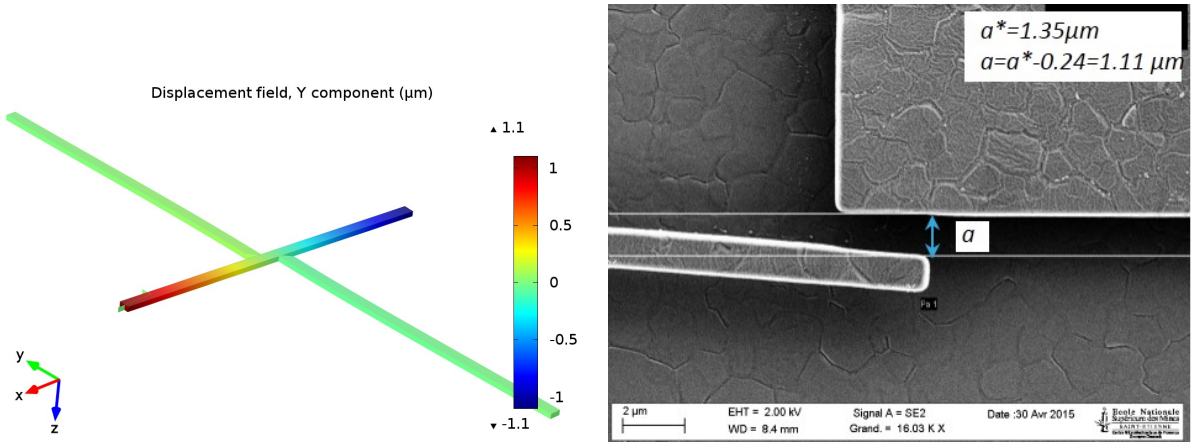

(a) (b)

Fig. 4.20 Illustration of the distance between the final position and the initial position (before release), a) *3D* Simulation and b) SEM measurement

- in SEM measurement: 1.2 µm versus 1.5 µm in a standard sample (chapter 2), *i.e.* ∼20 % less than with *non-W-coated* devices.

The fabrication process was successfully achieved, obtaining the correct spacer. The verification of correct operation is then validated. The rotation by a local asymmetric and controlled release is verified. The electrical function on this *W-Spacer* samples is then tested below.

4.2.3.2 Electrical characterisation of W-Spacer

As *Al* is the principal material in the patterned structure, the electrical actuation is identical to that performed in the previous chapter (chapter 3). Then during actuation test, the NORMALLY *On* and NORMALLY *Off* structures becomes *Off* and *On* respectively at 28 mA instead of 20 mA required by standard *Al* structure. The difference in current actuation between these two structures can be explained by the Young's modulus – *i.e.* 411 GPa for *W* versus 70 GPa for *Al*. In order to corroborate this value, estimated by optical microscopy observation, an electrical experiment will be performed.

Having proved that the structures moves like a standard one, hereafter a normally On structure is studied.

As Al_2O_3 is still present below the spacer layer, the requested electrical contact in *'W spacer samples'* can be performed in two ways:

- Either, tunnelling through the oxide

- Or breaking down the oxide, and in this case the *W* comes in contact with the *Al*.

The second case has a higher probability to work than in the *Al*- *Al* case, because the protective *W* layer will avoid welding of pointer and pad, while ensuring the electrical contact.

The test is performed on NORMALLY *On* structures. Similar to standard samples, this device makes contact at release stage and no actuation is needed.

In order to validate an ohmic contact, a particular electrical test is performed. The aim of this test is to measure an electrical contact in the *On* state, then activate the switch and lose contact (showing welding has not occurred). Figure 4.21 shows the connection used, where three terminals ensure the actuation and measure the contact current.

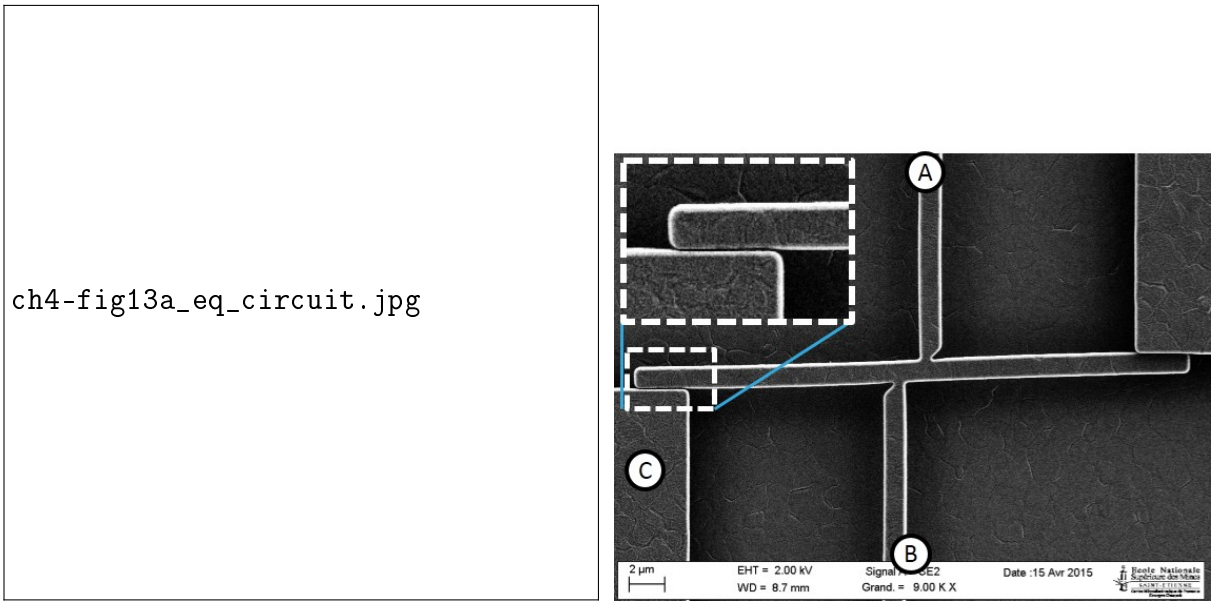

(a) (b)

Fig. 4.21 Equivalent circuit created by the connection and b) visualization of contact pad utilized on real structure

The voltage source (*VA*) is applied in *A* terminal and swept from 0 to 500 mV to cause a current in the arms as its actuation. To ensure that all current passes through the arms and avoid a leakage current to the contact until 200mV, the Vcont (in the pad *c*) source is polarised at 200 mV. In order to avoid arms damage or contact melting the current allowed in the arms is limited to 27 mA. Similarly, the current allowed in the contact is limited to 100 nA.

Figure 4.22 show the current in the arms (I arms) which rises to 24 mA. The *'I contact'* current is equal to 100 nA until 150 mV – *i.e.* the compliance current defined in the pad. Then a current flow is observed until 200 mV, which represents the current passing from the arms to the contact. Once the voltage of the arms reaches the 200 mV imposed in the pad the current

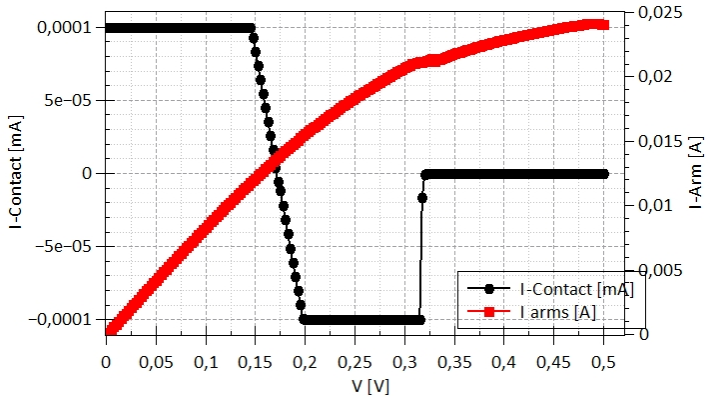

Fig. 4.22 *I-V* curve that corroborates a loss of the contact in a NORMALLY *On* structure of *W-Spacer* solution

reaches the 100 nA, this time flowing from the arms to the pad. Finally, at 320 mV with a current of ∼21 mA in the arms, the contact is lost and the *'I current'* goes down to zero.

This *W-spacer* solution has:

- a similar current actuation as standard structures (21 mA),
- much better electrical results with an intensity of 100 nA (compared to 1 nA in standard solution) – it could even be higher if we had not limited it to this value to avoid an increase in current and the risk of melt the structure,
- an additional fabrication step which is compatible with CMOS fabrication flow.

After a series of attempts at improving the electrical contact, this is the first really successful solution. Maybe it can be further improved in the sense of higher intensities. But its mechanical robustness must still be tested before this proposition can be implemented.

This electrical result arrives at the last time of characterisation work. Even if this hopeful result arrives at the end of this PhD work, the characterisation experience that was acquired on the structure development proves that this result can be repeated over time. The development of *W-Spacer* proves that the electrical contact with a small resistance is possible. Therefore, a thermo-electro mechanical switch is perfectly possible.

Summary

In this chapter the functionality of the structure (switch) is studied in terms of electrical contact (conduction efficiency), reliability upon cycling – both electrical and mechanical, and optimization of the structure itself with respect to these properties.

As switching is supposed to occur thousands of times, the first part of this chapter studied the reversibility of the movement. After release stage, the pointer-pad distance is not identical on both sides of the cross – a variation of 10 % is observed. The structure has been applied a running-in stage. Activated more than 1000 cycles, the pointer-pad distances evolve to become identical and stable.

Numerical simulation is used to show the stress concentration at sharp corners, which is a source of nonlinearity and non-reversibility. The structural damage caused by excessive heating is studied as well.

An ohmic electrical contact, repeatable and reversible, is desired and studied in the second part of this chapter. Then, in order to optimize the electrical contact resistance a study of the contact surface is realized.

During the manufacturing process, a native oxide layer grows on the aluminium structure when in contact with the air. The chemical analysis (XPS and AES) estimates an oxide thickness of 4 nm. Then, a cross-section TEM has been confirmed the 4 nm of *Al* oxide on the top of sample and 6 nm on the sidewall *Al* in the contact zone.

Thus, in order to create an electrical contact between the pointer to the pad, two possibilities are analysed:

- Either ensure a measurable tunnel current through the insulator layer, for applications where nA could be sufficient.
- Or add an oxidation-resistant interfacial material on the contacting surfaces to avoid or minimize the native oxide – namely "*W-Spacer*" solution.

The switch functionality is validated electrically. An electrical contact is reached at release step and lost in actuation step.

Résumé français

Dans ce chapitre la fonctionnalisation de la structure (en tant qu'interrupteur) est étudiée aussi bien d'un point de vue électrique que mécanique.

La commutation d'un interrupteur doit être réalisée des milliers des fois. Ainsi le travail cherchant à assurer une réversibilité dans le mouvement est présenté dans la première partie de ce chapitre. Après l'étape de libération, la distance pointeur-pad n'est pas identique des deux côtés de la croix – un écart de 10 % est observé. La structure a été rodée. Après plus de 1000 cycles d'actuation, la distance pointeur-pad devient identique des deux côtés et stable.

La concentration de contrainte résiduelle dans les angles de la structure, qui engendre des non-linéarités, est étudiée en utilisant la modélisation par élément finis. L'endommagement de la structure lors du passage d'un courant très élevé est également étudié.

La deuxième partie de ce chapitre est dédiée à l'étude du contact électrique. On souhaite que le contact soit répétitif et réversible. Ainsi, pour optimiser la résistance du contact, une étude sur la surface de contact est réalisée.

Le processus de fabrication des échantillons est réalisé dans un environnement dit propre – chaque étape de fabrication est réalisé sous vide. Les plaquettes suivent un flow de fabrication, mais lorsqu'elles rentrent en contact avec l'air (entre les étapes de fabrication), une fine couche d'oxyde croit dans l'aluminium.

Les analyses chimiques (XPS and AES) ont estimé une épaisseur d'oxyde de 4 nm. Puis, une coupe TEM a confirmé 4 nm d'oxyde sur la surface de l'échantillon et 6 nm sur la paroi d'*Al* dans la zone de contact.

Afin de créer un contact électrique entre le Pad et le Pointeur deux possibilités sont étudiées:

- Soit mesurer un faible courant tunnel, pour des applications d'une faible consommation énergétique, de l'ordre de quelques nA.

- Soit en ajoutant une couche protectrice d'un matériel non-oxydable (ou dont l'oxyde est plus conducteur (comme Ru)), afin d'empêcher la croissance d'oxyde ou de limiter son épaisseur – solution dénommé "*W-Spacer*".

Finalement, la fonctionnalité de l'interrupteur a été validée électriquement dans une structure NORMALLY *On*. Un contact électrique est établi lors de l'étape de libération, et perdu lors de l'étape d'actuation, la fonction de commutation est donc bien assurée.

Bibliography

[1] S. Orellana, B. Arrazat, P. Fornara, C. Rivero, S. Blayac, P. Montmitonnet, and K. Inal, "Robust design of thermo-mechanical MEMS switch embedded in aluminium BEOL interconnect," *Microelectronics Reliability*, vol. 55, no. 9-10, pp. 1896–1900, aug 2015. [Online]. Available: http://linkinghub.elsevier.com/retrieve/pii/S0026271415300275 135

[2] B. Arrazat, S. Orellana, C. Rivero, P. Fornara, A. Di Giacomo, and K. Inal, "From stress sensor towards back end of line embedded thermo-mechanical sensor," *Microelectronic Engineering*, vol. 120, pp. 41–46, may 2014. [Online]. Available: http://linkinghub.elsevier.com/retrieve/pii/S0167931713007016 135

[3] B. Arrazat, S. Orellana, C. Rivero, P. Fornara, A. Di-Giacomo, S. Blayac, P. Montmitonnet, and K. Inal, "Determination of material properties and failure using in-situ thermo-mechanical probe," in *2014 Symposium on Design, Test, Integration and Packaging of MEMS/MOEMS (DTIP)*, no. April. IEEE, apr 2014, pp. 1–5. [Online]. Available: http://ieeexplore.ieee.org/lpdocs/epic03/wrapper.htm?arnumber=7056700 135, 138

[4] B. El-Kareh and L. N. Hutter, *Silicon Analog Components*. Springer New York, 2015. [Online]. Available: http://link.springer.com/10.1007/978-1-4939-2751-7 139

[5] A. G. Evans and J. W. Hutchinson, "The thermomechanical integrity of thin films and multilayers," *Acta Metallurgica et Materialia*, vol. 43, no. 7, pp. 2507–2530, jul 1995. [Online]. Available: http://linkinghub.elsevier.com/retrieve/pii/095671519400444M 140

[6] H. Oughaddou, S. Vizzini, B. Aufray, B. Ealet, J.-M. Gay, J.-P. Bibérian, and F. D'Avitaya, "Growth and oxidation of aluminum thin films deposited on Ag(1 1 1)," *Applied Surface Science*, vol. 252, no. 12, pp. 4167–4170, apr 2006. [Online]. Available: http://linkinghub.elsevier.com/retrieve/pii/S0169433205009347 141

[7] E. Crinon and J. Evans, "The effect of surface roughness, oxide film thickness and interfacial sliding on the electrical contact resistance of aluminium," *Materials Science*

and Engineering: A, vol. 242, no. 1-2, pp. 121–128, feb 1998. [Online]. Available: http://linkinghub.elsevier.com/retrieve/pii/S092150939700508X 141

[8] K. Gloos, P. J. Koppinen, and J. P. Pekola, "Properties of native ultrathin aluminium oxide tunnel barriers," *Journal of Physics: Condensed Matter*, vol. 15, no. 10, pp. 1733–1746, mar 2003. [Online]. Available: http://stacks.iop.org/0953-8984/15/i=10/a=320?key=crossref.eb401cbe9fc0143dbd908b2373b5d8b9 145, 146, 148

[9] L. Kogut and K. Komvopoulos, "Breakdown of ultrathin native oxide films at contact interfaces of electromechanically stressed silicon microdevices," *Journal of Applied Physics*, vol. 97, no. 12, p. 124102, 2005. [Online]. Available: http://scitation.aip.org/content/aip/journal/jap/97/12/10.1063/1.1941467 141, 146

[10] J. Schultze and M. Lohrengel, "Stability, reactivity and breakdown of passive films. Problems of recent and future research," *Electrochimica Acta*, vol. 45, no. 15-16, pp. 2499–2513, may 2000. [Online]. Available: http://linkinghub.elsevier.com/retrieve/pii/S0013468600003479 141

[11] M. Biesinger, "X-ray Photoelectron Spectroscopy (XPS) Reference Pages," 2015. [Online]. Available: http://www.xpsfitting.com/2008/09/aluminum.html 142

[12] T. A. Carlson and G. McGuire, "Study of the x-ray photoelectron spectrum of tungsten—tungsten oxide as a function of thickness of the surface oxide layer," *Journal of Electron Spectroscopy and Related Phenomena*, vol. 1, no. 2, pp. 161–168, jan 1972. [Online]. Available: http://linkinghub.elsevier.com/retrieve/pii/036820487280029X 142

[13] B. R. Strohmeier, "An ESCA method for determining the oxide thickness on aluminum alloys," *Surface and Interface Analysis*, vol. 15, no. 1, pp. 51–56, jan 1990. [Online]. Available: http://doi.wiley.com/10.1002/sia.740150109 142

[14] F.-C. Chiu, "A Review on Conduction Mechanisms in Dielectric Films," *Advances in Materials Science and Engineering*, vol. 2014, pp. 1–18, 2014. [Online]. Available: http://www.hindawi.com/journals/amse/2014/578168/ 145, 148

[15] H. Spahr, S. Montzka, J. Reinker, F. Hirschberg, W. Kowalsky, and H.-H. Johannes, "Conduction mechanisms in thin atomic layer deposited Al2O3 layers," *Journal of Applied Physics*, vol. 114, no. 18, p. 183714, 2013. [Online]. Available: http://scitation.aip.org/content/aip/journal/jap/114/18/10.1063/1.4829910 146, 148

[16] Y. C. Yeo, T. J. King, and C. Hu, "Metal-dielectric band alignment and its implications for metal gate complementary metal-oxide-semiconductor technology,"

Journal of Applied Physics, vol. 92, no. 12, p. 7266, 2002. [Online]. Available: http://scitation.aip.org/content/aip/journal/jap/92/12/10.1063/1.1521517 146

[17] Y. Q. Wu, H. C. Lin, P. D. Ye, and G. D. Wilk, "Current transport and maximum dielectric strength of atomic-layer-deposited ultrathin Al2O3 on GaAs," *Applied Physics Letters*, vol. 90, no. 7, p. 072105, 2007. [Online]. Available: http://scitation.aip.org/content/aip/journal/apl/90/7/10.1063/1.2535528 148

[18] K. Ganesan, S. Ilango, M. Shanmugam, M. F. Baroughi, M. Kamruddin, and A. Tyagi, "Pre- and post-breakdown electrical studies in ultrathin Al2O3 films by conductive atomic force microscopy," *Current Applied Physics*, vol. 13, no. 9, pp. 1865–1869, nov 2013. [Online]. Available: http://linkinghub.elsevier.com/retrieve/pii/S1567173913002824 148

[19] N. Klein, "Electrical breakdown of aluminum oxide films flanked by metallic electrodes," *Journal of Applied Physics*, vol. 53, no. 8, p. 5840, 1982. [Online]. Available: http://scitation.aip.org/content/aip/journal/jap/53/8/10.1063/1.331423 148

[20] P. Tsang, S. Ogura, W. Walker, J. Shepard, and D. Critchlow, "Fabrication of high-performance LDDFET's with Oxide sidewall-spacer technology," *IEEE Transactions on Electron Devices*, vol. 29, no. 4, pp. 590–596, apr 1982. [Online]. Available: http://ieeexplore.ieee.org/lpdocs/epic03/wrapper.htm?arnumber=1482245 149, 150

[21] Y. C. Peng, "Structural and electrical properties of chemical vapor deposition tungsten overgrowth on physical vapor deposited and metalorganic chemical vapor deposited TiN adhesion layers," *Journal of Vacuum Science & Technology B: Microelectronics and Nanometer Structures*, vol. 16, no. 4, p. 2013, jul 1998. [Online]. Available: http://scitation.aip.org/content/avs/journal/jvstb/16/4/10.1116/1.590122 150

[22] V. D. Barth and G. W. P. Rengstorff, *Oxidation of tungsten*. Defense Metals Information Center, 1961. 150

[23] S. Cifuentes, M. Monge, and P. Pérez, "On the oxidation mechanism of pure tungsten in the temperature range 600–800°C," *Corrosion Science*, vol. 57, pp. 114–121, apr 2012. [Online]. Available: http://linkinghub.elsevier.com/retrieve/pii/S0010938X11006664 150

[24] L. B. Freund and S. Suresh, *Thin Film Materials*. Cambridge: Cambridge University Press, 2004. [Online]. Available: http://ebooks.cambridge.org/ref/id/CBO9780511754715 153

Conclusions & Perspectives

Contents

Conclusions

In this work, a class of microelectronic MEMS actuators has been investigated. It is innovative by its positioning inside the BEOL exploiting the fabrication residual stress, on a single Aluminium layer, and the choice to keep a perfect compatibility with the CMOS process line, namely by renouncing any non-standard material, *e.g.* gold or ruthenium which are used to improve electrical contact properties. This has imposed serious constraints for which alternative solutions had to be found, tested and commissioned.

This has forced us to scan a number of difficulties for which solutions have been elaborated at all the stages of the fabrication and commissioning process:

- Deposition and patterning of the layers
- Release of the suspended parts of the MEMS
- Actuation of the device to obtain a controlled movement and an electrical contact

First, a proper release protocole based on HF Vapor has been worked out in the laboratory to form fully suspended structures without stiction due to capillary effect or dummies which jeopardize the functionality during service life. Second, the residual stress has been exploited to obtain a movement by the release itself, either of the NORMALLY *On* or NORMALLY *Off* kind. This of course required measuring the residual stress, which has been done through full wafer curvature. A biaxial stress of 290 MPa has been found, in good agreement with literature. For our application, it had to be transposed to the uniaxial case, giving a line stress of 190 MPa. Third, spurious deformation connected in particular with the bilayer effect had to be eliminated, by suppressing the *TiN* layer and its estimated -900 MPa compressive residual stress from the suspended area which, as a matter of fact, does not need it.

These actions can be viewed as preliminaries but required a lot of time and care. Then, the precise control of the movement has been achieved thanks to adaptations of the design of the suspended part. The relationship between temperature and rotation angle (or more generally movement amplitude) has been established using an original, in situ hot plate in the SEM, then confirmed by Joule effect actuation. Considering the device used to demonstrate the feasibility of the approach, a switch, the last point was to obtain an ohmic electric contact, certainly the most difficult stage of this development due to the oxidation of aluminium which allows at best a poorly controlled tunnel current – which has been measured. This problem was finally solved by introducing a new step, the deposition of a nanometric *W* layer – but this metal remains among the standards of CMOS, the initial constraint is respected.

All along the study, on top of mastering the fabrication processes and characterizing the materials and structures formed, we took great care to develop a “virtual fabrication lab” in

the form of the coupled mechanical - electrical - thermal FEM model based on COMSOL MULTIPHYSICS. In the course of the project, it has allowed understanding the behaviour of our devices and elaborating solutions: attributing pointer bending to the bilayer effect, it suggested to eliminate *TiN*; irreversibility of the movement upon repeated actuation was explained by the observation of plastic strain at release and the effect of the design of the "hinge" has been clarified; the limit current leading to arm break has been referred thanks to numerical simulation not to melting, but to a combination of stress and high temperature, possibly enhanced by high current density via electromigration.

It must be emphasized that all these methodological developments are not restricted to the "cross" switch illustrated all along the memoir. In the course of the work, other geometries have been investigated in details, such as "H" symmetric structures. Other functions have been thought of such as variable capacities from classical comb-drive or a structure using several metal layer to increase the facing surface. We believe a whole family of devices can be developed faster and at a lower cost now that this combined experimental / numerical approach has been built.

Perspectives

The first industrial perspective consists in multiplying the devices of interest, to be developed in a shorter time thanks to the experimental / numerical methodology built here. Other geometries exploiting the fabrication residual stress can be designed, other functions can be given like a stress sensor or a mechanical security device. The present Joule effect actuation, which requires rather high intensities, in the 20 to 30 mA range, is probably too energy-greedy and could be replaced by an electrostatic actuation. The cross switch itself could certainly be improved in terms of dimensions, of geometry for robustness (hinge, cross section shape…). Models and understanding exist for upscaling or downscaling as well as for better functionality of improved robustness.

The tricky contact of the lateral side of a beam with the lateral side of a pad, which is very sensitive to movement imprecisions, can be facilitated by design ideas which have been fabricated but not fully tested during this PhD (see figures below):

- the notched pointer provides longer contact length and hopefully higher currents at contact thanks to its high flexibility. The FEM study of this design modification (Figure 1b) shows a 25-fold increase of the contact area (from 0.04 to 1 µm) and a contact force increase by 50 %, reaching 3 µN. While the maximum pressure is 5.5 MPa, the medium pressure is around of 3 MPa

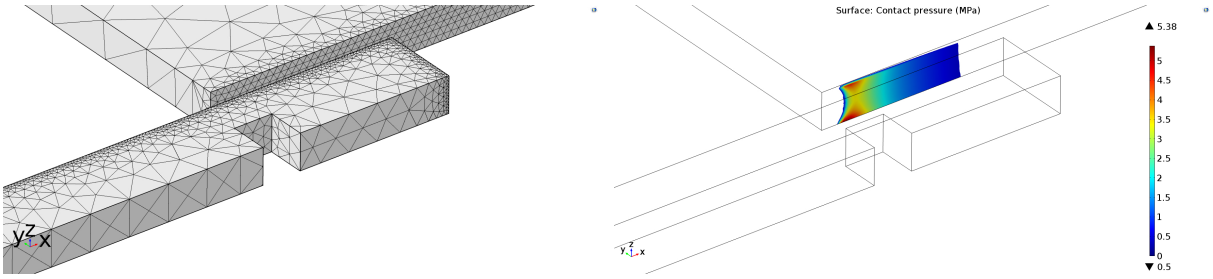

(a) (b)

Fig. 1 Notch pointer: a) adapted tetrahedral mesh, refined in the contact vicinity, b) contact area (1 µm^2) and contact pressure

- the tipped pointer which on the contrary concentrates the contact on a well-defined dimension and allows larger contact pressures. The tip shape is designed as square but is rounded by the fabrication process. The tip shape helps to increase the electric field, which should reduce the electric field of $\sim$10 GV m^{-1} needed to obtain a 0.4 nA by tunnelling (subsection 4.2.2.1)

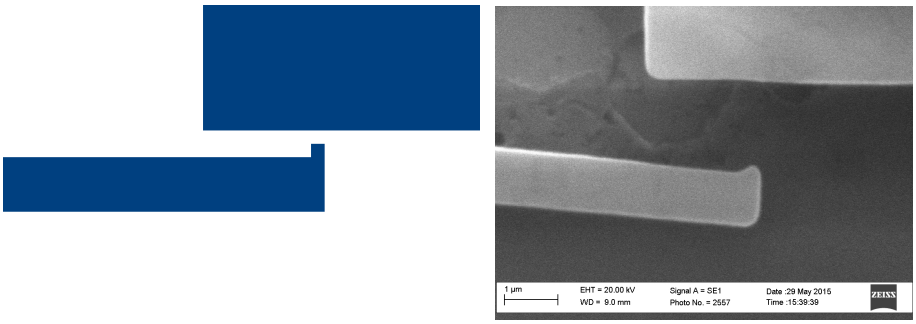

(a) (b)

Fig. 2 Tip solution to increase contact pressure, a) design, and b) SEM image of the device

Another major subject is the packaging of devices. The structure oxidizes easily in contact with air, so it must be done in a controlled environment. A seal ring defined around the device, which are made using the "metallic vias" (a sort of pillar that connects the different levels of metal) has been thought.

The virtual fabrication laboratory is central in our approach. It can certainly be improved, not only by using more complete versions of COMSOL MULTIPHYSICS. Precision can be gained by deepening the understanding of the heat transfer (convective as well as radiative) in confined, microscale and multibody spaces. Investigating non-reversibility and optimizing *e.g.* the hinge geometry would benefit from a more sophisticated elastic-plastic model, the parameters of which should of course be identified experimentally in an adequate way. Moreover, the assumption that electromigration could be one of the causes of break at high intensity or long times (repeated actuation) could be tested numerically in a more explicit and complete way.

As all R& D work, this PhD has also raised more fundamental questions and put forward needs which could not be investigated in details but would certainly deserve more attention. Thus, the relationship between intensity, temperature and arm fracture would have been determined with more certainty if a microscale temperature measurement system had been available. Two such apparatuses, an IR camera, have been preliminary tested in Toulouse (LAAS) and in Saint-Etienne (EMSE).

Appendix A

Scientific contribution

B. Arrazat, S. Orellana, C. Rivero, P. Fornara, A. Di-Giacomo, S. Blayac, P. Montmitonnet, and K. Inal, "Determination of material properties and failure using in-situ thermomechanical probe", *in 2014 Symposium on Design, Test, Integration and Packaging of MEMS/MOEMS (DTIP)*. IEEE, apr 2014, pp. 1–5. [Online]. Available: http://ieeexplore.ieee.org/lpdocs/epic03/wrapper.htm?arnumber=7056700

S. Orellana, B. Arrazat, P. Fornara, C. Rivero, A. Di Giacomo, S. Blayac, K. Inal, and P. Montmitonnet, "Improvement of freestanding CMOS-MEMS through detailed stress analysis in metallic layers", *in 2014 15th International Conference on Thermal, Mechanical and Mulit-Physics Simulation and Experiments in Microelectronics and Microsystems (EuroSimE)*. Ghent: IEEE, apr 2014, pp. 1–6. [Online]. Available: http://ieeexplore.ieee.org/lpdocs/epic03/wrapper.htm?arnumber=6813834

B. Arrazat, S. Orellana, C. Rivero, P. Fornara, A. Di Giacomo, and K. Inal, "From stress sensor towards back end of line embedded thermo-mechanical sensor", *Microelectronic Engineering*. vol. 120, pp. 41–46, may 2014. [Online]. Available: http://linkinghub.elsevier.com/retrieve/pii/S0167931713007016

S. Orellana, B. Arrazat, P. Fornara, C. Rivero, S. Blayac, P. Montmitonnet, and K. Inal, "Robust design of thermo-mechanical MEMS switch embedded in aluminium BEOL interconnect", *Microelectronics Reliability*. vol. 55, no. 9-10, pp. 1896–1900, aug 2015. [Online]. Available: http://linkinghub.elsevier.com/retrieve/pii/S0026271415300275

Appendix B

Back end of line: fabrication process flow

The CMOS and the MEMS fabrication flow are very similar. This is because both use photolithography processes. The CMOS fabrication is separated in front end of Line (FEOL) and BEOL. The FEOL is composed of the electrically active devices *i.e.* transistors, diodes, resistances. The interconnections of the actives devices are realized in the BEOL, mainly made of alternating metal and oxide.

At STMicroelectronics, we use mid-wafer short loop test vehicles for rapid learning cycles – *i.e.* without active devices. Thus, only the fabrication of the interconnection part is explained here. Using a *Si* substrate, the first step is wet thermal oxidation at 1150 °C to obtain a 3 nm thick thermal SiO_2 protective layer Figure 1.

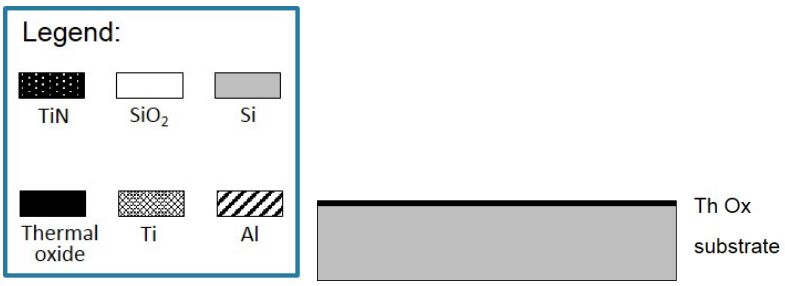

Fig. 1 Legend of cross-section view of figures, first step of short loop fabrication b) thermal oxidation (Th Ox)

In the fabrication flow, over the silicon substrate a successive alternation of an insulator (SiO_2) also called IMD and a metallic layer – principally *Al* (Cu) or *Cu* – is deposited, thus forming the BEOL.

The metallic layer fabrication is performed in three steps, *Ti*, *Al* (Cu) and *TiN* deposition (Figure 2).

Fig. 2 Description of the metallic layer, composed by Ti/AlCu/TiN, which is made in three continuous deposition steps

A thin layer of 7.5 nm of *Ti* is deposited over the silicon oxide. In the same equipment, changing the chamber of deposition, the 470 nm of *Al* film is sputtered using PVD from a target containing 0.5*wt*% *Cu* – *i.e.* *Al* (Cu). The 45 nm of *TiN* layer is added on top of the *Al* layer to avoid the electromigration of *Al* lines. This *TiN* is deposited using CVD process with a heater temperature of 450 °C and a wafer temperature of 407 °C. The *TiN* is classified as a "barrier metal", because it avoids the diffusion of metal (*Al* (Cu)) into the silicon and silicon dioxide. The pure titanium is sublimed and react with nitrogen in a high-energy, vacuum environment.

This metallic layer is deposited on full wafer (Figure 3a). In order to isolate the consecutive metal layers, an undoped CVD SiO_2 (TEOS) is deposited (Figure 3b) at 700 °C – *i.e.* CVD deposition.

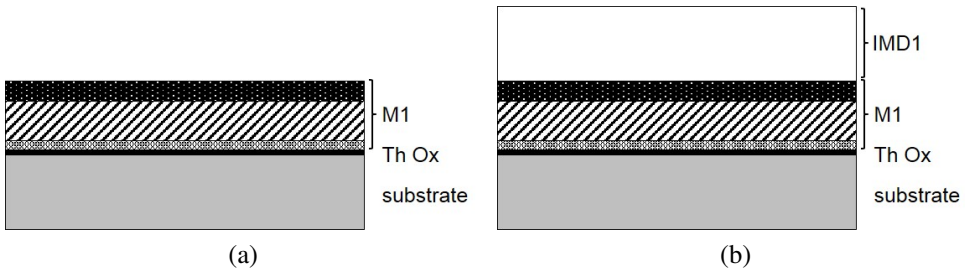

Fig. 3 a) Metallisation on full wafer, and b) CVD of sacrificial IMD1

Over the IMD layer of 1.6 µm a new metallic layer is deposited on full wafer (Figure 4a). In order to draw the motif in this new metallic layer, a photolithography is realized next. A photoresist resin is spread over the *M3* layer (Figure 4b).

In the case of a resin called "negative", the part exposed to light through a mask becomes insoluble in developer and allows to create the motives on metallic layer (Figure 5a). An anisotropic plasma etches the *M3* layer to create the structures on this layer (Figure 5b).

Finally, the photoresist is removed (Figure 6) and the device is finished. At this stage the wafer leaves the production and will be processed in the laboratory to prepare the samples and release the devices.

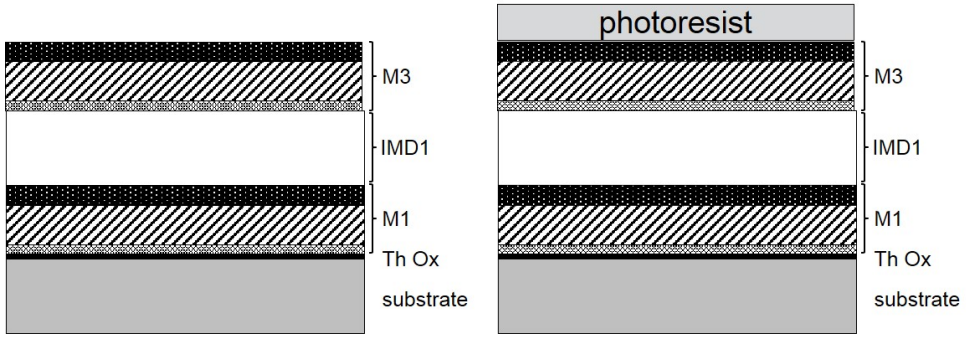

(a) (b)

Fig. 4 a) PVD metallisation on full wafer of M3 Metallic layer, and b) spread of the photoresist

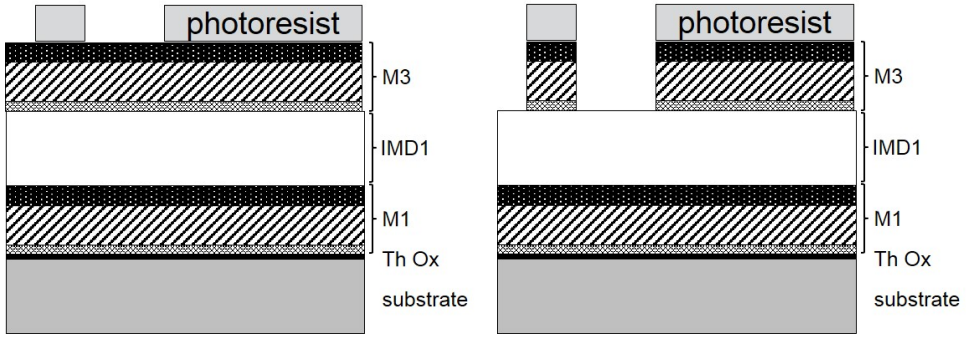

(a) (b)

Fig. 5 a) Opening motif to etch by the insolation of resin, b) etch of metallic layer using photoresist mask

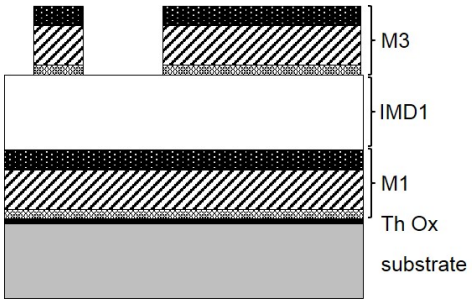

Fig. 6 Manufacturing is finished at this stage and the wafer proceeds to post-processing steps (sawing and etching)

After sawing the dices, the sacrificial layer is etched in a Vapor-HF process for 40 min. This releases thin beams but leaves larger structures (pad) attached to the M1 layer. The Vapor-HF method prevent stiction of free structures to the *M1* layer.

The principal parameters used in material deposition are shown in Table B.1, following a standard fabrication process.

Material added	Process	Values
	deposition temperature	450 °C
AlCu(0.5*wt*%) – PVD	plasma power	Stabilization + 14 k + 6 k + 2 k
	deposition time	10 s + 10.8 s + 18.9 s + 9.5 s
	deposition temperature	400 °C
TEOS – CVD	plasma power	0.5 k
	deposition time	78 s

Table B.1 Plasma parameters used in Aluminum and Silicon Dioxide – TEOS deposition

Appendix C

A critical process step: the release of structures

The most technological step of this project, the release of the main structure (cross), consists in etching the oxide below (or around) the metal layer to free the expansion arms and the central pointer.

There are three methods to etch the SiO_2; the wet, the dry, and the gaseous etch which are also known as chemical, physical, and vapor etching respectively.

- The dry etch (physical or plasma etch) uses oxygen plasma, more precisely a CHF_3, CHF_3O_2, SF_6 or SF_6O_2 at certain temperature and pressure in a vacuum chamber, to remove silicon dioxide; this technique normally produces an anisotropic profile, so it is not suitable to our objective of getting freestanding parts.

- The wet etch (chemical or HF etch) uses HF, more precisely a 50 % solution of hydrofluoric acid in water, applied during 10 s, giving an "isotropic" profile. The sample is then rinsed by deionized water and isopropanol alcohol.

- A third alternative also useful is to use the gas-based method; the wet HF is heated to 40 °C, it evaporates and etches the oxide without wet process.

Several problems due to imperfect release of wet etch, using pure HF solution, are reported. A general difficulty is that contrary to industrial conditions, wet etching by a manual process is an uncontrollable and poorly repeatable procedure, in particular due to the short etching time which cannot be enforced accurately, but there is a risk of damaging the metals.

Another problem with wet etching is the risk to stiction of mobile parts Figure 1. During the process, the evaporating liquid forms a meniscus; its very small radius of curvature builds

up a very high attractive Laplace force (due to surface tension of the solution) which may bend the arms towards the floor layer. If contact occurs, adhesive forces cannot be counteracted any more. Therefore, I chose gaseous etching.

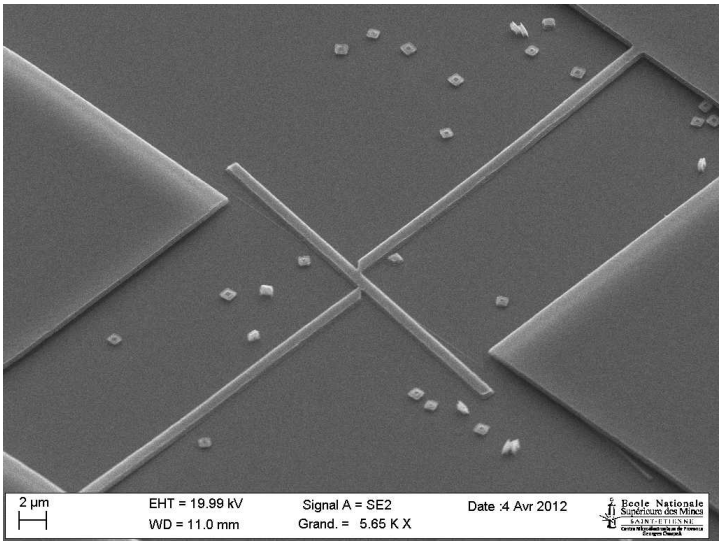

Fig. 1 Stiction in the released structure

Appendix D

Comsol Multiphysics

D.1 Software description

COMSOL MULTIPHYSICS is composed by a main core, Comsol Multiphysics, and then different modules can be added to deepen a certain study (Figure 1).

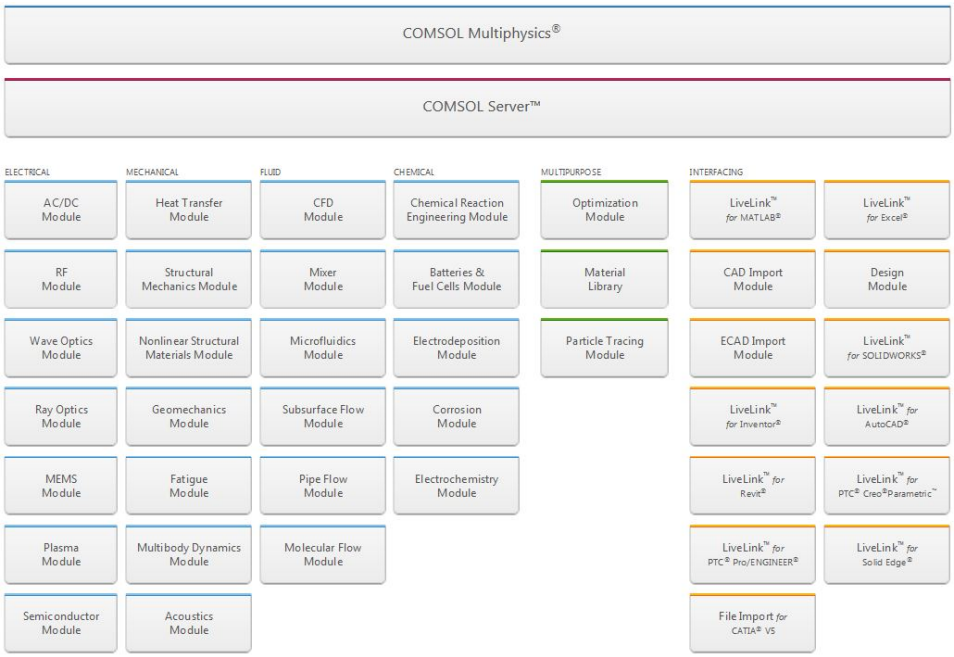

Fig. 1 The available modules in COMSOL MULTIPHYSICS

In order to model our device in finite element, COMSOL MULTIPHYSICS proves well adapted. This is because of its performance in the various multiphysics coupling modules and simplicity in the post-processing of the data collected. It offers powerful solvers who can solve problems numerically very large.

The predefined templates permit to simulate physical phenomena such as electrostatics, fluid mechanics, heat transfer and deformation of materials, and coupling them with ease through a graphical interface.

To solve a problem using COMSOL MULTIPHYSICS, the logical sequence of steps is:

1. Creation of geometry;
2. Definition of physical properties involved in partial differential equations;
3. Definition of boundary conditions;
4. Choice of mesh;
5. Digital resolution and viewing result

D.2 Contact modelling in Comsol

The augmented Lagrangian method is implemented in COMSOL MULTIPHYSICS contact model. This technique is explained by Simo and Laursen [1] and Zavarise [2].

Extract from Comsol documentation where the augmented Lagrangian method is explained [3]:

"In the augmented Lagrangian method, the system of equations is solved in a segregated way. Augmentation components are introduced for the contract pressure T_n and the components T_{ti} of the friction traction vector T_t. An additional iteration level is added where the usual displacement variables are solved separately from the contact pressure and traction variables. The algorithm repeats this procedure until it fulfils a convergence criterion. Using the special gap distance variable, the penalized contact pressure T_{np} is defined on the destination boundary as

$$T_{np} = \begin{cases} T_n - p_n d_g & \text{if } \ d_g \leq 0 \\ T_n e^{\frac{-(p_n d_g)}{T_n}} & \text{otherwise} \end{cases} \quad \text{(D.1)}$$

where d_g is the gap distance between the destination and source boundary, and p_n is the user-defined normal penalty factor."

References

[1] J. Simo and T. Laursen, "An augmented lagrangian treatment of contact problems involving friction", *Computers & Structures*, vol. 42, no. 1, pp. 97–116, jan 1992. [Online]. Available: `http://linkinghub.elsevier.com/retrieve/pii/004579499290540G`

[2] G. Zavarise, P. Wriggers, and B. A. Schreer, "On augmented Lagrangian algorithms for thermomechanical contact problems with friction",*International Journal for Numerical Methods in Engineering*, vol. 38, no. 17, pp. 2929–2949, sep 1995. [Online]. Available: `http://doi.wiley.com/10.1002/nme.1620381706`

[3] Comsol, "Structural Mechanics Module User's Guide", Comsol, Ed. Comsol, 2014, p. 494

Appendix E

Chemical analysis

In order to identify the chemical compounds in the structure, an array of bridges is performed. To have an accurate data information a dense structure is needed. A dense bridge-shaped structures, placed close to our structures are fabricated (Figure 1).

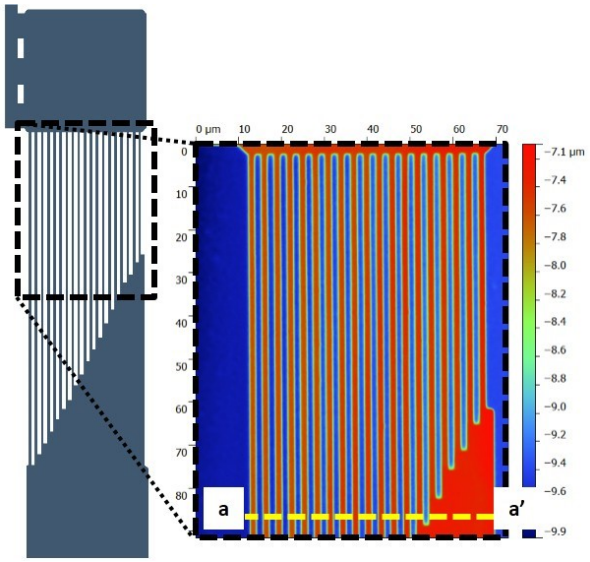

Fig. 1 a) schema and b) optical profile of parallel bridges, which are suspended 1.6 µm over *M1* metallic layer

In order to identify the contamination in functional devices, the interest is focused on obtaining the chemical composition in the side of freestanding structures. The XPS analysis is performed in 3 zones (Figure 9):

- In the top of a pad, to obtain the material present in the top surface.
- In the top of 'bridge arrangement', to quantify the difference with a homogenous zone (pad), and

- In the top of ‘bridge arrangement’, but tilted 20°, to identify the material present in the side of freestanding structures.

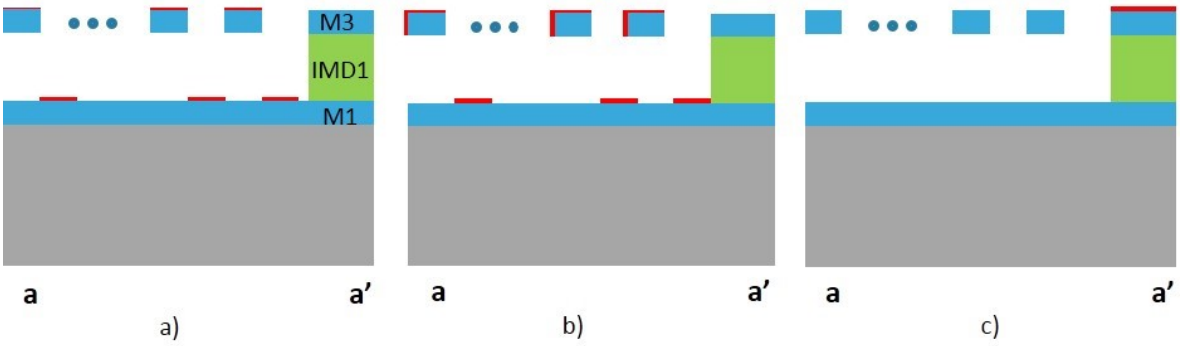

Fig. 2 Cross section view of Figure 1 and surfaces (in red) analysed by XPS analysis, a) top, and b) sides of the ‘bridges’, and c) top of the pad

The information given by the top of the pad is a reliable information of the surface condition on the top of the sample.

To obtain the surface composition of the sidewall, the information obtained by a top analysis is compared to the tilted analysis. Thanks to this experiment, an aluminium oxide of 4 nm and 6 nm has been found in the top and in the side of *Al* structure.

Nomenclature

A	area of the conducting electrical lines
a	distance from the pointer to its initial position
A^*	saturation ionization in the gas
a^*	pointer/pad distance
a_c	radius of a circular contact area
a_f	lattice constants on thin film
a_s	lattice constants on substrate
A_b	bearing area
A_H	Hamaker constant
A_n	nominal area
a_{rc}	critical area of asperities
A_r	total real contact area
a_r	real contact area of asperities
B^*	a constant related to the excitation and ionization energies
C	the 4^{th} order elasticity tensor
c	specific heat
D	fractal dimension of the surface profile (fractal model)
d	distance between two surfaces that come in contact (Ch.1)

d cantilever tip deflection (Ch.2)

E isotropic elastic modulus

E' equivalent elasticity modulus

E_F Fermi level

F force in a contact

F_0 constant electron flow

F_i forces of the cantilever

f_i spatial frequency i

F_m capillarity force

F_{VDW} Van der Waals force

G fractal roughness parameter (fractal model)

H macroscopic contact hardness

h Planck's constant

h' standardized separation

h_p distribution of peak heights

I_i intensities of the metal and oxide photoelectron peaks (Ch.4)

I_i moment of inertia

J current density

K thermal conductivity

k Boltzmann's constant

K' hardness coefficient related to the Poisson ratio

K^* Knudsen number

k_{wf} curvature of wafer

L length of the conducting electrical lines

l	length scale of a single asperity (fractal model)
ℓ	electron elastic mean free path
M	biaxial modulus
m^*	effective electron mass in the oxide
m_0	electron rest mass
M_i	moments of the cantilever
N	number of asperities
n	number of contact spots
N_C	density of states in conduction band
N_i	volume densities of atoms in the metal and in the oxide
P	load in a contact
p	pressure applied in a contact
p_g	gas pressure
$\overline{p}$	average pressure
q	electron charge
R	electrical resistance
r	half distance between two spots
Ra_L	Rayleigh number
R_H	Holm electric resistance
R_s	Sharvin Resistance
R_{wf}	radius of wafer
R_w	Wexler resistance
S	second Piola–Kirchhoff stress tensor
T	temperature

t time

t_f film thickness

t_s substrate thickness

t_{eot} equivalent oxide thickness

U voltage

U_{ext} external voltage

V_B breakdown voltage

w interference of asperity (fractal model)

w sinking on Hertz' theory

z height of asperities

$z(x)$ surface profile in contact

Greek Symbols

α coefficient of thermal expansion

β radius of the sphere in a spot contact

β' amplification factor

β_i asperity amplitude corresponding to the given frequency

δ full height of asperity (fractal model)

ε strain tensor

ε_{th} emissivity

η density of asperities

$\gamma(K^*)$ gamma function

γ^n frequency spectrum of the surface roughness (fractal model)

γ_{1v} surface tension of water

γ_{se} secondary electron emission coefficient

λ inelastic mean free path

μ electron mobility

ν Poisson's ratio

$\overline{\sigma}$ biaxial stress component

$\phi(z)$ distribution density function of the measured roughness height

ϕ_B junction barrier height

ϕ_T depth of traps potential well

ψ plasticity index

ρ electrical resistivity

ρ radius of curvature of the cantilever beam (Ch.2)

ρ_m material density

σ substrate thickness

σ_a standard deviation of the height distribution

σ_{mf} misfit stress

θ contact angle

θ rotation angle (Ch.2)

θ_a photoelectron take-off angle

ε electric permittivity

$\varkappa$ relative dielectric constant of the oxide layer

ξ electric field

ξ_c p/H ratio

Résumé

Ces dernières années la miniaturisation des microsystèmes atteint la limite physique de leur développement. Ainsi une de voie d'innovation dans l'industrie des semi-conducteurs est l'intégration des fonctionnalités supplémentaires au sein des composants déjà existants.

Le projet consiste à intégrer, dans une même couche métallique d'interconnexion CMOS, un MEMS capable, par sa rotation, d'établir un contact électrique.

Les verrous se situent dans la libération des parties mobiles par dissolution de l'oxyde environnant (déformation hors plan sous l'effet des contraintes résiduelles, stiction, présence de résidus qui empêchent le contact), dans l'actionnement (densité de courant, répétabilité, durabilité, fiabilité) ainsi que, la capacité d'établir un vrai contact électrique à faible résistance (aire réelle / apparente du contact des surfaces rugueuses, pollution du contact).

Le travail réalisé a porté sur la conception, le design et la simulation des microsystèmes afin de surmonter ces difficultés et / ou d'étudier le comportement et mesurer les effets.

Mots Clés

Contraintes résiduelles, contact, Back end of line, Simulation Multiphysique, CMOS-MEMS

Abstract

In recent years the miniaturization of microsystems is reaching the physical limit of its development. Thus, a path of innovation in the semiconductor industry is additional functionalities in existing components.

The project consists to integrate a MEMS, within the same metal interconnect of CMOS layer which, by rotating, can establish an electrical contact.

The obstacles are in the release of the moving parts by dissolution of the surrounding oxide (out of plane deformation under the effect of residual stress, stiction, residues which prevent contact), in the actuation (current density repeatability, durability, reliability) and, for ohmic switches, the ability to establish a real electrical contact with low resistance (real / apparent area of contact with rough surfaces, contact pollution).

The work carried out has focused on conception (design) and simulation of microsystems to overcome these difficulties and / or to study the behavior and measure the effects.

Keywords

Residual stress, contact, Back end of line, Multiphysics simulation, CMOS-MEMS

Numero national de thèse :